SIMULATION OF OPTICAL DEVICES AND CIRCUITS USING TIME DOMAIN METHODS

SIMULATION OF OPTICAL DEVICES AND CIRCUITS USING TIME DOMAIN METHODS

by

LIN HAN

A Thesis

Submitted to the School of Graduate Studies

in Partial Fulfillment of the Requirements

for the Degree

Doctor of Philosophy

McMaster University

©Copyright by Lin Han, September 2012

DOCTOR OF PHILOSOPHY (2012) McMaster University

(Electrical and Computer Engineering) Hamilton, Ontario

TITLE: SIMULATION OF OPTICAL DEVICES AND CIRCUITS USING TIME DOMAIN METHODS

AUTHOR: LIN HAN
SUPERVISOR: DR. WEI-PING HUANG
PROFESSOR, DEPARTMENT OF ELECTRICAL AND COMPUTER ENGINEERING

NUMBER OF PAGES: xx, 151

Abstract

In design of large scale optical devices and circuits, it is important to do simulation by aid of modern computation techniques before fabrication to significantly reduce total costs and development cycles. Several numerical methods, such as the Finite-Difference Time-Domain (FDTD) method, the Beam Propagating Method (BPM), the Mode Matching Method (MMM), and the Couple Mode Theory (CMT), have been widely adopted in academic fields and commercial software packages for different applications. Among all these numerical methods, the FDTD method is the most popular one in device simulation and design verification. The main reason relies on the fact that the FDTD method is a rigorous numerical model for simulating of electromagnetic field in a variety of materials with high accuracy and feasibility. However, the FDTD method is extremely memory and time consuming when employed to simulate large scale structures. This thesis mainly focuses on improving the efficiency of the FDTD method in modeling optical devices of different materials including dispersive, nonlinear and gain materials. A circuit model based on the complex mode theory is proposed for analysis of large scale compact optical devices and high density integrated circuits using the improved FDTD method. With the aid of the proposed method, the computing resources required for Computer-Aided Design (CAD) of large scale optical devices and circuits could be dramatically reduced.

In this thesis, a new model, referred to as the Rational Dispersion Model (RDM) is proposed for modeling of dispersive materials in wide wavelength range using the FDTD

method with high efficiency. A parameter estimation method is introduced for the RDM to fit material permittivity functions fast and accurately. The improved FDTD method with the RDM model is implemented and verified in simulation of the nano-wires. The cross-section spectrum characteristics of different nano-particles are systematically studies by employing the implemented method.

For the nonlinear materials, the second and third order nonlinearities including the Kerr and Raman effects are considered and implemented in the improved FDTD method with the RDM serving as a powerful tool in simulation of optical devices with nonlinear effects.

The RDM is then employed in modeling of optical gain profiles of semiconductor materials. The FDTD method with the RDM and a rate equation model are proposed to accurately simulate semiconductor lasers with arbitrary cavity geometries.

In waveguide modal analysis, a hardware-accelerated FDTD method combined with the matrix pencil method is proposed to solve both guided and leaky modes with high efficiency.

In the last part of this thesis, a circuit model based on the complex mode theory is proposed for analysis of large scale structures with non-negligible radiation effects. Firstly, a large scale structure is partitioned in to small building blocks. Each of these building blocks is then to be analyzed through the improved FDTD method. The generated results are then cascaded to produce the final result of the entire structure. This model is verified through analysis of different optical structures.

Acknowledgements

The past four and a half years at McMaster University have been a gratifying experience to me. As the journal is coming to an end, I would like to express my sincere gratitude to those people who have given me great opportunities to expand my knowledge and to strengthen myself by overcoming my weaknesses.

First and foremost, I would like to thank my supervisor Dr. Wei-Ping Huang for directing me in my research with his grand vision, for encouraging me in my studies, for sharing his rich knowledge with me without reservation and for supporting my life in Canada.

I would also like to give grateful thanks to Dr. Xun Li for his guidance and hand-in-hand help during my research and for his inspiration and help in all aspect of my life.

I would also like to acknowledge the great help and support for my research work from my committee members: Dr. Chih-Hung Chen, Dr. Chang-Qing Xu and Dr. Shiva Kumar.

I would also like to thank my former supervisor Dr. Kang Li in Shandong University. He recommended and encouraged my continuing study in McMaster University after graduation. I also want to thank Dr. Kang Li and Dr. Fanmin Kong, who is also at Shandong University, for the insightful advices on several topics of my research.

I also want to thank my colleagues and friends in the Photonic Research Lab: Yu Li, Qingyi Guo, Yanping Xi, Jianwei Mu, Lanxin Deng, Yefeng Wen, Rui Wang and

Dong Zhou for helping me in both my study and life. I really appreciate the time I spent with them.

I am very grateful to McMaster's ECE administrative and technical staff, Ms. Cheryl Gies, Ms. Helen Jachna, Ms. Danielle Marcellin, Mr. Terry Greenlay, and Mr. Cosmin Coroiu.

Finally, I would like to give my deep love and thanks to my wife Meili Ma for her endless patience and support in my life in Canada, my parents and twin sister for their encouragements, supports and love.

Contents

Abstract iii

Chapter 1 Introduction 1

1.1 Motivation 1

1.2 Overview of the Thesis and Contributions of the Research 3

Chapter 2 FDTD Method for Dispersive Materials 6

2.1 Introduction 6

2.2 Rational Dispersion Model 7

2.2.1 Introduction 7

2.2.2 The RDM Oscillator 10

2.2.3 Analysis of the RDM in Time Domain 12

2.3 Implementation of the RDM in the FDTD Method 14

2.4 Parameter Estimation of the RDM 16

2.5 Verification of the FDTD Method with the RDM 22

2.6 Analysis of Metal Nano-particles 24

2.6.1 Simulation of Single Nano-ellipsoid 26

2.6.2 Simulation of Nano-ellipsoid Dimer 30

2.6.3 Simulation of Single Nano-ellipse 34

2.6.4 Simulation of Nano-ellipse Dimer 38
2.6.5 Simulation of Nano-ellipse Trimer 44
2.6.6 Summary of Optical Properties 50
2.7 Summary 52
Chapter 3 FDTD Method for Nonlinear Materials 53
3.1 Introduction 53
3.2 Linear Polarization 54
3.3 Second-order Nonlinear Polarization 56
3.4 Third-order Nonlinear Polarization 57
3.4.1 The Kerr Effect 57
3.4.2 The Raman Effect 58
3.5 Electric Field Updating Scheme 60
3.6 Magnetic Field Updating Scheme 62
3.7 Summary of the FDTD Updating Scheme 63
3.8 Simulation of 1D-temporal Soliton 64
3.9 Summary 67
Chapter 4 FDTD Method for Gain Materials 68
4.1 Introduction 68
4.2 Optical Model for Gain Materials 69

4.3 Rate Equation Model for Carriers 76
4.4 FDTD Updating Scheme for Gain Material 79
4.5 Verification 80
4.6 Application 85
4.7 Summary 89
Chapter 5 FDTD Method for Modal Analysis of Waveguides 90
5.1 Introduction 90
5.2 Wave Equation-based Compact 2D-FDTD Method with UPML ABCs 92
5.2.1 Fullvectorial Scheme 92
5.2.2 Semivectorial Scheme 96
5.2.3 Scalar Scheme 97
5.3 Extraction of Mode Parameters by Matrix Pencil Method 98
5.4 Assessment and Validation 100
5.4.1 Guided Mode Analysis 100
5.4.2 Leaky Mode Analysis 102
5.5 Error Analysis and Convergence Test 104
5.5.1 Convergence with FDTD Time Steps 105
5.5.2 Convergence with MPM Sample Number 105
5.6 Performance of the Mode Solver on GPUs 106

5.6.1 Memory Consumption 107

5.6.2 Time Consumption 108

5.7 Summary 110

Chapter 6 Circuit Model with Complex Mode Expansion Method 111

6.1 Introduction 111

6.2 Partition Methodology and Building Blocks 113

6.3 Complex Mode Expansion Method 116

6.4 Complex Scattering Matrix 122

6.5 Cascade of the Complex Scattering Matrices 126

6.6 Verification 128

6.7 Applications 132

6.8 Summary 137

Chapter 7 Conclusions and Future Work 139

7.1 Summary of Contributions 139

7.2 Suggestions of Future Work 141

Bibliography 142

Appendix A List of publications related to the thesis work 150

List of Figures

Figure 2.1 (a) Real (minus) and (b) imaginary (minus) parts of the permittivity function of Au; (c) real (minus) and (d) imaginary (minus) parts of the permittivity function of Ag; (e) real (minus) and (f) imaginary(minus) parts of the permittivity function of Cu: the black circles are experimental data taken from [48]; the black dot and dash lines are fitting curves with 4-pole Lorentz-Drude model (1 Drude pole pair and 1 Lorentz pole pair) and 6-pole Lorentz-Drude model (1 Drude pole pair and 2 Lorentz pole pairs), respectively; the solid red and blue lines are the fitting curves with 4-pole RDM and 6-pole RDM, respectively. 18

Figure 2.2 Relative errors of modeled permittivity of (a) Au, (b) Ag, and (C) Cu versus the number of poles in the models: the black line is the relative error of the Lorentz-Drude model, and the red line is the relative error of the RDM. 20

Figure 2.3 (a) Absorption cross-section (b) Scattering cross-section: the black circles are analytical solution with experimental data [48]; the black dash line is the FDTD solution with 1 Drude pole pair and 2 Lorentz pole pairs; the solid red and blue lines are the FDTD solutions with 4-pole RDM and 6-pole RDM, respectively. 23

Figure 2.4 Cross-section spectra of a gold nano-ellipsoid with a longer radius r2=20nm and two shorter radii r1=10nm: the green, red and blue lines are scattering, absorption and extinction cross-section, respectively. The electric field is polarized parallel to the longer radius. 27

Figure 2.5 Cross-section spectra of a gold nano-ellipsoid with a longer radius r2=20nm and two shorter radii r1=10nm: the green, red and blue lines are scattering, absorption and extinction cross-section, respectively. The magnetic field is polarized parallel to the longer radius. 27

Figure 2.6 Cross-section spectra of a gold nano-ellipsoid with all three radii equal to 20nm: the green, red and blue lines are scattering, absorption and extinction cross-section, respectively. 28

Figure 2.7 Cross-section spectra of a gold nano-ellipsoid with all three radii equal to 10nm: the green, red and blue lines are scattering, absorption and extinction cross-section, respectively. 28

Figure 2.8 Cross-section spectra of gold nano-ellipsoids with different radii and incident wave polarizations: (a) extinction, (b) scattering, (c) absorption. 29

Figure 2.9 Structure of nano-ellipsoid dimer 30

Figure 2.10 (a) Extinction, (b) scattering and (c) absorption cross-section spectra of the nano-ellipsoid dimer with different values of distance d from 0nm to 6nm. The electric field is polarized parallel to the aligned axis. 32

Figure 2.11 (a) Extinction, (b) scattering and (c) absorption cross-section spectra of the nano-ellipsoid dimer with difference values of distance d from 0nm to 6nm. The magnetic field is polarized parallel to the aligned axis. 33

Figure 2.12 (a) Extinction, (b) scattering and (c) absorption cross-section spectra of the nano-ellipsoid dimer with different background materials. The electric field is polarized parallel to the aligned axis. 34

Figure 2.13 Structure of a single nano-ellipse illuminated by an incident plane wave 35
Figure 2.14 (a) Extinction, (b) scattering and (c) absorption cross-section spectra of a nano-ellipse with incident wave illuminating from different directions.....36
Figure 2.15 (a) Extinction, (b) scattering and (c) absorption cross-section spectra of a nano-ellipse surrounded by different materials.....37
Figure 2.16 (a) Extinction, (b) scattering and (c) absorption cross-section spectra of a nano-ellipse with different raidus r2. 38
Figure 2.17 Structure of a nano-ellipse dimer illuminated by an incident plane wave 39
Figure 2.18 (a) Extinction, (b) scattering and (c) absorption cross-section spectra of a nano-ellipse dimer illuminated by incident wave from different angles. 40
Figure 2.19 (a) Extinction, (b) scattering and (c) absorption cross-section spectra of a nano-ellipse dimer with different values of distance between its two nano-ellipses. The angle alpha of the incident wave is 0 degree. 41
Figure 2.20 (a) Extinction, (b) scattering and (c) absorption cross-section spectra of a nano-ellipse dimer with different values of distance between its two nano-ellipses. The angle alpha of the incident wave is 90 degrees. 42
Figure 2.21 (a) Extinction, (b) scattering and (c) absorption cross-section spectra of a nano-ellipse dimer with different length of radius r2. The angle alpha of the incident wave is 90 degrees. 43
Figure 2.22 (a) Extinction, (b) scattering and (c) absorption cross-section spectra of a nano-ellipse dimer surrounded by different background materials. The angle alpha of the incident wave is 90 degrees. 44

Figure 2.23 Structure of a nano-ellipse trimer. 45
Figure 2.24 (a) Extinction, (b) scattering and (c) absorption cross-section spectra of a nano-ellipse trimer illuminated by incident wave from different angles. 46
Figure 2.25 (a) Extinction, (b) scattering and (c) absorption cross-section spectra of a nano-ellipse trimer with different values of d. The angle of the incident wave is 0 degree. 47
Figure 2.26 (a) Extinction, (b) scattering and (c) absorption cross-section spectra of a nano-ellipse trimer with different values of d. The angle of the incident wave is 60 degree. 48
Figure 2.27 (a) Extinction, (b) scattering and (c) absorption cross-section spectra of a nano-ellipse trimer with different length of radius r2. The angle of the incident wave is 0 degree. 49
Figure 2.28 (a) Extinction, (b) scattering and (c) absorption cross-section spectra of a nano-ellipse trimer surrounded by different materials. The angle of the incident wave is 0 degree. 50
Figure 3.1 The time domain waveform of a pulse with hyperbolic-secant function envelop 65
Figure 3.2 FDTD results of a pulse propagating in a linear dispersive media: the blue line is the spatial waveform after it has propagated $55\mu m$, the red line is the spacial waveform after it has propagated $126\mu m$ 65

Figure 3.3 FDTD results of a pulse propagating in a nonlinear dispersive media: the blue line is the spacial waveform after it has propagated $55\mu m$, the red line is the spacial waveform after it has propagated $126\mu m$ 66

Figure 3.4 Frequency spectrum of the main propagating soliton at spacial position $x=55\mu m$ (blue line) and $x=126\mu m$ (red line). 66

Figure 4.1 Gain profiles for different carrier densities: the dots are data calculated from theoretical gain model, the solid lines are fitted results through 2 RDM poles by using the RDM model. 74

Figure 4.2 Index profile along the longitudinal direction 80

Figure 4.3 Spontaneous emission at the beginning: the first figure is the random noise at different position of the laser, the second figure is the random noise monitored at outside of the left mirror versus time. 81

Figure 4.4 E-field evolution in the Fabry-Perot laser 81

Figure 4.5 Carrier density and output power evolution 82

Figure 4.6 Carrier density distribution in the laser cavity after lasing.....82

Figure 4.7 Electric field distribution in the laser cavity after lasing.....83

Figure 4.8 Electric field spectrum of the laser diode after lasing 83

Figure 4.9 Carrier density distrubution in the laser cavity if the carrier diffusion is neglected 84

Figure 4.10 Carrier density and output power evolution if the carrier diffusion is neglected 84

Figure 4.11 Gain and loss profile of a laser diode 85

Figure 4.12 Optical spectrum of a Fabry-Perot laser diode 86
Figure 4.13 3D structure of a Fabry-Perot laser etched with two ditches.....86
Figure 4.14 1D structure of a two-ditch band-pass filter 87
Figure 4.15 Power transmission and reflection spectra of a two-ditch band-pass filter. ...87
Figure 4.16 Longitudinal refractive index profile of a designed single mode laser structure 88
Figure 4.17 Optical spectrum of a designed laser diode 88
Figure 5.1 Schematic diagram of the square channel waveguide structure, $n_1 = 1.52$, $n_2 = 1.46$, $w_1 = 2\mu m$, PML Layers = 20.....100
Figure 5.2 Fundamental mode profile of the square channel waveguide. 101
Figure 5.3 Guided modal analysis by Goell's model and solver in this chapter. 102
Figure 5.4 Schematic diagram of a deep-etched GaAs-alGaAs optical waveguide structure. 103
Figure 5.5 TE20 mode profile of the ridge waveguide. 103
Figure 5.6 Percentage error of extracted wavelength of fundamental mode versus different FDTD time steps. 105
Figure 5.7 Percentage error of extracted wavelength of fundamental mode versus MPM sample numbers. 106
Figure 5.8 Memory consumptions of the scalar mode calculation by the accelerated FDTD and the conventional FD mode solvers. 108
Figure 5.9 Memory consumptions of the scalar, semi-vector and full-vector mode calculations by the accelerated FDTD solvers. 108

Figure 5.10 Time consumption of the scalar mode calculation by the standard FDTD, accelerated FDTD and the conventional FD mode solvers.....109
Figure 5.11 Time consumption of the scalar, semi-vector and full-vector mode calculations by accelerated FDTD mode solvers on GPUs. 110
Figure 6.1 (a) Partition of a structure of an optical band-pass filter 116
Figure 6.2 (a)The refractive index and 50 complex mode profiles of a 0.8um waveguide solved by a complex mode solver (b)The real and imaginary parts of the complex effective index of the first 50 complex modes. 118
Figure 6.3 (a) Results calculated by the mode orthogonality equation (b) Results calculated by the power orthogonality equation 119
Figure 6.4 A 0.8um waveguide with index=1.42 surrounded by air boxed in a PBR region with 3um thick PML. 120
Figure 6.5 The static state electric field of launching a complex mode at port #1: (a) mode #1 (b) mode #4 (c) mode #6.....120
Figure 6.6 The amplitude and phase of the electric field recorded at port 2 and the corresponding complex mode launched at port 1: (a) mode #1 (b) mode #4 (c) mode #6 122
Figure 6.7 Amplitudes of in-going and out-going complex modes at two ports of a building block 123
Figure 6.8 Amplitudes of in-going and out-going complex modes at two ports of an optical connector with length L 125
Figure 6.9 Two adjacent building blocks.....127

Figure 6.10 A band-pass filter consisting of two vertical ditches on a slab waveguide partitioned into 3 blocks: $n_0 = 3.218$, $n_1 = 3.260$, $n_2 = 1.0$, $a = 0.5\mu m$, $b = 2.0\mu m$ 129

Figure 6.11 Transmission (a) and reflection (b) coefficients of the first mode of the entire device: The red dots are the results calculated by the FDTD method, The blue dotted line, purple dash line and black solid line are the results calculated by the circuit theory with 1 mode, 3 modes and 10 modes, respectively, for the interconnection 130

Figure 6.12 A band-pass filter consisting of two vertical ditches on a slab waveguide partitioned into 5 blocks: $n_0 = 3.218$, $n_1 = 3.260$, $n_2 = 1.0$, $a = 0.5\mu m$, $b = 2.0\mu m$ 131

Figure 6.13 Transmission (a) and reflection (b) coefficients of the first mode of the entire device: The red dots are the results calculated by the FDTD method, The blue dotted line, purple dash line and black solid line are the results calculated by the circuit theory with 3 mode, 6 modes and 10 modes, respectively, for the interconnection 131

Figure 6.14 The relative error of the transmission coefficients versus the number of modes employed by the circuit model 132

Figure 6.15 Structure of a one-dimensional couple cavities photonic crystal filter: $N_{inner} = 9$, $N_{outer} = 4$, $h = 650nm$, $dH = 200nm$, $dL = 90nm$, and $D = 400nm$ 133

Figure 6.16 A one-dimensional couple cavities photonic crystal partitioned into 22 building blocks.....133

Figure 6.17 Transmission (a) and reflection (b) coefficients of the first mode of the 1D photonic crystal filter 134

Figure 6.18 The relative error of the transmission coefficients versus the number of modes employed by the circuit model 134

Figure 6.19 Schematic diagram for an optical square disk resonator. 135

Figure 6.20 Transmission spectrum of the fundamental mode at the input and output ports of the structure shown in Figure 6.19: the red circles are data of a FDTD simulation; the blue and green triangles, purple dash line, blue dot-line and black solid line are calculated by the circuit theory using 15, 20, 30, 40 and 50 complex modes for interconnections, respectively. 137

Figure 6.21 The electric field amplitude distribution of the entire structure when shining the 1.53um fundamental mode at the top left port. 137

List of Tables

Table 2.1 Coefficients of dispersion models.....9

Table 2.2 Values of the parameters for the Lorentz-Drude Model (Au) 20

Table 2.3 Values of the parameters for the RDM (Au) 21

Table 2.4 Computational costs and relative errors of different FDTD schemes.....24

Table 5.1 Leaky modal analysis by FD mode solver and solver in this chapter.....104

Chapter 1 Introduction

1.1 Motivation

Benefiting from rapid growth of computing capabilities, the Computer-Aided Design (CAD) becomes more and more popular in the development of optical devices and circuits. The photonic CAD technology [1, 2] offers a great opportunity for people to design and optimize a prototype quickly and accurately by simulating the behavior of lightwave in an optical component. It dramatically shortens the development cycle of products and reduces the overall cost. Several lightwave simulation methods, such as the Beam Propagating Method (BPM) [3-5], the Mode Matching Method (MMM) [6, 7], and the Couple Mode Theory (CMT) [8-10], the Finite-Difference Time-Domain (FDTD) method [11-13] and the Finite-difference Frequency-Domain (FDFD) method [14-16] have been widely adopted in academic researches and commercial software packages [17, 18]. The two semi-analytical methods of CMT and MMM are quite computationally efficient, but they can only be applied to devices with particular geometries or refractive index profiles. The BPM based on a reduced form of Maxwell's equations is only accurate in solving paraxial propagation problems. The FDFD method is a rigorous numerical method for the simulation of electromagnetic field in frequency-domain. However, its demanding of computer memory increases extremely fast with the increase of the simulation domain size. This prevents its practical use in three-dimensional (3D) or large scale problems.

The FDTD method is one of the most frequently and widely used method in photonic simulation and verification. It is rigorous, generally applicable and versatile in simulation of both 2D and 3D structures of various materials. It has the ability to simulate the optical characteristics in multi-wavelength in one run, which is very efficient in a lot of applications [19, 20]. However, the FDTD method is quite memory and time consuming when employed to simulate large scale structures. It is hard for a single modern personal computer to afford such a task, because it requires too much computing resources. Although the FDTD method can be implemented to execute on multiple computers in parallel [21, 22], there is a big burden on computing resources used for exchanging data between the corresponding computers involved in the computation. Therefore, it is strongly desirable to improve the computational efficiency of the FDTD method in simulation of various materials for optical devices.

Circuit theory [23-26] is a good way to dramatically reduce the requirement of computing resources in analysis of large scale structures. It avoids dealing with an entire large scale structure by partitioning it into small building blocks. In the conventional circuit theory, only guided modes [27] in the waveguides connecting each building block are considered, while radiation effects in the connecting waveguides are neglected. Nowadays, the compact optical devices and high density integrated optical circuits are more and more widely used [28-31]. It is highly desirable to have a new circuit theory that carefully takes the radiation effects into account to significantly increase the accuracy in analysis of theses optical devices and circuits.

1.2 Overview of the Thesis and Contributions of the Research

This thesis consists of seven chapters and a bibliography. The first chapter is introduction and the last chapter is about conclusion and future work. The main body of this thesis is from Chapter 2 to 6. The contributions corresponding to the work in each chapter are described as follows.

In Chapter 2, a novel rational dispersion model, referred to as the Rational Dispersion Model (RDM) with a parameter estimation method is proposed for the simulation of optical properties of arbitrary linear dispersive media over a wide wavelength range. The conventional Debye, Drude and Lorentz models are derivable from this more general model. The time domain properties of the proposed model are analyzed. It is demonstrated that the rational model can fit the relative permittivity data of a material accurately and efficiently in a wide wavelength range and the parameters of this model can be estimated requiring no initial guess. The new model is implemented in the FDTD method as a powerful and computationally efficient tool for simulating nano-particles of dispersive materials in a wide wavelength range of light. By employing this model, a systematic study of the optical properties of different nano-particles gives a good reference for designs of optical devices utilizing the cross-section spectra characteristics of nano-particles, such as optical sensors, optical filters, heat sinks, etc.

In Chapter 3, the second-order nonlinearity and the third-order nonlinearity including Raman effect and Kerr effect are studied and implemented in the FDTD method. The RDM is integrated into the nonlinear FDTD scheme to handle the linear polarization part. The implemented FDTD method is verified by simulating of a 1D-temporal soliton.

It is useful for simulating of optical devices consisting of nonlinear materials such as poled glasses with the second-order nonlinearity and silicon materials with nonlinear effects resulting from the third-order susceptibility.

In Chapter 4, the FDTD method and the rate equation model are employed to simulate the semiconductor lasers having arbitrary cavity geometries. The RDM is proposed to model the gain materials for efficiency and feasibility. A new method based on Newton iteration is proposed to discretize the carrier rate equation. It serves as an efficient and accurate tool for the simulation of semiconductor laser. The proposed model is proved to be an efficient and accurate method in design of semiconductor lasers having arbitrary cavity geometries.

In Chapter 5, a two-dimensional (2D) compact FDTD mode solver is developed based on wave equation formalism in combination with the matrix pencil method (MPM). The method is validated by calculation of both real guided and complex leaky modes of typical optical waveguides against the bench-mark Finite-Difference (FD) eigen mode solver. Taking advantage of the inherent parallel nature of the FDTD algorithm, the mode solver is implemented on graphics processing units (GPUs) using the compute unified device architecture (CUDA). It is demonstrated that the high-performance computing technique leads to significant acceleration of the FDTD mode solver. The computational efficiency of the accelerated FDTD method is in the same order of magnitude of the standard FD eigen mode solver but requires much less memory.

In Chapter 6, a circuit theory based on the complex mode expansion is proposed for analysis of large scale optical devices and circuits. The new circuit theory was verified

by a two-ditch band-pass filter. It shows that the new circuit theory significantly improves the accuracy due to consideration of the radiation effects using the complex mode expansion of fields at the ports of interconnections. This theory even works for the building blocks whose ports located at an open space where only complex radiation modes exist. The proposed circuit theory is a powerful and versatile tool for analysis of large scale optical devices and circuits.

Chapter 2 FDTD Method for Dispersive Materials

2.1 Introduction

Dispersive materials, such as semiconductors and metals, are widely used in optical devices. The Finite-Difference Time-Domain (FDTD) method [11] is one of the most common choices for simulating such devices in a wide frequency range. One of the most important advantages of the FDTD method is that the broadband response can be accurately obtained in only one simulation run [32]. Several simple phenomenological models, such as multi-pole Debye, Drude, and Lorentz models, have been widely adopted for modeling dispersive materials using the FDTD method [33-37]. To fit permittivity function of a given material accurately in a wide frequency range, a large number of poles are required in these models. Rakic and Djurisic used the Durde model with up to five Lorentzian terms to fit the permittivity functions of eleven metals [38]. Hao and Nordlander proposed an improved model consisting of four Lorentzian terms to fit dielectric data of gold and silver [19]. All the proposed multi-pole models archived good fit to the measure data. However, using a dispersion model with a large number of poles not only requires a lot of efforts for modal parameter estimation but also dramatically increases the memory and computational costs of the FDTD method [39]. Han, Dutton and Fan proposed a complex-conjugate pole-residue pair model and implemented it in the FDTD method to increase the modeling efficiency [40, 41]. However, these authors did not propose an efficient method for the parameters estimation. Etchegoin, Ru and Meyer proposed an analytical model with one Drude term and two critical points to model the

optical properties of gold [42]. However, these authors did not show how to estimate the eleven parameters of this model.

A new model, referred to as the Rational Dispersion Model (RDM) is proposed in this chapter for efficiently modeling of arbitrary linear dispersive materials. The proposed model is much more efficient than the conventional Debye, Drude, and Lorentz models, because it offers more degrees of freedom in parameter estimation. In addition, a generally applicable parameter estimation method is proposed for this model to efficiently and accurately fit the permittivity function. The rational dispersion model is implemented in the FDTD method. Both the memory and computational costs of the FDTD method for broadband dispersive material simulation are dramatically reduced.

This chapter is organized as follows. The RDM and its numerical implementation in the FDTD method are described in sections 2 and 3, respectively. The parameter estimation method is demonstrated in section 4. The implemented FDTD method is verified by simulating a metal nanowire in section 5. The application of the proposed method to analyze optical properties of nano-particles is demonstrated in section 6.

2.2 Rational Dispersion Model

2.2.1 Introduction

Assuming the time harmonic dependence $\exp(j\omega t)$, the RDM is proposed to describe the dispersive material's relative permittivity expressed by the rational fraction form as

$$\varepsilon_r(\omega) = \frac{\sum_{k=1}^{N} a_k (j\omega)^k}{\sum_{k=1}^{N} b_k (j\omega)^k} \tag{2.1}$$

where a_k and b_k are real numbers. The rational fraction form is the ratio of two polynomials $\sum_{k=1}^{N} a_k (j\omega)^k$ and $\sum_{k=1}^{N} b_k (j\omega)^k$, where the highest order of the denominator is the same as that of the numerator. The parameters a_k and b_k of the two polynomials can be estimated accurately and quickly by a rational approximation method and employed as a good initial guess for the material permittivity curve fitting method proposed in the later section of this chapter. To be conveniently adopted by the FDTD method, the RDM model is represented by its partial fraction expansion described by

$$\begin{aligned} \varepsilon_r(\omega) &= \varepsilon_\infty + \sum_{k=1}^{L} \chi_k(\omega) \\ \chi_k(\omega) &= \begin{cases} \dfrac{r_k}{j\omega - p_k}; if\ p_k\ is\ real \\ \dfrac{r_k}{j\omega - p_k} + \dfrac{r_k^*}{j\omega - p_k^*}; if\ p_k\ is\ \text{complex} \\ \sum_{u=1}^{U} \dfrac{r_{k,u}}{(j\omega - p_k)^u}; if\ p_k\ is\ \text{a multiple root} \end{cases} \end{aligned} \tag{2.2}$$

where ε_∞, r_k, and p_k are the direct coefficient, residue, and pole, respectively. The partial fraction term $\chi_k(\omega)$ is the frequency domain susceptibility function. It has three forms depending on the properties of the pole p_k: 1) a real fraction term with a real residue and a real pole, when p_k is a real number; 2) two complex fraction terms consist of complex conjugate residue and pole pairs, when p_k is a complex number; and 3) a summation of fraction terms which contains high order (>1) of $j\omega$, when p_k is a multiple root of the

denominator $\sum_{k=1}^{N} b_k (j\omega)^k$. It is observed that the third expression of P_k should be avoided in the parameter estimation procedure because the high order (the order of $j\omega$ is higher than one) partial fraction terms make it difficult to implement this model in the FDTD method. If there are L_1 real poles and L_2 complex conjugate pole pairs, the upper bound of the summation in equation (2.2) is $L = L_1 + L_2$, and the total pole number is $N = L_1 + 2L_2$.

Table 2.1 shows relationships of the RDM with other dispersion models.

Table 2.1 Coefficients of dispersion models

$\varepsilon_r(\omega)$	L	p_k	r_k	p_{k+1}	r_{k+1}
Debye model $\varepsilon_\infty + \sum_{p=1}^{N_p} \frac{\Delta\varepsilon_p}{j\omega\gamma_p + 1}$	N_p	$-1/\gamma_k$	$\frac{\Delta\varepsilon_k}{\gamma_k}$	-	-
Drude model $\varepsilon_\infty + \sum_{p=1}^{N_p} \frac{\omega_p^2}{-\omega^2 + j\omega\gamma_p}$	$2N_p$	0	$\frac{\omega_p^2}{\gamma_p}$	$-\gamma_p$	$-\frac{\omega_p^2}{\gamma_p}$
Lorentz model $\varepsilon_\infty + \sum_{p=1}^{N_p} \frac{\Delta\varepsilon_p \omega_p^2}{-\omega^2 + 2j\omega\gamma_p + \omega_p^2}$	N_p	$-\gamma_p - j\sqrt{\omega_p^2 - \gamma_p^2}$	$r_k = j\frac{\Delta\varepsilon_p \omega_p^2}{2\sqrt{\omega_p^2 - \gamma_p^2}}$ $(\omega_p > \gamma_p)$	-	-
Complex-conjugate pole-residue pair model $\varepsilon_\infty + \sum_{k=1}^{N_p} \left(\frac{r_k}{j\omega - p_k} + \frac{r_k^*}{j\omega - p_k^*} \right)$	N_p	Complex number	Complex number	-	-
Critical points model $\varepsilon_\infty + \sum_{p=1}^{N_p} A_p \omega_p \left(\frac{e^{i\phi_p}}{\omega_p - \omega - j\gamma_p} + \frac{e^{-i\phi_p}}{\omega_p + \omega + j\gamma_p} \right)$	N_p	$\gamma_p + j\omega_p$	$-jA_p\omega_p e^{i\phi_p}$	-	-

It shows that Debye, Drude, and Lorentz models are all special cases of RDM with specified parameters. The RDM treats the Debye, Drude, and Lorentz materials in a

unified formulation, which simplifies the implementation of dispersion models in numerical simulation algorithms such as the FDTD method. It also shows that when p_k is a complex number, the partial fraction form of the RDM is the same as the complex-conjugate pole-residue pair model. The RDM can also be converted to the critical points model through parameter substitution. The advantages of the RDM, including its easy implementation in the FDTD method and the generally applicable parameter estimation process, will be demonstrated in the later sections.

2.2.2 The RDM Oscillator

Similar to the conventional phenomenological dispersion models, the RDM describes the macroscopic susceptibility of a material. It is also very interesting to study the mechanism of the RDM from the microscopic view. When p_k is a real number, the susceptibility function has the same form as the Debye model. Therefore, in this case, the RDM susceptibility has the same physical meaning as that of the Debye model which is the medium relaxation response of an ideal and non-interacting group of dipoles to an applied varying electric field. When p_k is a complex number, each term of the susceptibility function can be reformed as

$$\chi_k(\omega) = \frac{\left(r_k + r_k^*\right) j\omega + \left(-r_k p_k^* - r_k^* p_k\right)}{-\omega^2 - \left(p_k + p_k^*\right) j\omega + p_k p_k^*} \qquad (2.3)$$

The corresponding polarization $\tilde{\mathbf{P}}_k(\omega)$ of this medium due to an applied electric field $\tilde{\mathbf{E}}(\omega)$ is described by

$$\tilde{\mathbf{P}}_k = \chi_k(\omega)\tilde{\mathbf{E}} = \frac{\left(r_k + r_k^*\right) j\omega + \left(-r_k p_k^* - r_k^* p_k\right)}{-\omega^2 - \left(p_k + p_k^*\right) j\omega + p_k p_k^*}\tilde{\mathbf{E}} \qquad (2.4)$$

The macroscopic polarization $\tilde{\mathbf{P}}_k(\omega)$ of the medium is given by the summation over all dipole moments as

$$\tilde{\mathbf{P}}_k = \frac{N}{V}(-e\tilde{\mathbf{x}}) \tag{2.5}$$

where e, N, V, and $\tilde{\mathbf{x}}$ are the elementary charge, the number of dipoles, the volume of all the dipoles, and the displacement vector, respectively. Substituting equation (2.5) into (2.4) and after an obvious rearrangement, a new equation of the displacement vector is expressed as

$$\left[-\omega^2 - \left(p_k + p_k^*\right) j\omega + p_k p_k^*\right]\tilde{\mathbf{x}} = -\frac{V}{eN}\left[\left(r_k + r_k^*\right) j\omega + \left(-r_k p_k^* - r_k^* p_k\right)\right]\tilde{\mathbf{E}} \tag{2.6}$$

The corresponding time domain equation is obtained by inverse Fourier transforming and rearranging equation(2.6), yielding

$$\beta(-e)\frac{d\mathbf{E}}{dt} + \alpha(-e)\mathbf{E} + \delta\frac{d\mathbf{x}}{dt} - k\mathbf{x} = m_0\frac{d^2\mathbf{x}}{dt^2} \tag{2.7}$$

where

$$\alpha = \frac{m_0 V}{e^2 N}\left(-r_k p_k^* - r_k^* p_k\right)$$
$$\beta = \frac{m_0 V}{e^2 N}\left(r_k + r_k^*\right)$$
$$\delta = m_0\left(p_k + p_k^*\right)$$
$$k = m_0\left(p_k p_k^*\right)$$

This formula is the motion equation of a system referred to as the "RDM oscillator". It is noticed that this equation is very similar to the motion equation of a Lorentz oscillator of the Lorentz medium which describes the dispersive medium as a population of spring bounded electrons on nucleus. The motion equation of the Lorentz oscillator is given by

$$\alpha(-e)\mathbf{E}+\delta\frac{d\mathbf{x}}{dt}-k\mathbf{x}=m_0\frac{d^2\mathbf{x}}{dt^2} \tag{2.8}$$

where

$$\alpha=\frac{\Delta\varepsilon_p\omega_p^2 V m_0}{e^2 N}=1$$
$$\delta=-2m_0\gamma_p$$
$$k=m_0\omega_p^2$$

Comparing equation (2.7) with (2.8), it is easy to find that the only difference of the two equations is that equation (2.7) has an extra term $\beta(-e)\frac{d\mathbf{E}}{dt}$ while equation (2.8) does not. Therefore, in this case when p_k is a complex number, the RDM describes a population of RDM oscillators moving under the action of the instantaneous electric filed $\mathbf{E}$, as well as its derivative $d\mathbf{E}/dt$. From the mathematical point of view, the RDM oscillator offers more degrees of freedom compared with the Lorentz oscillator. If the RDM's parameter r_k is purely imaginary, the coefficient β in equation (2.7) becomes zero. Correspondingly, the RDM oscillator degenerates to the Lorentz oscillator.

2.2.3 Analysis of the RDM in Time Domain

To study properties of the RDM in time domain, the inverse Fourier transformation is performed on the frequency domain susceptibility function $\chi_k(\omega)$ defined in equation (2.2). If p_k is a real number, the time domain susceptibility is expressed by

$$\chi_k(t)=r_k e^{p_k t}U(t) \tag{2.9}$$

where $U(t)$ is the unit step function. It shows that when $p_k>0$, the susceptibility is exponentially growing with time, which contradicts the phenomenon that the lightwave is

decaying when propagating in lossy materials, such as metals and semiconductors. Thus, the parameter p_k should not be greater than zero when modeling lossy materials in this model. If p_k is a complex number, the frequency domain susceptibility can be reformed as

$$\chi_k(\omega) = \frac{\left(-r_k p_k^* - r_k^* p_k\right)}{-\omega^2 - \left(p_k + p_k^*\right) j\omega + p_k p_k^*} + j\omega \frac{\left(r_k + r_k^*\right)}{-\omega^2 - \left(p_k + p_k^*\right) j\omega + p_k p_k^*} \qquad (2.10)$$

The time domain susceptibility is obtained by taking the inverse Fourier transformation, as expressed by

$$\chi_k(t) = \zeta_k e^{-\alpha_k t} \sin(\kappa_k t) U(t) + \frac{d}{dt}\left[\xi_k e^{-\alpha_k t} \sin(\kappa_k t) U(t)\right] \qquad (2.11)$$

where

$$\alpha_k = -\frac{p_k + p_k^*}{2} = -\mathrm{Re}(p_k)$$
$$\kappa_k = \sqrt{p_k p_k^* - \alpha_k^2}$$
$$\zeta_k = \frac{-r_k p_k^* - r_k^* p_k}{\kappa_k}$$
$$\xi_k = \frac{r_k + r_k^*}{\kappa_k}$$

It is noteworthy that when the real part of p_k is positive ($\mathrm{Re}(p_k) > 0$), the parameter α_k is negative ($\alpha_k < 0$). The time domain susceptibility $\chi_k(t)$ will grow exponentially with time, which contradicts the property of the lossy materials. The above analysis comes out a natural conclusion that the real part of the pole parameter p_k must be no bigger than zero ($\mathrm{Re}(p_k) \le 0$) when using the RDM to model lossy dispersive materials.

2.3 Implementation of the RDM in the FDTD Method

The RDM can be easily and efficiently implemented in the FDTD method with an auxiliary differential equation (ADE) scheme. In Maxwell's equations, Ampere's law in frequency domain is expressed by

$$j\omega\varepsilon_0\varepsilon_\infty\tilde{\mathbf{E}}+\sigma\tilde{\mathbf{E}}+\sum_{k=1}^{L}\tilde{\mathbf{J}}_k=\nabla\times\tilde{\mathbf{H}} \tag{2.12}$$

where $\tilde{\mathbf{J}}_k$ is the polarization current related with each term in the summation of the RDM, defined by

$$\tilde{\mathbf{J}}_k = j\omega\varepsilon_0\tilde{\mathbf{E}}\begin{cases}\dfrac{r_k}{j\omega-p_k};\ if\ \ p_k\ \ is\ real\\ \dfrac{r_k}{j\omega-p_k}+\dfrac{r_k^*}{j\omega-p_k^*};\ if\ \ p_k\ \ is\ \text{complex}\end{cases} \tag{2.13}$$

As mentioned previously, the multiple-root p_k should be avoided in the parameter estimation procedure, so that it would not be concerned with the difficult implementation of polarization current in the multiple-root p_k case.

If p_k is real, r_k is also real. Then the time-domain polarization current is real and given by

$$\frac{\partial\mathbf{J}_k}{\partial t}-p_k\mathbf{J}_k=r_k\varepsilon_0\frac{\partial\mathbf{E}}{\partial t} \tag{2.14}$$

If p_k is complex, r_k is also complex. The time-domain polarization current has two parts $\mathbf{J}_k$ and $\mathbf{J}_k'$, corresponding to the two complex poles in equation(2.13). The two polarization currents are all complex and given by

$$\frac{\partial\mathbf{J}_k}{\partial t}-p_k\mathbf{J}_k=r_k\varepsilon_0\frac{\partial\mathbf{E}}{\partial t} \tag{2.15}$$

$$\frac{\partial\mathbf{J}_k'}{\partial t}-p_k^*\mathbf{J}_k'=r_p^*\varepsilon_0\frac{\partial\mathbf{E}}{\partial t} \tag{2.16}$$

Because $\mathbf{E}(t)$ is real, if the initial values for the two polarization current are the same, the two parts are mutual complex conjugate, i.e. $\mathbf{J}_k' = \mathbf{J}_k^*$ [40]. Only one complex equation, either equation (2.15) or (2.16), needs to be computed in the FDTD calculation. In the following derivation, equation (2.15) is employed. Therefore, when p_k is complex, the real part of the time domain polarization current is $\mathrm{Re}\left[\mathcal{F}^{-1}\left(\tilde{\mathbf{J}}_k\right)\right] = 2\,\mathrm{Re}\left(\mathbf{J}_k\right)$. By applying the inverse Fourier transform on both sides of equation(2.12), the time domain Ampere's curl equation is obtained as

$$\varepsilon_0\varepsilon_\infty \frac{\partial}{\partial t}\mathbf{E} + \sigma\mathbf{E} + \sum_{k=1}^{L} m\,\mathrm{Re}\left(\mathbf{J}_k\right) = \nabla\times\mathbf{H} \tag{2.17}$$

where $m = 1$ if p_k is real; $m = 2$ if p_k is complex. The time domain polarization current equation and Ampere's curl equation are combined together and discretized in the explicit FDTD scheme, yielding

$$\mathbf{E}\,|^{n+1/2} = C_a\mathbf{E}\,|^{n-1/2} + C_b\left[\nabla\times\mathbf{H}\,|^{n} - \mathrm{Re}\left(\sum_{k=1}^{L}\frac{m}{2}\left(1+k_p\right)\mathbf{J}_k\,|^{n-1/2}\right)\right] \tag{2.18}$$

$$\mathbf{J}_k\,|^{n+1/2} = k_k\mathbf{J}_k\,|^{n-1/2} + \beta_k\left(\frac{\mathbf{E}\,|^{n+1/2} - \mathbf{E}\,|^{n-1/2}}{\Delta t}\right) \tag{2.19}$$

where

$$\begin{aligned}
&k_k = \frac{2+p_k\Delta t}{2-p_k\Delta t};\ \beta_k = \frac{2r_k\varepsilon_0\Delta t}{2-p_k\Delta t}\\
&C_a = \frac{2\varepsilon_0\varepsilon_\infty - \sigma\Delta t + \mathrm{Re}\sum_{k=1}^{L}\left(m\beta_k\right)}{2\varepsilon_0\varepsilon_\infty + \sigma\Delta t + \mathrm{Re}\sum_{k=1}^{L}\left(m\beta_k\right)};\ C_b = \frac{2\Delta t}{2\varepsilon_0\varepsilon_\infty + \sigma\Delta t + \mathrm{Re}\sum_{k=1}^{L}\left(m\beta_k\right)}\\
&m = \begin{cases} 1; & \textit{if } p_k \textit{ is real} \\ 2; & \textit{if } p_k \textit{ is complex} \end{cases}
\end{aligned} \tag{2.20}$$

The discretization of the magnetic field $\mathbf{H}|^{n+1}$ is the same as it is in the standard FDTD algorithm[11]. This is an efficient implementation of the RDM in the FDTD method. With the same number of poles, the RDM takes no additional memory and computational costs for updating the auxiliary equations of the polarization currents compared with the conventional dispersion models such as multi-pole Lorentz-Drude model. However, the RDM offers more degrees of freedom in fitting a permittivity function in the parameter estimation process. Thus, the implementation of the RDM in the FDTD method is far more computationally efficient compared to those of Lorentz-Drude model. This implementation is much easier than the critical points model implementation of recursive convolution method [43] or ADE method [44] in which the Drude and the critical point expressions are implemented separately with different derivations.

2.4 Parameter Estimation of the RDM

The RDM is an analytical function that describes the relative permittivity of a dispersive material. To fit a given relative permittivity curve accurately and quickly, a parameter estimation procedure is highly demanded in obtaining a good initial guess for the starting point and locate a good approximation to the global optimum. The advantage of the rational fraction form of the RDM in equation (2.1) lies in the fact that a very good initial guess of parameters a_k and b_k can be quickly obtained using the rational approximation method [45, 46]. After that, the initial values of the residues r_k, poles p_k, and direct coefficient ε_∞ are obtained from the parameters a_k and b_k by converting the RDM from the rational fraction form to the partial fraction form. Finally, the initial values

are employed in a simulated annealing algorithm [47] to find the optimized values of parameters ε_∞, p_k and r_k. The high efficiency of the RDM is demonstrated in modeling metal materials Au (gold), Ag (silver) and Cu (copper) in a wide range of wavelength from 400 to 1100 nm. The measured relative permittivity of these three metals [48] is fitted using four dispersion models: the 4-pole Lorentz-Drude model (1 Drude pole pair and 1 Lorentz pole pair), the 6-pole Lorentz-Drude model (1 Drude pole pair and 2 Lorentz pole pairs), the RDM with 4 poles, and the RDM with 6 poles. The Lorentz-Drude model is expressed in the equation

$$\varepsilon_r(\omega) = \varepsilon_\infty + \frac{\omega_D^2}{-\omega^2 + j\omega\gamma_D} + \sum_{l=1}^{N_L} \frac{\Delta\varepsilon_l \omega_l^2}{-\omega^2 + 2j\omega\gamma_l + \omega_l^2} \qquad (2.21)$$

where the numbers of Drude, and Lorentz pole pairs are one, and N_L, respectively. As it is shown in Figure 2.1, both the Lorentz-Drude model and the RDM achieve better accuracy with more number of poles. However, the RDM overwhelms the Lorentz-Drude model with significant improvement of accuracy while with the same number of poles. Moreover, for some materials such as Au and Cu, the RDM with 4 poles fits the experimental data to a higher accuracy than that of the 6-pole Lorentz-Drude model, while having much lower computational cost. The RDM with 6 poles performs a much more accurate fit than the 6-pole Lorentz-Drude model, while having the same computational cost.

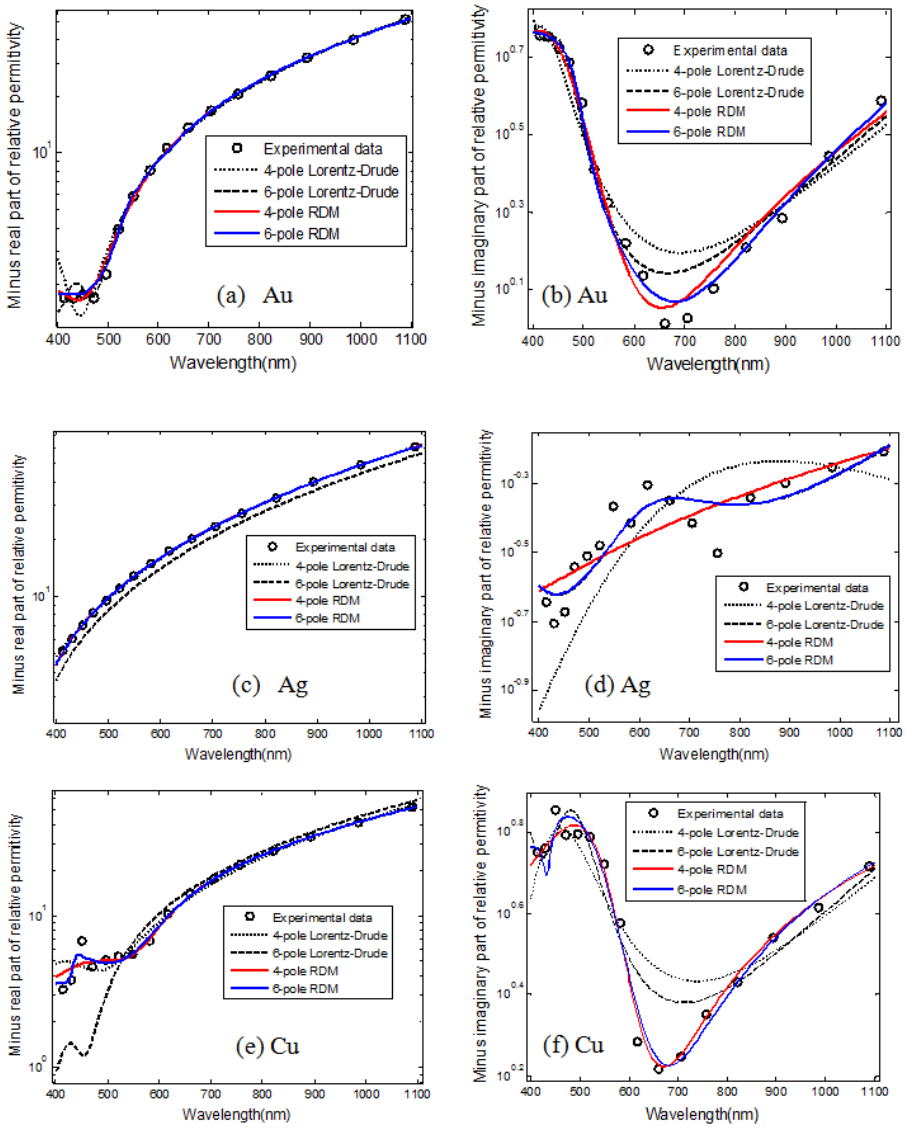

Figure 2.1 (a) Real (minus) and (b) imaginary (minus) parts of the permittivity function of Au; (c) real (minus) and (d) imaginary (minus) parts of the permittivity function of Ag; (e) real (minus) and (f) imaginary(minus) parts of the permittivity function of Cu: the black circles are experimental data taken from [48]; the black dot and dash lines are fitting curves with 4-pole Lorentz-Drude model (1 Drude pole pair and 1 Lorentz pole pair) and 6-pole Lorentz-Drude model (1 Drude pole pair and 2 Lorentz pole pairs),

respectively; the solid red and blue lines are the fitting curves with 4-pole RDM and 6-pole RDM, respectively.

To demonstrate the advantages of the RDM in terms of the modeling accuracy, a convergence test of the RDM is performed on the three metal materials Au, Ag and Cu. The convergence of the RDM is studied by measuring the relative errors of the modeled permittivity with increasing the number of poles. The relative error of the modeled permittivity to the experimental data is defined by

$$e_{rel} = \frac{\sqrt{\sum_{i=1}^{N} \left| \varepsilon^{\exp}(\omega_i) - \varepsilon(\omega_i) \right|^2}}{\sqrt{\sum_{i=1}^{N} \left| \varepsilon^{\exp}(\omega_i) \right|^2}} \qquad (2.22)$$

Figure 2.2 depicts the relative errors of the RDM and the Lorentz-Drude mode in modeling the permittivity of the metal materials Au, Ag and Cu. It shows that when increasing the number of poles, both the RDM and the Lorentz-Drude model reduce the relative error. However, the RDM model converges faster than the Lorentz-Drude model. The parameters of the Lorentz-Drude model and the RDM model for modeling material Au are listed in Table 2.2 and Table 2.3, respectively.

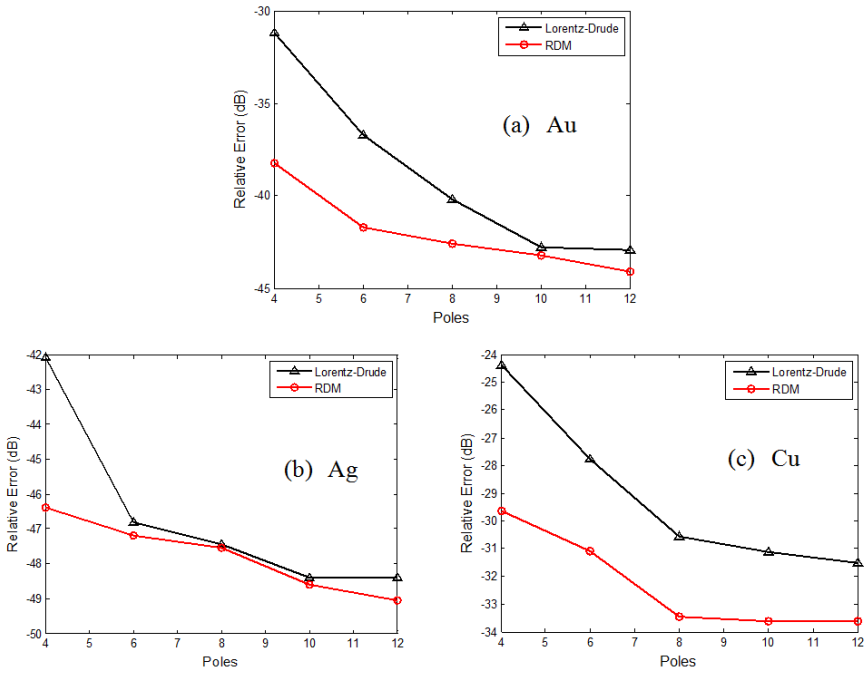

Figure 2.2 Relative errors of modeled permittivity of (a) Au, (b) Ag, and (C) Cu versus the number of poles in the models: the black line is the relative error of the Lorentz-Drude model, and the red line is the relative error of the RDM.

Table 2.2 Values of the parameters for the Lorentz-Drude Model (Au)

Parameters	1 Drude 1 Lorentz	1 Drude 2 Lorentz	1 Drude 3 Lorentz	1 Drude 4 Lorentz	1 Drude 5 Lorentz
ε_∞	6.069	5.035	2.541	1.000	1.000
ω_D (eV)	8.829	8.739	8.646	8.229	8.225
γ_D (eV)	5.617e-2	6.274e-2	6.596-2	1.035e-7	3.539-8
$\Delta\varepsilon_1$	1.930	7.360e-1	8.834e-1	1.190	5.324e-1
ω_1 (eV)	3.038	2.750	3.075	3.088	2.678
γ_1 (eV)	5.034e-1	2.858e-1	3.053e-1	3.870e-1	2.635e-1
$\Delta\varepsilon_2$	-	1.309	1.910	2.901	2.896
ω_2 (eV)	-	3.316	3.932	4.285	4.280
γ_2 (eV)	-	3.494e-1	5.859e-9	1.276e-9	1.892e-7
$\Delta\varepsilon_3$	-	-	6.520e-1	5.288e-1	1.184
ω_3 (eV)	-	-	2.688	2.677	3.088

γ_3 (eV)	-	-	2.686e-1	2.629e-1	3.857e-1
$\Delta\varepsilon_4$	-	-	-	9.679	9.799
ω_4 (eV)	-	-	-	7.594e-1	7.573e-1
γ_4 (eV)	-	-	-	2.420e-1	2.412e-1
$\Delta\varepsilon_5$	-	-	-	-	1.109e-6
ω_5 (eV)	-	-	-	-	2.736e-1
γ_5 (eV)	-	-	-	-	8.050e-2

Table 2.3 Values of the parameters for the RDM (Au)

Parameters	4-pole RDM	6-pole RDM	8-pole RDM	10-pole RDM	12-pole RDM
ε_∞	2.988	1.000	1.366	1.000	1.000
p_1 (eV)	-1.745e-2 -1.079e-2i	-2.356e-2 -8.549e-2i	-3.719e-10 -9.473e-2i	-1.484e-9 -1.364e-1i	-4.216e-9 -1.054e-1i
r_1 (eV)	1.464 +3.397e+3 i	1.533 +4.210e+2 i	2.308 +3.710e+2 i	8.279e-1 +2.603e+2 i	-2.018 +3.430e+2 i
p_2 (eV)	-1.745e-2 +1.079e-2i	-2.356e-2 +8.549e-2i	-3.719e-10 +9.472e-2i	-1.484e-9 +1.364e-1i	-4.216e-9 +1.054e-1i
r_2 (eV)	1.464 -3.397e+3i	1.533 -4.210e+2i	2.308 -3.710e+2i	8.279e-1 -2.603e+2i	-2.018 -3.430e+2i
p_3 (eV)	-6.805e-1 -2.602i	-2.329e-1 -2.521i	-1.716e-10 -1.037i	-9.667e-9 -9.334e-1i	-6.634e-10 -7.769e-1i
r_3 (eV)	3.686 +1.660i	3.873e-1 +3.146e-2i	1.354e-1 +7.042e-2i	5.839e-1 +9.971e-2i	2.251 +2.487e-1i
p_4 (eV)	-6.805e-1 +2.602i	-2.329e-1 +2.521i	-1.716e-10 +1.037i	-9.667e-9 +9.334e-1i	-6.634e-10 +7.769e-1i
r_4 (eV)	3.686 -1.660i	3.873e-1 -3.146e-2i	1.354e-1 -7.042e-2i	5.839e-1 -9.971e-2i	2.251 -2.487e-1i
p_5 (eV)	-	-1.186 -2.390i	-2.127e-1 -2.508i	-1.366e-1- 2.461i	-2.254e-1 -2.335i
r_5 (eV)	-	7.246 +1.796e-1i	3.156e-1 -2.150e-2i	8.992e-2 -6.297e-2i	-4.081e-1 +6.295e-2i
p_6 (eV)	-	-1.186 +2.390i	-2.127e-1 +2.508i	-1.366e-1 +2.461i	-2.254e-1 +2.335i
r_6 (eV)	-	7.246 -1.796e-1i	3.156e-1 +2.150e-2i	8.992e-2 +6.297e-2i	-4.081e-1 -6.295e-2i
p_7 (eV)	-	-	-1.040 -2.358i	-7.099e-1 -2.564i	-3.450e-1 -2.455i
r_7 (eV)	-	-	6.141	3.408	1.585

			-2.946e-1i	+1.755i	+3.928e-1i
p_8 (eV)	-	-	-1.040 +2.358i	-7.099e-1 +2.564i	-3.450e-1 +2.455i
r_8 (eV)	-	-	6.141 +2.946e-1i	3.408 -1.755i	1.585 -3.928e-1i
p_9 (eV)	-	-	-	-8.789e-10 -4.533i	-3.486e-1 -3.661i
r_9 (eV)	-	-	-	-2.085e-1 +3.024i	-9.571 +2.662i
p_{10} (eV)	-	-	-	-8.789e-10 +4.533i	-3.486e-1 +3.661i
r_{10} (eV)	-	-	-	-2.085e-1 -3.024i	-9.571 -2.662i
p_{11} (eV)	-	-	-	-	-4.312e-10 -3.815i
r_{11} (eV)	-	-	-	-	7.567 +5.354i
p_{12} (eV)	-	-	-	-	-4.312e-10 +3.815i
r_{12} (eV)	-	-	-	-	7.567 -5.354i

2.5 Verification of the FDTD Method with the RDM

The FDTD method is a rigorous numerical tool for simulating nano-particle problems by solving Maxwell's equations accurately. However, it is extremely memory and time consuming when dealing with metal nano-structures in the wavelength range of light due to two reasons: 1) the small feature size of the structure requires very fine meshes and time steps; and 2) the complicated dispersion property dramatically increases the implementation complexity and computational cost. Therefore, it is strongly desired to have a simulation tool, which can accurately model the wide band dispersion properties, yet taking an affordable computation effort. The RDM is implemented in 2D and 3D FDTD methods for simulating of nano-structures.

To exam the efficiency of the RDM with different numbers of poles, the light wave scattering phenomenon of an Au nano-wire with 40 nm diameter surrounded by air is simulated by the 2D FDTD method with the RDM in a wide wavelength range from 400 to 1100 nm. The CPML [49] is employed to truncate the computation window. A uniform mesh size of 0.5 nm is employed and 20,000 time steps are performed. Figure 2.3 shows the cross-section curves calculated using the analytical solution, the FDTD method with 1 Drude pole pair and 2 Lorentz pole pairs(scheme 1), the FDTD method with the 4-pole RDM(scheme 2), and the FDTD method with the 6-pole RDM(scheme 3), respectively. Table 2.4 lists the memory and computational costs of different FDTD schemes, as well as the relative errors of the extinction cross-section compared with the analytical solution. It shows that compared with the conventional Lorentz-Drude model, the FDTD method with the 4-pole RDM achieves a smaller relative error while taking much less computational effort, and the FDTD method with the 6-pole achieves even better accuracy yet maintaining a comparable computational cost.

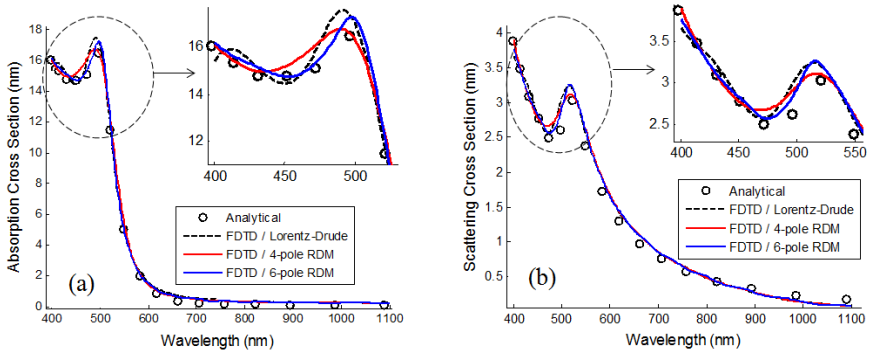

Figure 2.3 (a) Absorption cross-section (b) Scattering cross-section: the black circles are analytical solution with experimental data [48]; the black dash line is the FDTD solution

with 1 Drude pole pair and 2 Lorentz pole pairs; the solid red and blue lines are the FDTD solutions with 4-pole RDM and 6-pole RDM, respectively.

Table 2.4 Computational costs and relative errors of different FDTD schemes

	Scheme 1 (1 Drude pole pair and 2 Lorentz pole pairs)	Scheme 2 (4 RDM poles)	Scheme 3 (6 RDM poles)
Memory (mega-byte)	6.600	5.872	6.604
Computation time (second)	694.58	599.26	702.04
Relative error (dB) (Extinction cross-section)	-23.97	-25.31	-26.04

It proves that the new model is more efficient in terms of memory and computational costs in modeling dispersive materials in comparison with conventional phenomenological models. It is a powerful and efficient tool for simulating broadband optical phenomena of nano-particles with dispersive materials.

2.6 Analysis of Metal Nano-particles

Optical properties of the nano-particles have been given a lot of attention in these years. The lightwave phenomena of nano-particles such as scattering, absorption, field enhancement, etc. have been intensively studied [50-57]. McMahon and Smajic studied the properties of the triangle and rectangular nano-wire dimers, respectively, with the 2D FDTD method [57, 58]. In paper [59], Talley and Jackson demonstrated the properties of a dimer consists of two gold nano-spheres using the Mie's approximation and the 3D

FDTD method. Simulating of a nano-ellipsoid dimer requires extensive computing resources and is not intensively reported. A numerical algorithm is highly demanded for accurate and efficient simulation of the interactions between nano-particles and the lightwave. Mie's theory [50, 53, 60] has been employed to efficiently solve the particle extinction problems. However it is only accurate for analyzing a single spherical or cylinder particle. The FDTD method[11, 61-63] is a powerful numerical tool for simulating nano-particle problems by solving Maxwell's equations accurately[64, 65]. However, the FDTD method is extremely memory and time consuming when dealing with metal nano-structures. The reasons are two-folded: 1) very fine meshes both in space and time domain have to be used due to the small feature size of the structure [66]; 2) complicated dispersive material models such as the multi-pole Drude-Lorentz model are often required for precisely modeling of metal properties in the lightwave range [38]. Therefore, it is strongly desired to have a model which can accurately model the optical broadband material properties, yet maintaining an affordable computation effort. Meanwhile, it is highly demanded to significantly accelerate the simulation process without jeopardizing the simulation accuracy.

In this section, the rational dispersion model (RDM) is employed for modeling material properties of metal nano-particles in the lightwave range with the FDTD method. It improves the accuracy of material modeling while does not increase the computing cost of the FDTD method. Convolution perfectly matched layer (CPML) [67, 68] absorbing boundary conditions (ABCs) are employed in order to reduce the computation region. Since the FDTD method is an inherently data-parallel algorithm, it is implemented and

run on Graphics Processing Units (GPUs) by using Nvidia's Compute Unified Device Architecture (CUDA)[69]. With the help of the high computing power brought by GPUs[65], the simulation time of the FDTD method is further reduced to less than 10% of that used for the implementation on a standard desktop CPU. The optical properties such as distinction cross-section and electric field enhancement of nano-ellipses are simulated by the accelerated 2D FDTD method and those of nano-ellipsoids are simulated by the accelerated 3D FDTD method. The parameters employed for modeling the gold material with RDM in the FDTD method are the same as it is listed in Table 2.3.6 poles are used in the RDM for all the simulations.

2.6.1 Simulation of Single Nano-ellipsoid

The simulation results of the optical scattering properties of a gold nano-ellipsoid with different radii surrounding by air are produced by the three-dimensional (3D) FDTD method combined with the RDM. In the 3D FDTD simulation, a uniform mesh size of 1.0 nm is employed and 30,000 time steps are performed. Figure 2.4 shows the scattering, absorption and extinction cross-section spectra of a gold nano-ellipsoid with a longer radius r2=20nm and two shorter radii r1=20nm surrounded by air. It is illuminated by a plane wave propagating perpendicular to the longer radius and electric field polarized parallel to the longer radius. Figure 2.5 gives the cross-section spectra of the same nano-ellipsoid illuminated. However, at this time, the magnetic field of the incident plane wave is polarized parallel to the longer radius, thus the electric field is polarized parallel to the shorter radius. The cross-section spectra of a gold nano-sphere with 20nm radius and a gold nano-sphere with 10nm radius are depicted in Figure 2.6 and 2.7, respectively.

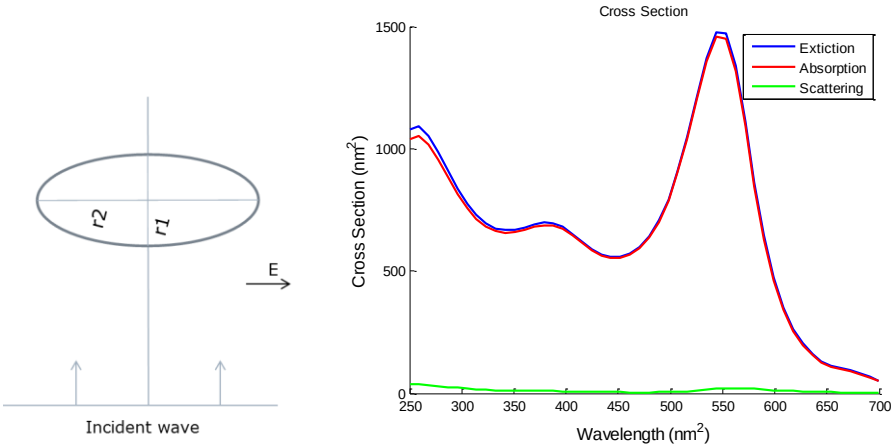

Figure 2.4 Cross-section spectra of a gold nano-ellipsoid with a longer radius r2=20nm and two shorter radii r1=10nm: the green, red and blue lines are scattering, absorption and extinction cross-section, respectively. The electric field is polarized parallel to the longer radius.

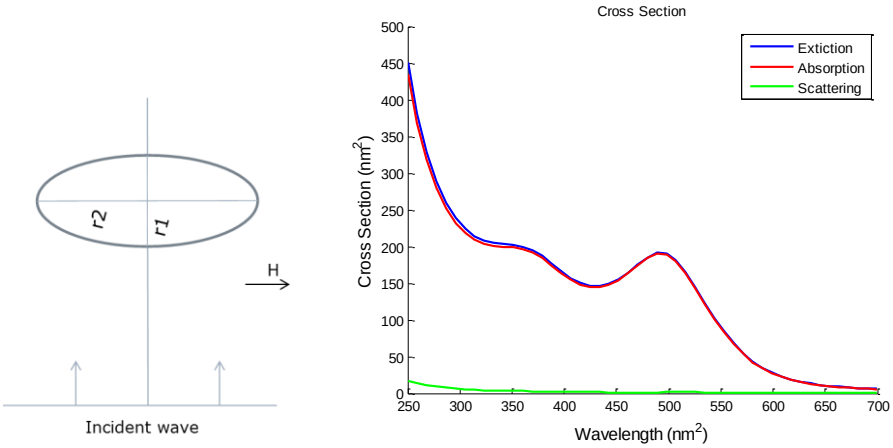

Figure 2.5 Cross-section spectra of a gold nano-ellipsoid with a longer radius r2=20nm and two shorter radii r1=10nm: the green, red and blue lines are scattering, absorption and extinction cross-section, respectively. The magnetic field is polarized parallel to the longer radius.

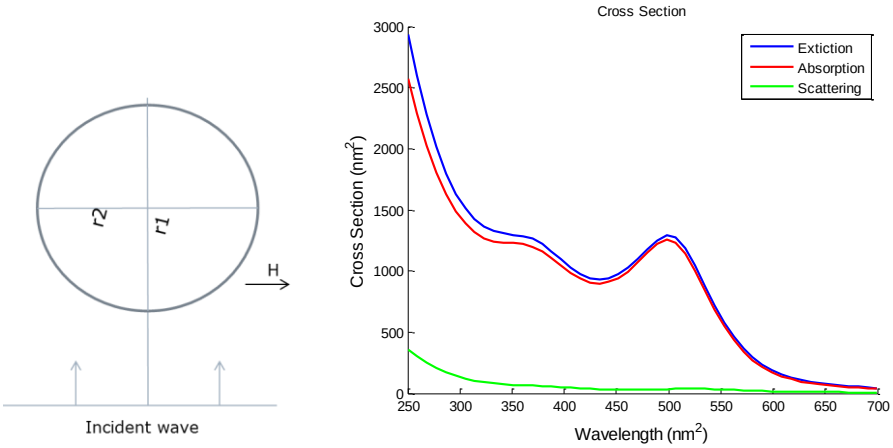

Figure 2.6 Cross-section spectra of a gold nano-ellipsoid with all three radii equal to 20nm: the green, red and blue lines are scattering, absorption and extinction cross-section, respectively.

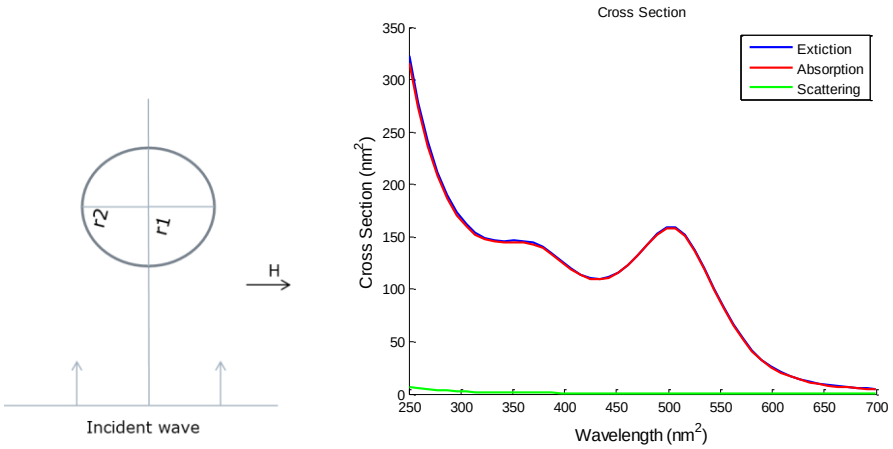

Figure 2.7 Cross-section spectra of a gold nano-ellipsoid with all three radii equal to 10nm: the green, red and blue lines are scattering, absorption and extinction cross-section, respectively.

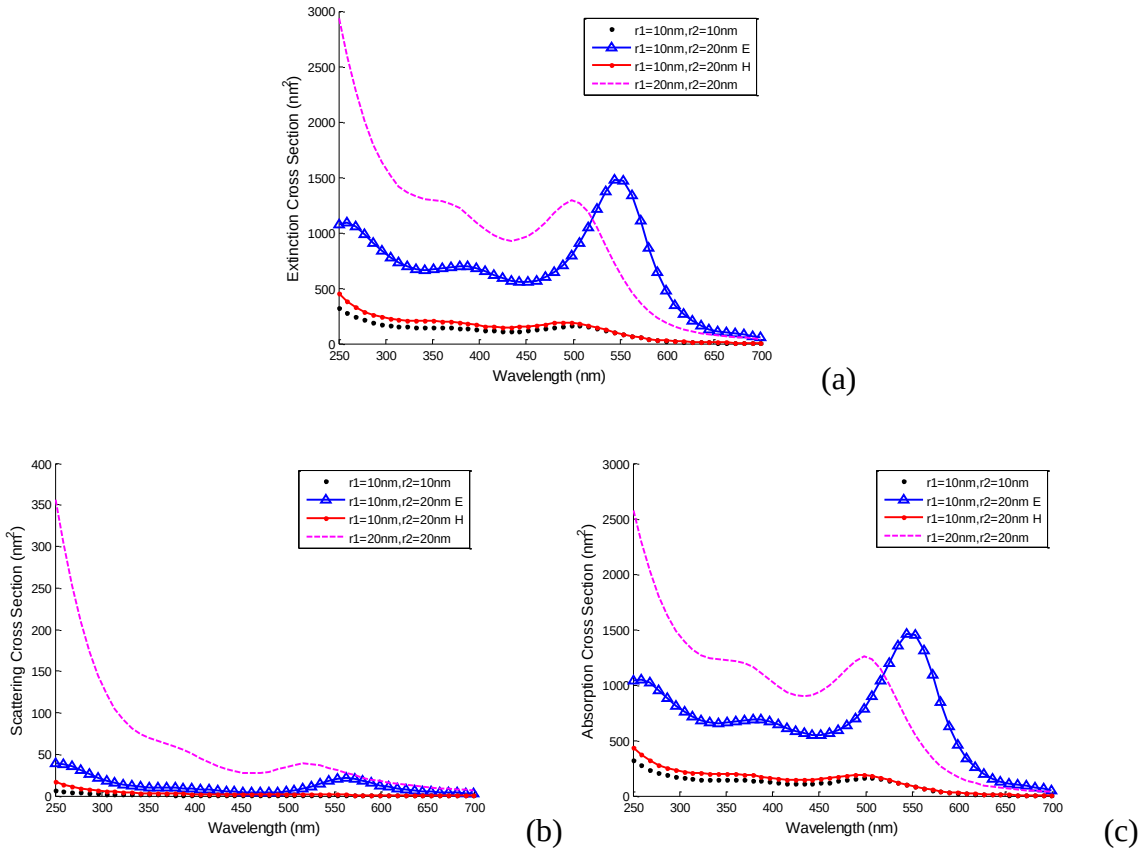

Figure 2.8 Cross-section spectra of gold nano-ellipsoids with different radii and incident wave polarizations: (a) extinction, (b) scattering, (c) absorption.

In Figure 2.8 the extinction, scattering and absorption cross-section spectra of nano-ellipsoids with above four different configurations are compared and depicted in Figure (a), (b) and (c), respectively. Figure 2.8 (b) shows that the scattering effect is enhanced by the volume of the nano-particle. Comparing the blue dots and the red dot-line in Figure 2.8 (c), one can realize that although the radius of the nano-particle parallel to the magnetic field polarization is doubled, the absorption cross-section is not enlarged very much. However, when the radius parallel to the electric field polarization is doubled, the absorption is dramatically enhanced as shown by the blue triangle-line in Figure 2.8 (c).

From the comparison of Figure 2.8 (c) one can conclude that the absorption effect is mainly affected by the length of the radius which is parallel to the direction of the electric field polarization.

2.6.2 Simulation of Nano-ellipsoid Dimer

The 3D FDTD method accelerated by the high performance GPU hardware with parallel computing techniques is used to analyze the optical properties such as the extinction cross-section and the electric field enhancement of a gold nano-ellipsoid dimer. The configuration of the nano-ellipsoid dimer is shown in Figure 2.9. It consists of two nano-ellipsoids aligned at the same axis along the longer radius r2. The other two radii are the same, named r1. The distance between nearest points of the two ellipsoids is marked as d. The incident plane wave is propagating toward the direction perpendicular to the shared axis of r2.

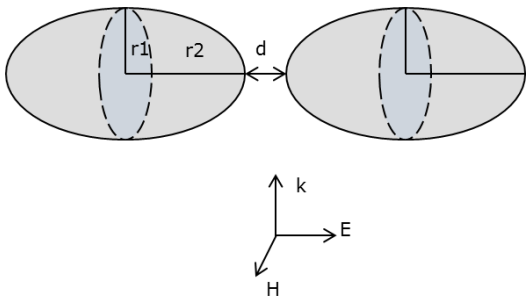

Figure 2.9 Structure of nano-ellipsoid dimer

The optical properties of this dimer with different values of distance are first studied by the 3D FDTD simulation. The radius r1 and r2 of the dimer in this simulation are 10nm and 20nm, respectively. The dimer is surrounded by air (refraction index=1.0) . A

uniform mesh size of 1nm is employed and 30,000 time steps are performed. Two cases are considered regarding the polarization direction of the incident wave. In the first case, the plane wave is propagating towards the dimer with electric field parallel to the longer radius r2 and magnetic field perpendicular to r2. The extinction, scattering and absorption cross-sections are depicted in Figure 2.10 (a), (b) and (c), respectively. It shows that with the decrease of distance d, the peaks of the three cross-sections all increase. The peak positions are blue shifted with the increase of the distance, which means the plasmonic resonance frequency of the dimer moves to shorter wavelengths with the increase of the two particles distance. In the other case, the magnetic field is polarized along the common axis and electric field is polarized perpendicular to it. Figure 2.11 (a), (b) and (c) depict the extinction, scattering and absorption cross-sections, respectively. It shows all the cross-sections do not change along with the change of the distance between the two ellipsoids. From the comparison of the two cases, one comes to a conclude that the plasmonic resonant phenomenon of a dimer is affected dramatically by changing the distance between the two ellipsoids only when a significant portion of electric field is polarized along the common axis of the two particles.

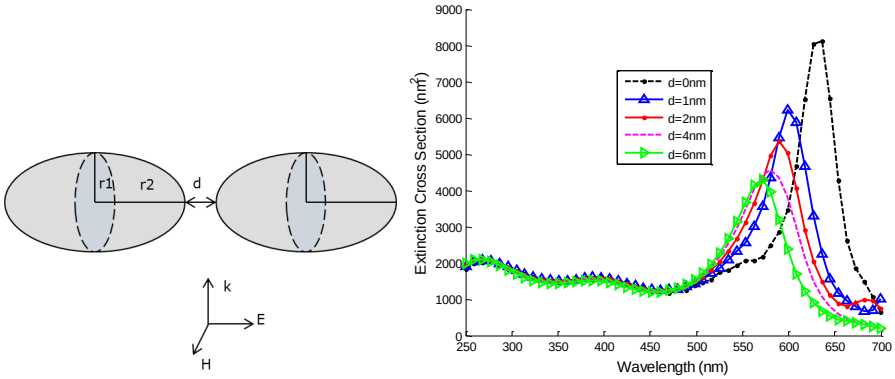

(a)

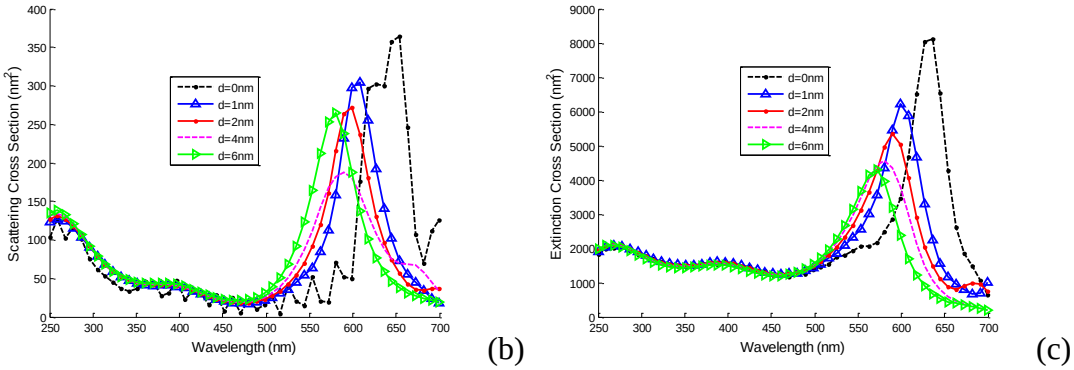

Figure 2.10 (a) Extinction, (b) scattering and (c) absorption cross-section spectra of the nano-ellipsoid dimer with different values of distance d from 0nm to 6nm. The electric field is polarized parallel to the aligned axis.

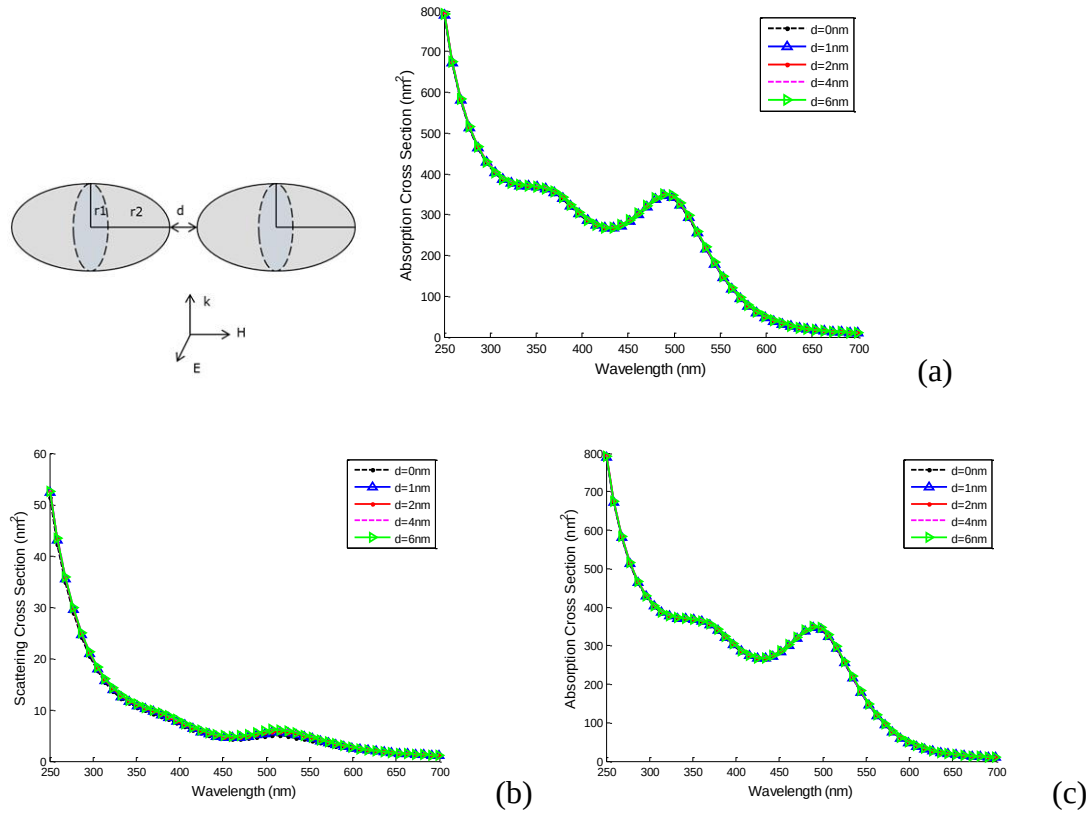

Figure 2.11 (a) Extinction, (b) scattering and (c) absorption cross-section spectra of the nano-ellipsoid dimer with difference values of distance d from 0nm to 6nm. The magnetic field is polarized parallel to the aligned axis.

The optical properties of this dimer surrounded by different background materials are also studied in the 3D FDTD method. The radius r1 and r2 of the dimer in this simulation are 10nm and 20nm, respectively. The background materials are air, water, silica and polymer with refraction index of 1.00, 1.33, 1.40, and 1,49, respectively. The incident plane wave is propagating towards the dimer with electric field parallel to the longer radius r2. A uniform mesh size of 1nm is employed and 30,000 time steps are performed. The absorption, scattering and extinction cross-sections are shown in Figure 2.12 (a), (b) and (c), respectively. It shows that with the increase of the background index, the peaks of the three cross-sections all increase and the peak positions are red shifted. It means the plasmonic resonance frequency of this dimer moves to the long wavelengths with the increase of the surrounded material index. The peak positions are located in the visible light range when surrounded by the other four low refraction index materials in the simulation. From the trends showing in Figure 2.12, one can predict that the resonance peak is located in the infrared range if it is surrounded by silicon with refractive index value around 3.2.

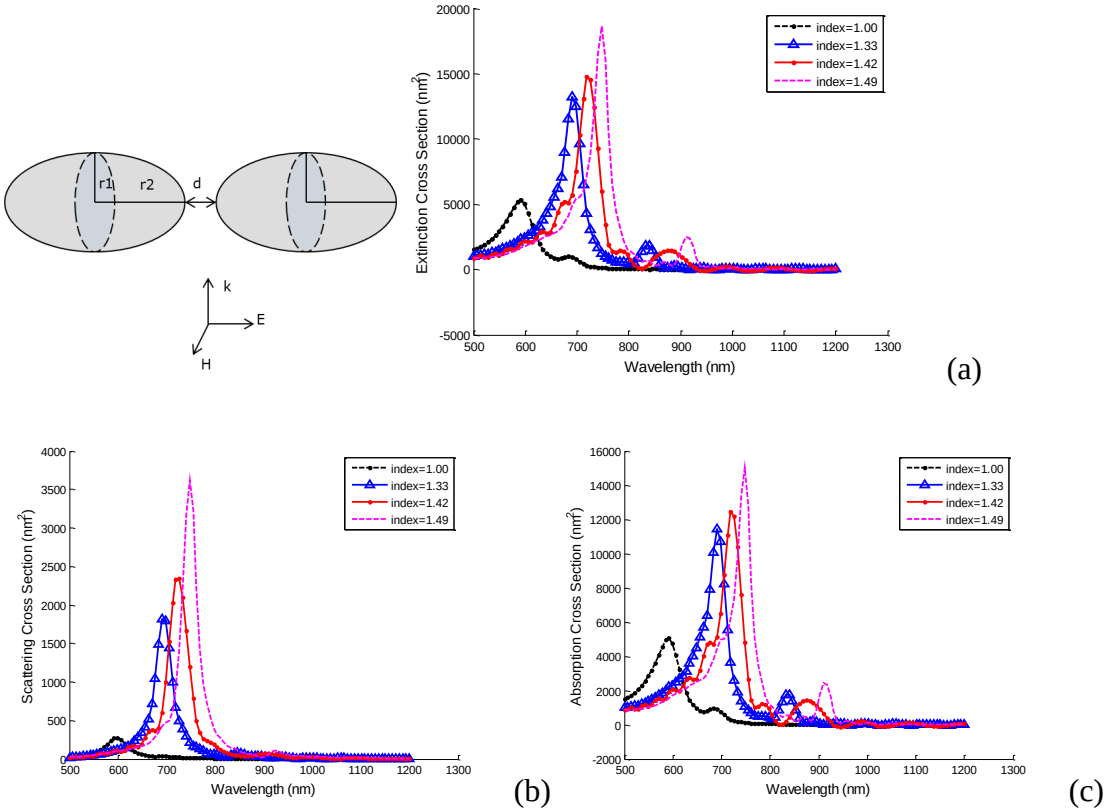

Figure 2.12 (a) Extinction, (b) scattering and (c) absorption cross-section spectra of the nano-ellipsoid dimer with different background materials. The electric field is polarized parallel to the aligned axis.

2.6.3 Simulation of Single Nano-ellipse

The optical properties such as the extinction cross-section of a gold nano-ellipse with different configurations regarding the differences of sizes, incident wave angle and background materials are simulated using the 2D FDTD method accelerated by the high performance GPU hardware with parallel computing technique. The TM polarization is used in the 2D FDTD simulations. The structure of the nano-ellipse is showed in Figure

2.13. It has a longer radius r2 and a shorter radius r1. The nano-ellipse is illuminated by an incident plane wave propagating toward it with an angle of alpha to the r2 axis.

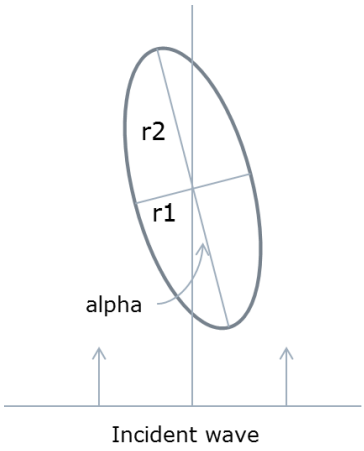

Figure 2.13 Structure of a single nano-ellipse illuminated by an incident plane wave

The optical properties of this particle are studied in three cases. In the first case, the nano-ellipse with a longer radius r2=20nm and a shorter radius r1=10nm is surrounded by air. The plane wave propagates toward it from different directions, which means the angle alpha changes to different values. Figure 2.14 (a), (b) and (c) depict the extinction, scattering and absorption cross-section, respectively, with angle alpha varying from 0 degree to 90 degree. It shows that the peaks of all the three cross-sections increase with angle size changing from 0 to 90 degrees. When the longer axis of the nano-ellipse aligns with electric field polarization direction (alpha=90 degrees), the peaks reach the maximum. However, the peak positions in the spectra do not change in the simulations.

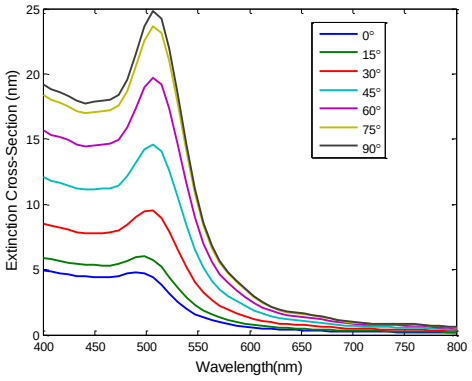

(a)

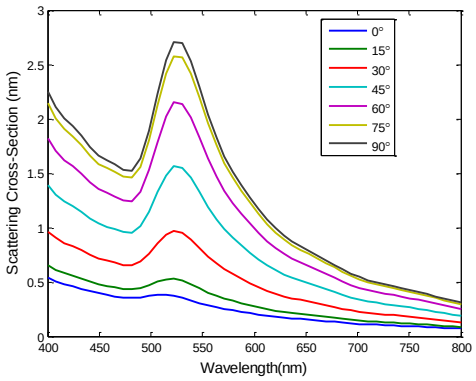

(b)

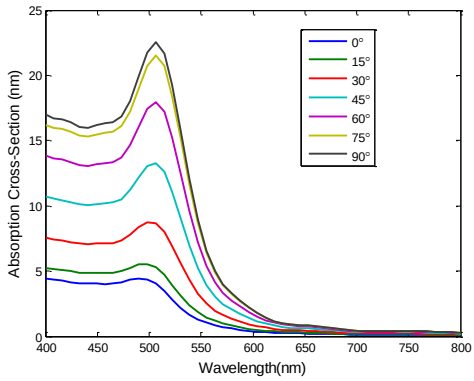

(c)

Figure 2.14 (a) Extinction, (b) scattering and (c) absorption cross-section spectra of a nano-ellipse with incident wave illuminating from different directions.

In the second case, the nano-ellipse has the same size as that in the first case and the electric field of the incident wave is polarized to the direction in the longer radius axis (alpha=90 degrees). However, different surrounded materials such as air (index=1.0), water (index=1.33), silica (index=1.42), Polymethyl Methacrylate (index=1.49) and silicon (index=3.2) are used in the simulations. The extinction, scattering and absorption cross-sections are depicted in Figure 2.15 (a), (b) and (c), respectively. It shows that peaks of the cross-sections increase along with the increase of the background material refractive index. The only one exception is absorption spectrum when the particle is

surrounded by silicon with refractive index as 3.2. Its peak is no larger than those of all the other spectra with lower surrounded material refractive indices. With the increase of the background refractive index, the peak positions in the spectra are shifted to the long wavelengths (red shift).

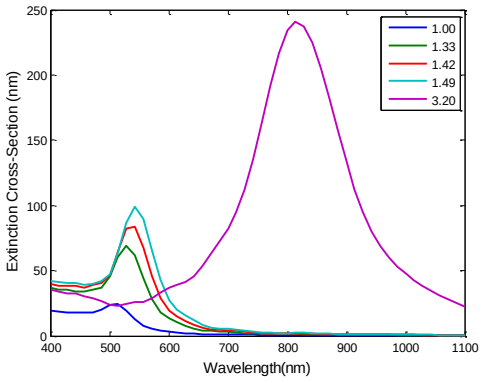

(a)

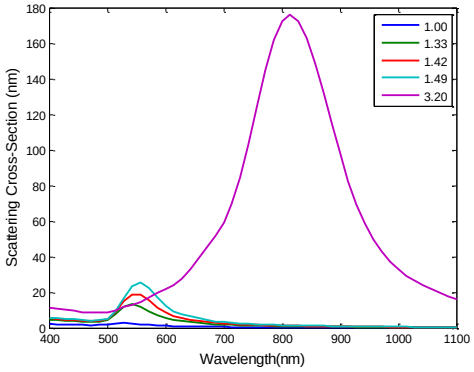

(b)

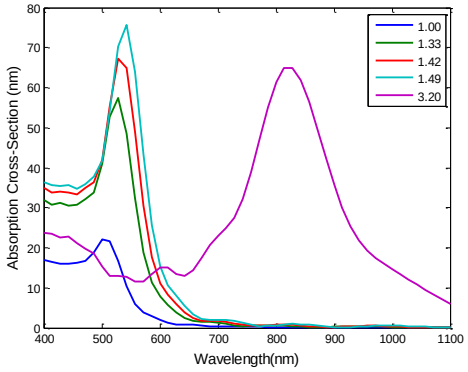

(c)

Figure 2.15 (a) Extinction, (b) scattering and (c) absorption cross-section spectra of a nano-ellipse surrounded by different materials.

In the third case, one radius of the nano-ellipse is r1=10nm. The other radius r2 varies from 10nm to 30nm. The particle is surrounded by air. The angle alpha is 90 degrees. The extinction, scattering and absorption cross-sections are depicted in Figure 2.16 (a), (b)

and (c), respectively. It shows clearly that the peaks of the cross-sections increase with the increase of the radius size r2, but the peak positions are not sensitive.

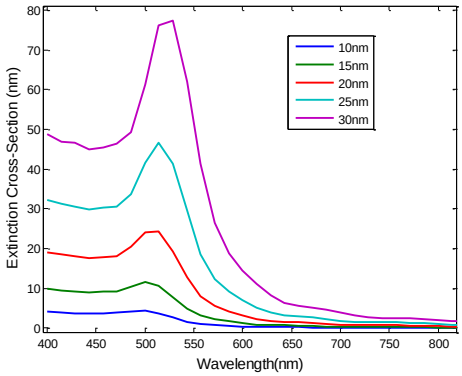

(a)

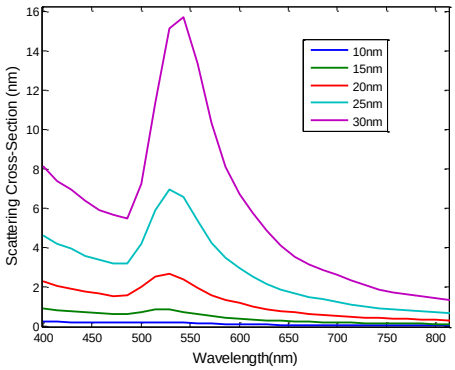

(b)

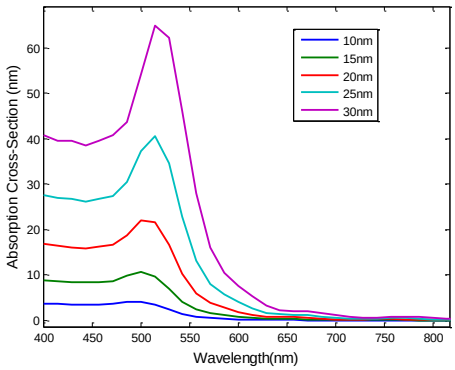

(c)

Figure 2.16 (a) Extinction, (b) scattering and (c) absorption cross-section spectra of a nano-ellipse with different raidus r2.

2.6.4 Simulation of Nano-ellipse Dimer

The optical properties of a gold nano-ellipse dimer shown in Figure 2.17 are simulated using the 2D FDTD method with TM polarization. The dimer consists of two identical nano-ellipses with a longer radius r2 and a shorter radius r1. The two nano-ellipses are aligned in the same axis of the radius r2. The incident plane wave propagates

toward the dimer with an angle of alpha to the common axis. The distance between the nearest points on the two nano-ellipses is d.

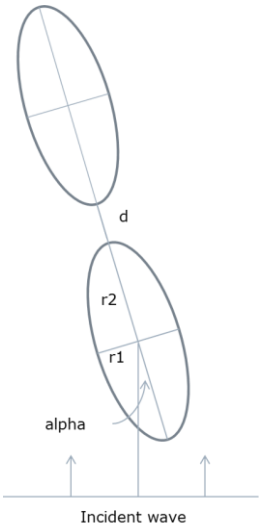

Figure 2.17 Structure of a nano-ellipse dimer illuminated by an incident plane wave

The optical properties of this nano-ellipse dimer are demonstrated in four cases. In the first case, the incident angle alpha is scanned from 0 degree to 90 degrees. The dimmer is surrounded by air with r1=10nm and r2=20nm. The distance between the two nano-ellipses is d=2nm. Figure 2.18 gives the extinction, scattering and absorption cross-section spectra for different incident angles in (a), (b) and (c), respectively. It shows that the peaks of the cross-section spectra keep increasing when alpha varies from 0 to 90 degrees but the peak positions do not change accordingly. This trend is the same as that we observed in Figure 2.14 of the single nano-ellipse simulation.

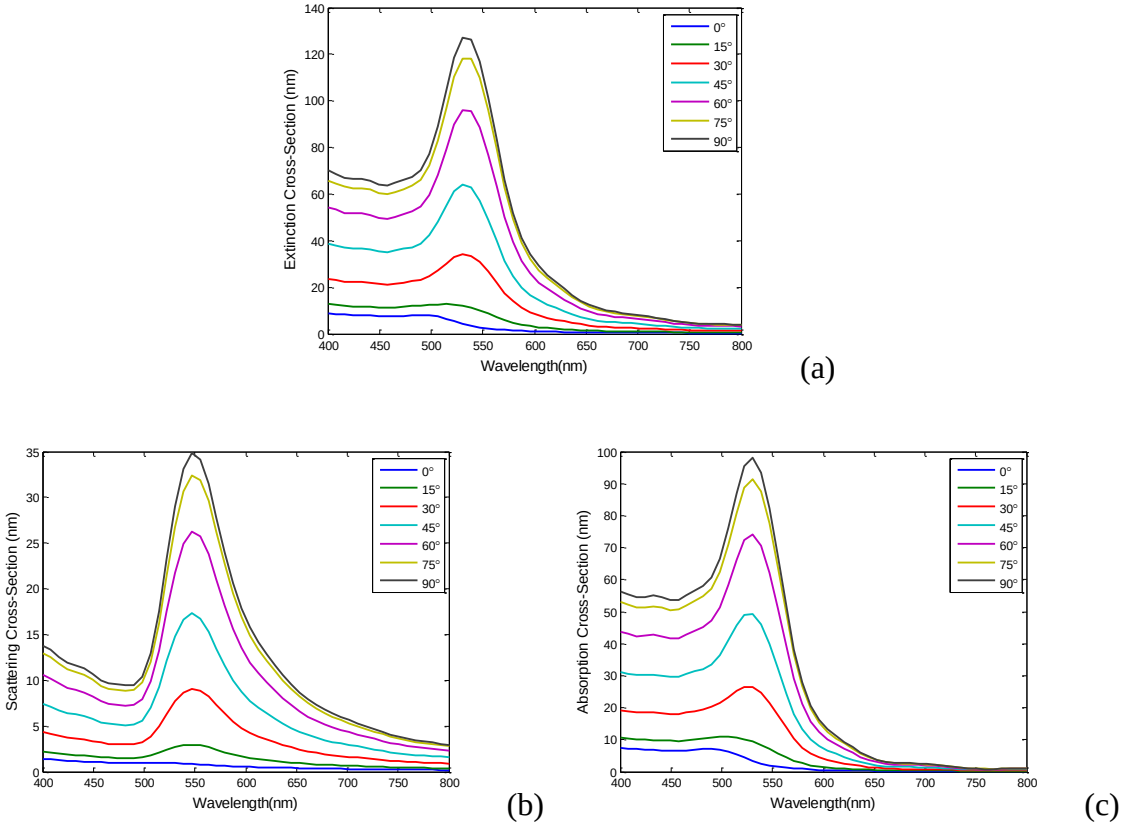

Figure 2.18 (a) Extinction, (b) scattering and (c) absorption cross-section spectra of a nano-ellipse dimer illuminated by incident wave from different angles.

In the second case, the distance d between the two nano-ellipse in the dimer varies from 2nm to 6nm. The dimer is surrounded by air with r1=10nm and r2=20nm. Figure 2.19 shows the cross-section spectra for different values of d from 2nm to 6nm when the incident wave propagating along the common axis (alpha=0 degree). Figure 2.20 shows the corresponding cross-section spectra when the incident wave propagating along the direction perpendicular to the common axis (alpha=90 degrees). It shows the cross-section spectra are much more sensitive to the change of the distance d in the situation where the electric field polarization is parallel to the common axis (alpha=90 degrees)

than that in the situation where the electric field polarization is perpendicular to the common axis (alpha=0 degree). Figure 2.20 shows that the peaks of the extinction, scattering and absorption cross-section spectra all increase with the shrink of the distance d and the peak positions are red shifted accordingly.

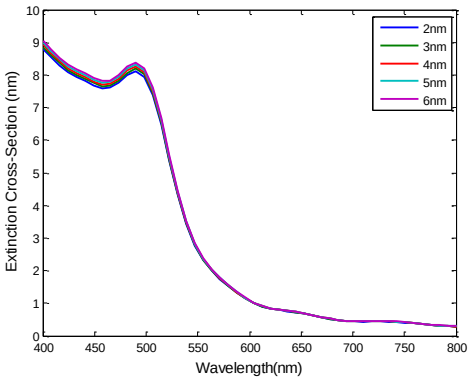

(a)

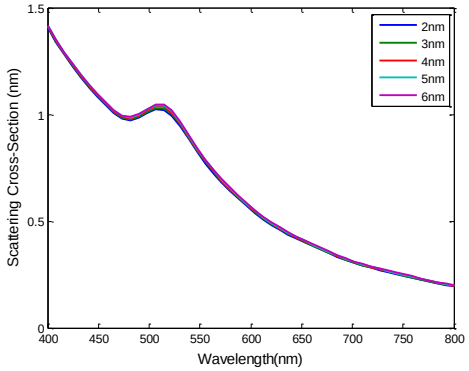

(b)

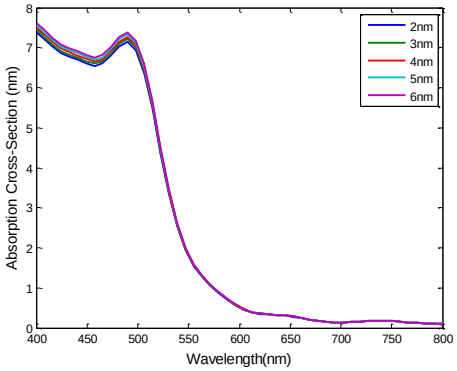

(c)

Figure 2.19 (a) Extinction, (b) scattering and (c) absorption cross-section spectra of a nano-ellipse dimer with different values of distance between its two nano-ellipses. The angle alpha of the incident wave is 0 degree.

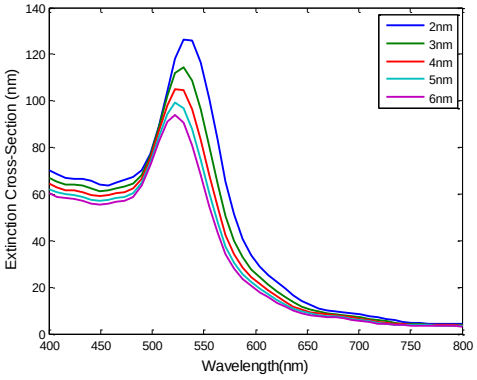

(a)

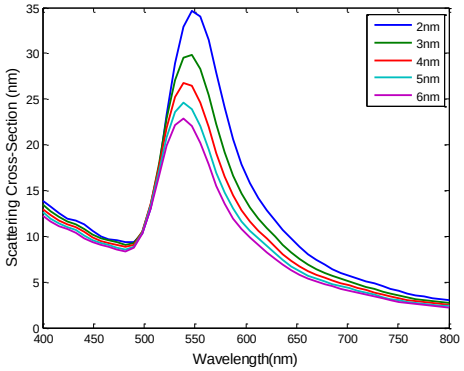

(b)

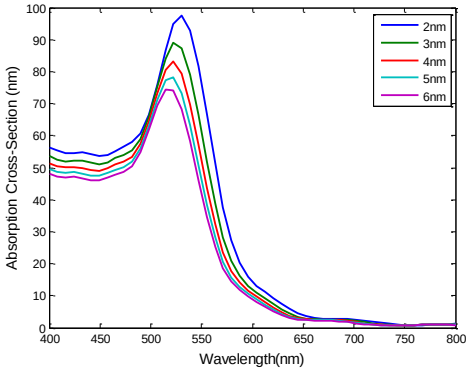

(c)

Figure 2.20 (a) Extinction, (b) scattering and (c) absorption cross-section spectra of a nano-ellipse dimer with different values of distance between its two nano-ellipses. The angle alpha of the incident wave is 90 degrees.

In the third case, the length of the align radius r2 of the two nano-ellipses changes from 10nm to 30nm. The other radius r1 keeps 10nm. The distance d is 2nm. The dimer is surrounded by air and the incident wave is propagating along the direction perpendicular to the common axis (alpha=90 degree). The extinction, scattering and absorption cross-section spectra are depicted in Figure 2.21 (a), (b) and (c), respectively. It shows as the radius r2 increasing, the cross-sections are dramatically enhanced and the plasmonic resonance frequency is red shifted.

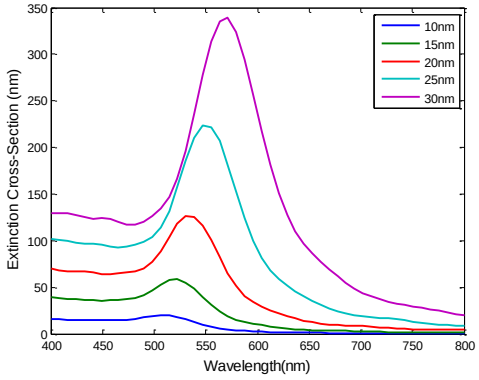

(a)

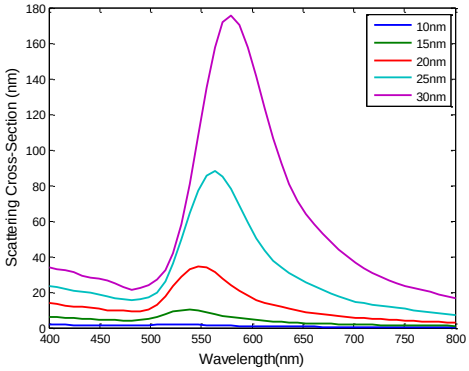

(b)

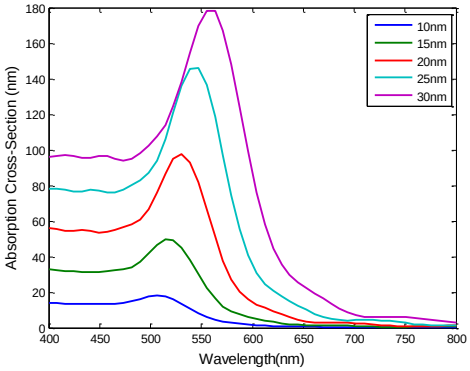

(c)

Figure 2.21 (a) Extinction, (b) scattering and (c) absorption cross-section spectra of a nano-ellipse dimer with different length of radius r2. The angle alpha of the incident wave is 90 degrees.

in the fourth case, the background refractive index of the dimer is changed to 1.00, 1.33, 1.42, 1.49 and 3.20 corresponding the materials air, water, silica, Polymethyl Methacrylate and silicon, respectively. The distance d is 2nm and the length of the radius r1 and r2 is 10nm and 20nm, respectively. The incident angle alpha=90 degrees. Figure 2.22 shows that with the increase of the background index, the peak of extinction cross-section spectrum increases and the peak position moves from the visible lightwave range to the infrared range.

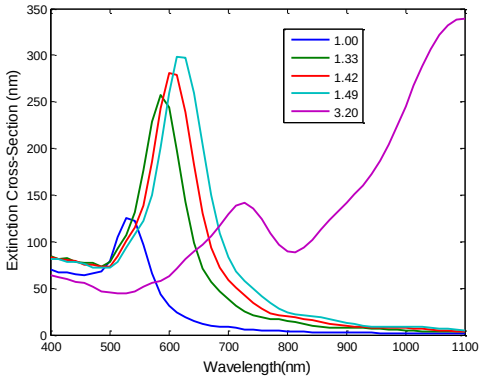

(a)

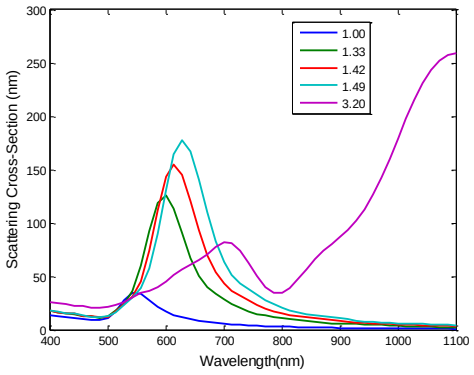

(b)

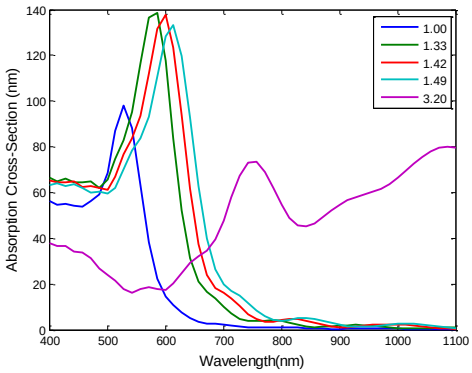

(c)

Figure 2.22 (a) Extinction, (b) scattering and (c) absorption cross-section spectra of a nano-ellipse dimer surrounded by different background materials. The angle alpha of the incident wave is 90 degrees.

2.6.5 Simulation of Nano-ellipse Trimer

The structure of a gold nano-ellipse trimer is shown in Figure 2.23. The trimer consists of three identical nano-ellipses with a longer radius r2 and a shorter radius r1. The three nano-ellipses are evenly distributed in a plane and their axes along the longer radius r2 have a common point of intersection. The distances from the three nano-ellipses to the common point of intersection are all equal to d. The incident plane wave propagates toward the trimer with an angle of alpha to the axis along the radius r2 of one nano-ellipse.

The optical properties of the nano-ellipse trimer are studied using the 2D FDTD method with TM polarization.

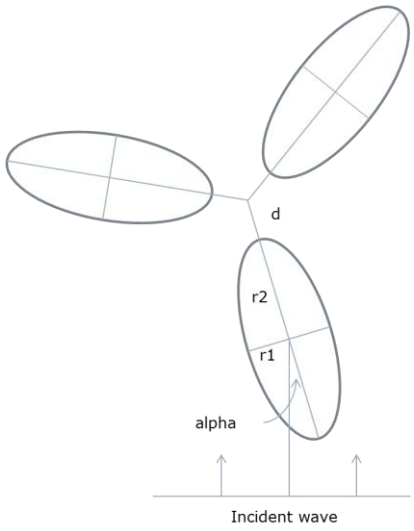

Figure 2.23 Structure of a nano-ellipse trimer.

The extinction, scattering and absorption cross-sections spectra of the trimer are studied in four cases where the incident wave angle, the value of d, the length of the radius r2 and the refractive index of the background material is changed, respectively. In the first case, the propagating angle of the incident wave is changed from 0 degree to 60 degrees. The trimer is surrounded by air with r1=10nm, r2=20nm and d=2nm. Figure 2.24 shows that the cross-section spectra of this trimer are very insensitive to the incident wave angle. It also means the cross-section spectra of the nano-ellipse trimer are not sensitivity to the polarization direction of electric field. This property is quite different from those of the single nano-ellipse and nano-ellipse dimer shown in Figure 2.14 and Figure 2.18, respectively, where the incident angle change influences the cross-section spectra obviously.

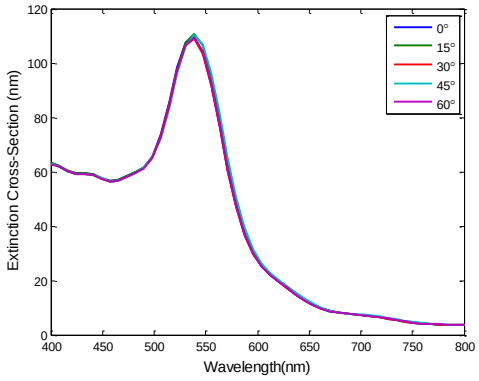

(a)

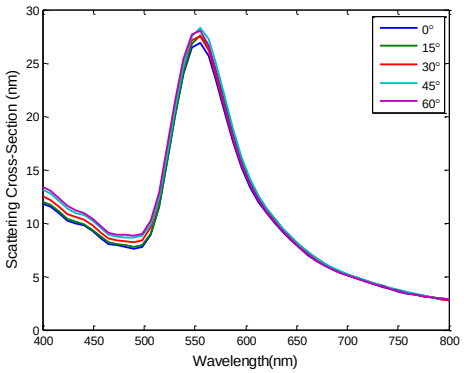

(b)

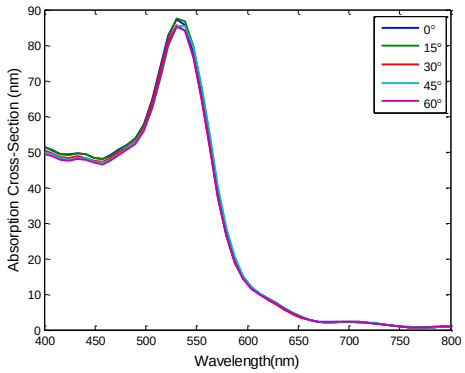

(c)

Figure 2.24 (a) Extinction, (b) scattering and (c) absorption cross-section spectra of a nano-ellipse trimer illuminated by incident wave from different angles.

In the second case, the value of d of the trimer varies from 2nm to 4nm. The trimer is surrounded by air with r1=10nm, r2=20nm. The cross-section spectra of the trimer for the incident wave angle equal to 0 degree and 60 degrees are depicted in Figure 2.25 and 2.26, respectively. There is no obvious difference between the two groups of cross-section spectra taking from two different incident angle at 0 and 60 degrees, respectively. This is consistent to the conclusion made previously in the first case. Similar to the spectra of the nano-ellipse dimer, the cross-section spectra of the nano-ellipse trimer are

enhanced with the shrink of the distance d and the peak positions are red shifted accordingly.

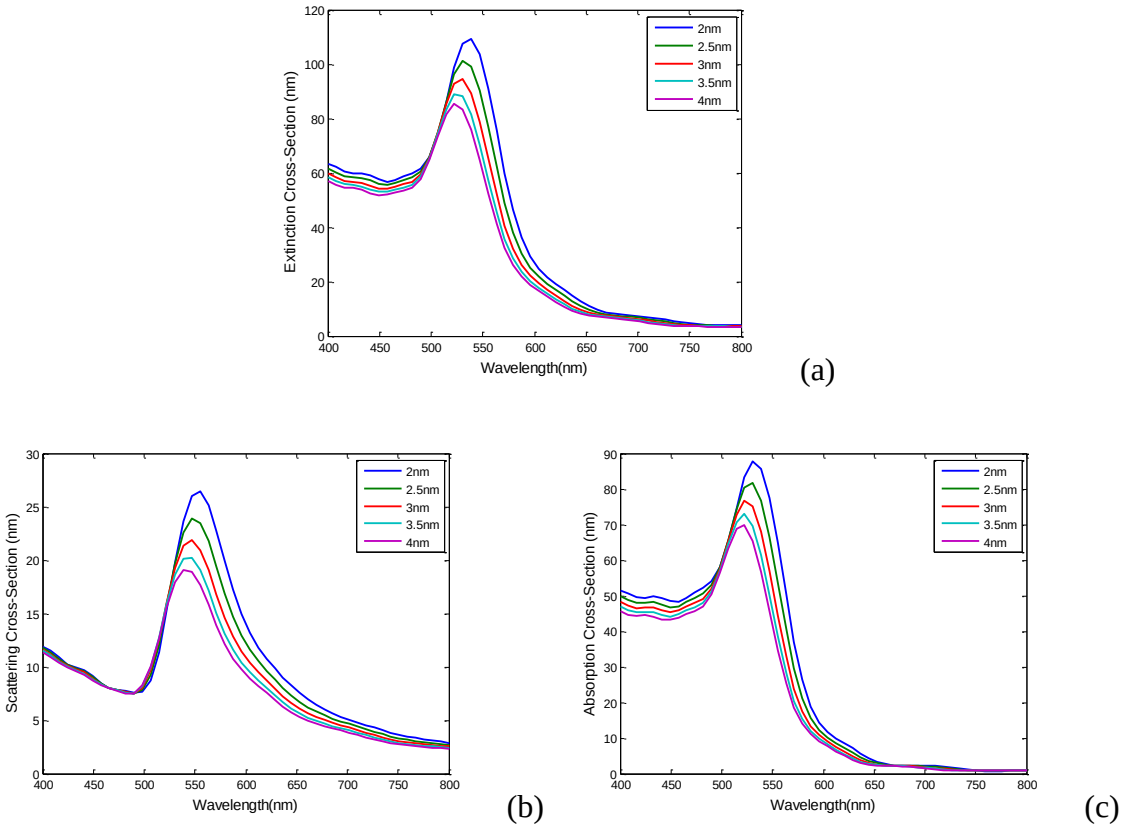

Figure 2.25 (a) Extinction, (b) scattering and (c) absorption cross-section spectra of a nano-ellipse trimer with different values of d. The angle of the incident wave is 0 degree.

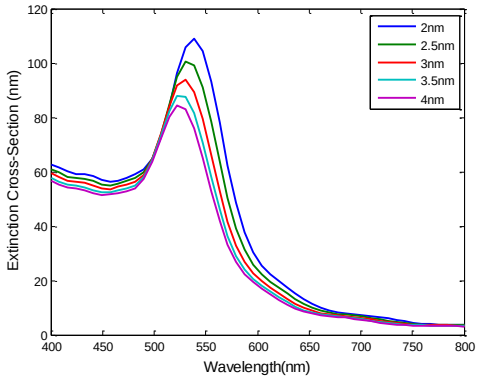

(a)

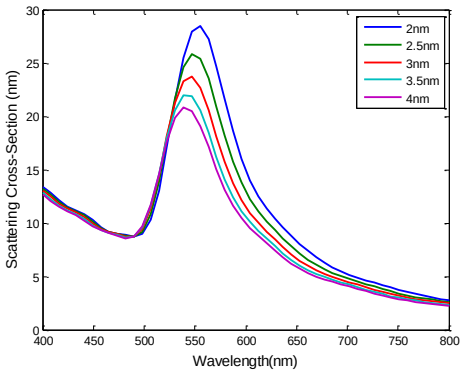

(b)

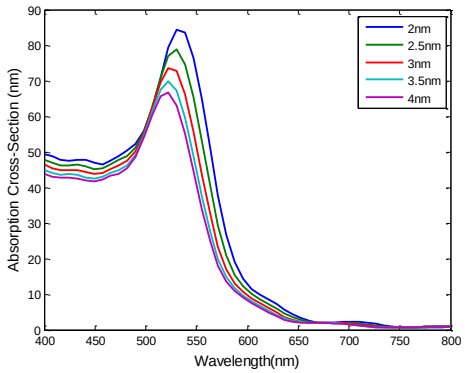

(c)

Figure 2.26 (a) Extinction, (b) scattering and (c) absorption cross-section spectra of a nano-ellipse trimer with different values of d. The angle of the incident wave is 60 degree.

In the third case, the length of the radius r2 of each nano-ellipse in the trimer is scanned simultaneously from 10nm to 30nm. The trimer is surrounded by air with radius r1=10nm and d=2nm. The incident angle alpha equals to 0 degree. Figure 2.27 gives the cross-section spectra of extinction, scattering and absorption in (a), (b) and (c), respectively. As it is expected, with the increase of the length of radius r2, the cross-section spectra are dramatically enhanced and the peak positions are red shifted.

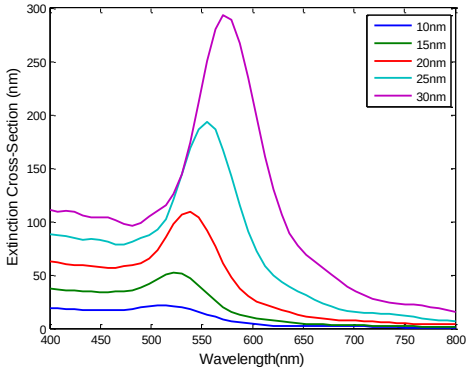

(a)

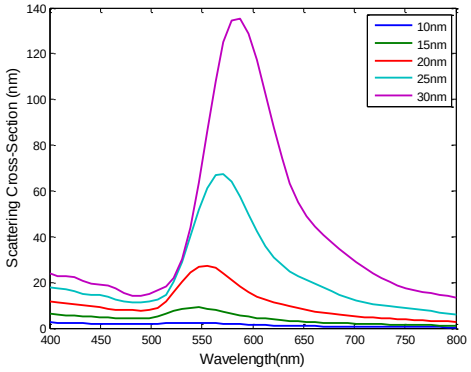

(b)

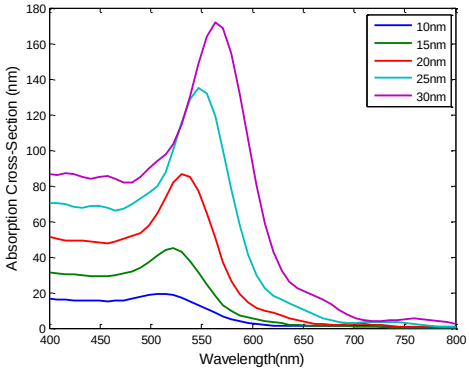

(c)

Figure 2.27 (a) Extinction, (b) scattering and (c) absorption cross-section spectra of a nano-ellipse trimer with different length of radius r2. The angle of the incident wave is 0 degree.

In the last case, the background refractive index of the trimer is changed to 1.00, 1.33, 1.42, 1.49 and 3.20 corresponding to the materials air, water, silica, Polymethyl Methacrylate and silicon, respectively. The lengths of r1 and r2 are equal to 10nm and 20nm, respectively. The distance d = 2nm and the incident angle alpha=0 degree. The cross-section spectra are given in Figure 2.28. The peak of the extinction cross-section spectrum increases along with the increase of the background refractive index and the

peak position is red shifted accordingly. This trend is the same as it is observed for the nano-ellipse dimer.

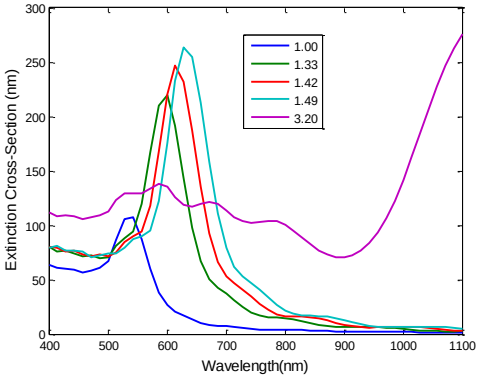

(a)

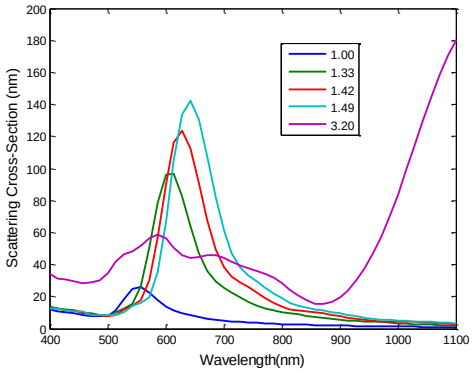

(b)

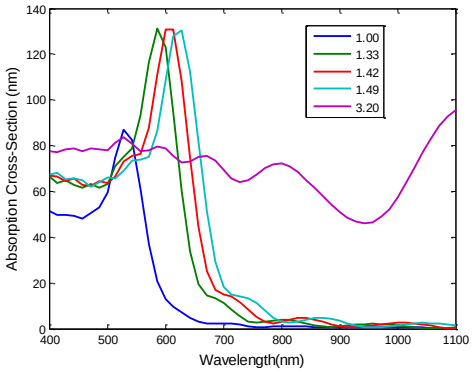

(c)

Figure 2.28 (a) Extinction, (b) scattering and (c) absorption cross-section spectra of a nano-ellipse trimer surrounded by different materials. The angle of the incident wave is 0 degree.

2.6.6 Summary of Optical Properties

The optical properties of a single gold nano-ellipsoid and a gold nano-ellipsoid dimer are simulated by the 3D FDTD method first. The RDM is employed for modeling the susceptibility of the dispersive material. It shows that the absorption effect of a gold single nano-ellipsoid is mainly affected by the length of the radius which is parallel to the

direction of the electric field polarization. The cross-section spectra of a dimer are affected dramatically by changing the distance between the two ellipsoids only when a significant portion of electric field is polarized along the common axis of the two particles. The resonance peaks of the cross-section spectra are shifted to the longer wavelength side when the background materials are changed to those with larger refractive index.

A single gold nano-ellipse, a gold nano-ellipse dimer and a gold nano-ellipse trimer are simulated with the 2D FDTD method with RDM for modeling the material susceptibility. The extinction, scattering and absorption cross-section spectra of them are studied in many cases where the incident wave angle, the value of d, the length of the radius r2 and the refractive index of the background material is changed, respectively. It shows that resonance peaks of the single nano-ellipse and the dimer reach the maximum when the longer axis of the nano-ellipse aligns with electric field polarization direction. However the cross-section spectra of the nano-ellipse trimer are not sensitivity to the polarization direction of electric field. The cross-section spectra of a nano-ellipse dimer are much more sensitive to the change of the distance d in the situation where the electric field polarization is parallel to the common axis than that in the situation where the electric field polarization is perpendicular to the common axis. When the background materials change to those who have larger refractive index, the resonance peaks of both the dimer and the trimer move to longer wavelength side.

2.7 Summary

The RDM with a parameter estimation method is proposed in this chapter for simulation of dispersive materials in a wide wavelength range. The new model is proven to be more efficient in terms of memory and computational costs in comparison with conventional phenomenological models. The RDM is implemented in the FDTD method, forming a powerful and efficient tool for simulating broadband optical phenomena of nano-particles with dispersive materials. This method is applied to analyze the optical properties of gold nanoparticles. The characteristics of the cross-section spectra affected by the geometry and background material of the nano-particles are carefully studies. This systematic study of the optical properties of different nano-particles gives a good reference for design of optical devices utilizing the cross-section spectra characteristics of nano-particles, such as optical sensors, optical filters, heat sinks, etc.

Chapter 3 FDTD Method for Nonlinear Materials

3.1 Introduction

It has been observed that the optical refractive indices of some optical materials, such as photonic glasses, silicon, etc., vary with the intensity of the confined optical power due to the nonlinear effect[70, 71]. This effect is attracting considerable attention due to many reasons. First of all, the nonlinear effect has great potential applications in optical devices such as power stabilizers, all optical switches, second-harmonic generators, etc. [72, 73] Secondly, the nonlinear effects are not negligible in the design of many optical devices whose optical density is high. For example, the optical devices manufactured with Silicon-On-Insulator (SOI) technology are now intensively studied because of their low cost potential[74]. In these devices, light is strongly confined in the Si core region because the Si (index=3.4) is surrounded by the silicon oxide (index=1.42) and air (index=1.0) forming a high-index-contrast waveguide. The high optical intensity of the strongly confined light in the waveguide enhances the nonlinear effects of the Si material[74]. It is necessary to take into consideration of the nonlinear effects in the simulation of such devices[75]. Otherwise, the performances of the designed device will be difficult to be predicted.

In poled glasses, the second-order nonlinearity is observed. This material is very useful in design of second-harmonic generators[70]. In silicon material, the nonlinear effects result from the third-order susceptibility[76]. These effects include Raman nonlinearity, Kerr

effect, etc. Without loss of generality, both the second-order and third-order nonlinearities are considered in the FDTD method[77, 78].

Assuming the time harmonic dependence $\exp(j\omega t)$, the Maxwell's equations in frequency domain are expressed by

$$\nabla \times \tilde{\mathbf{H}} = j\omega\tilde{\mathbf{D}} + \sigma\tilde{\mathbf{E}} \tag{3.1}$$

$$\nabla \times \tilde{\mathbf{E}} = -j\omega\mu_0\tilde{\mathbf{H}} \tag{3.2}$$

where $\tilde{\mathbf{E}}$ and $\tilde{\mathbf{H}}$ are electric and magnetic field vector, respectively, in frequency domain; $\tilde{\mathbf{D}}$ is the frequency domain electric displacement vector; μ_0 is the permeability of the vacuum. The electric displacement vector can be expressed by a sum of several polarizations as

$$\tilde{\mathbf{D}} = \varepsilon_0\varepsilon_\infty\tilde{\mathbf{E}} + \tilde{\mathbf{P}}^L + \tilde{\mathbf{P}}_{2nd}^{NL} + \tilde{\mathbf{P}}_{3rd}^{NL} \tag{3.3}$$

where ε_0 is the permittivity in vacuum; ε_∞ is the relative permittivity; $\tilde{\mathbf{P}}^L$, $\tilde{\mathbf{P}}_{2nd}^{NL}$ and $\tilde{\mathbf{P}}_{3rd}^{NL}$ are the linear polarization, second-order and third-order nonlinear polarization, respectively. The corresponding polarization current of each polarization term is given by

$$\tilde{\mathbf{J}} = j\omega\tilde{\mathbf{P}} \tag{3.4}$$

3.2 Linear Polarization

The linear polarization term is related to the electric field through

$$\tilde{\mathbf{P}}_L = \varepsilon_0\chi_L^{(1)}\tilde{\mathbf{E}} \tag{3.5}$$

where the susceptibility can be expressed by suitable linear dispersion models such as Lorentz, Drude, and Debye models, etc. In this thesis, the Rational Dispersion Model

(RDM) is employed to model the linear susceptibility due to its high modeling efficiency, generally applicable parameter estimation, and easy implementation in time domain methods, etc. Thus, the linear susceptibility from the multi-pole RDM is given as

$$\chi_L^{(1)} = \sum_{k=1}^{P} \chi_k(\omega)$$

$$\chi_k(\omega) = \begin{cases} \dfrac{r_k}{j\omega - p_k}; if\ p_k\ is\ real \\ \dfrac{r_k}{j\omega - p_k} + \dfrac{r_k^*}{j\omega - p_k^*}; if\ p_k\ is\ \text{complex} \\ \sum\limits_{u=1}^{U} \dfrac{r_{k,u}}{(j\omega - p_k)^u}; if\ p_k\ is\ \text{a multiple root} \end{cases} \tag{3.6}$$

The polarization current $\tilde{\mathbf{J}}_k^L$ related to each term in the summation of the linear susceptibility is given by

$$\tilde{\mathbf{J}}_k^L = j\omega\varepsilon_0\tilde{\mathbf{E}} \begin{cases} \dfrac{r_k}{j\omega - p_k}; if\ p_k\ is\ real \\ \dfrac{r_k}{j\omega - p_k} + \dfrac{r_k^*}{j\omega - p_k^*}; if\ p_k\ is\ \text{complex} \end{cases} \tag{3.7}$$

As described in chapter 2, the polarization current is transformed in to time domain and then discretized explicitly in both time and space as

$$\mathbf{J}_k^L\,|^{n+1/2} = k_k \mathbf{J}_k^L\,|^{n-1/2} + \beta_k \left(\frac{\mathbf{E}\,|^{n+1/2} - \mathbf{E}\,|^{n-1/2}}{\Delta t} \right) \tag{3.8}$$

where

$$k_k = \frac{2 + p_k \Delta t}{2 - p_k \Delta t}; \beta_k = \frac{2 r_k \varepsilon_0 \Delta t}{2 - p_k \Delta t}$$

$$C_a = \frac{2\varepsilon_0 \varepsilon_\infty - \sigma \Delta t + \mathrm{Re} \sum_{k=1}^{P} (m \beta_k)}{2\varepsilon_0 \varepsilon_\infty + \sigma \Delta t + \mathrm{Re} \sum_{k=1}^{P} (m \beta_k)}; C_b = \frac{2\Delta t}{2\varepsilon_0 \varepsilon_\infty + \sigma \Delta t + \mathrm{Re} \sum_{k=1}^{P} (m \beta_k)} \tag{3.9}$$

$$m = \begin{cases} 1; & \text{if } p_k \text{ is real} \\ 2; & \text{if } p_k \text{ is complex} \end{cases}$$

3.3 Second-order Nonlinear Polarization

The linear polarization term is related to the electric field by

$$\tilde{\mathbf{P}}_{2nd}^{NL} = \varepsilon_0 \chi_{NL}^{(2)} \tilde{\mathbf{E}} \tilde{\mathbf{E}} \tag{3.10}$$

where $\chi_{NL}^{(2)}$ is the susceptibility corresponding to the second-order nonlinear effect. Thus in time domain, the corresponding second-order nonlinear polarization current is given by

$$\mathbf{J}_{2nd}^{NL} = \varepsilon_0 \chi_{NL}^2 \frac{\partial}{\partial t} \mathbf{E}^2 \tag{3.11}$$

The finite difference discretization is applied, and yields

$$\mathbf{J}_{2nd}^{NL} \Big|^{n+1/2} = -\mathbf{J}_{2nd}^{NL} \Big|^{n-1/2} + 2\varepsilon_0 \chi_{NL}^{(2)} \frac{\left(\mathbf{E} \Big|^{n+1/2}\right)^2 - \left(\mathbf{E} \Big|^{n-1/2}\right)^2}{\Delta t} \tag{3.12}$$

Consequently, the n-th step update equation is given by

$$\mathbf{J}_{2nd}^{NL} \Big|^{n} = \frac{\mathbf{J}_{2nd}^{NL} \Big|^{n+1/2} + \mathbf{J}_{2nd}^{NL} \Big|^{n-1/2}}{2} = \varepsilon_0 \chi_{NL}^{(2)} \frac{\left(\mathbf{E} \Big|^{n+1/2}\right)^2 - \left(\mathbf{E} \Big|^{n-1/2}\right)^2}{\Delta t} \tag{3.13}$$

3.4 Third-order Nonlinear Polarization

The third order nonlinear polarization is given by the time convolution between the third-order susceptibility function $\chi_{NL}^{(3)}(t_1,t_2,t_3)$ and the electric field for the different time scales t_1, t_2 and t_3. However, for the simple model of the electron and the core of the atom, it is reduced by the Born-Oppenheimer approximation [79] to

$$\mathbf{P}_{3rd}^{NL}(t)=\varepsilon_0\chi_{NL}^{(3)}\mathbf{E}(t)\int_{-\infty}^{t}g(t-t')\mathbf{E}^2(t')dt' \tag{3.14}$$

where $\chi_{NL}^{(3)}$ is the strength of the third-order nonlinearity, and the causal response function $g(t)$ is given as in [77, 80] by

$$g(t)=\alpha\delta(t)+(1-\alpha)g_R(t) \tag{3.15}$$

Thus, under the Born-Oppenheimer approximation, the third-order polarization can be written as an expression with two terms,

$$\mathbf{P}_{3rd}^{NL}(t)=\alpha\varepsilon_0\chi_{NL}^{(3)}\mathbf{E}^3(t)+(1-\alpha)\varepsilon_0\mathbf{E}(t)\chi_{NL}^{(3)}g_R(t)*\mathbf{E}^2(t) \tag{3.16}$$

The first term represents the nonlinearity due to Kerr effect and second term represents the Raman nonlinearity. The real constant $a(0\le a\le 1)$ determines the ratio of the Kerr intensity in the total Kerr and Raman nonlinearity.

3.4.1 The Kerr Effect

The instantaneous Kerr nonlinearity, which represents the immediate response of the electrons, is expressed by the Dirac delta function $\delta(t)$ as

$$\mathbf{P}_K^{NL}(t)=\varepsilon_0\chi_{NL}^{(3)}\mathbf{E}(t)\int_{-\infty}^{t}\alpha\delta(t-t')\mathbf{E}^2(t')dt'=a\varepsilon_0\chi_{NL}^{(3)}\mathbf{E}^3(t) \tag{3.17}$$

If the time scale, over which the medium change is greater than the pulse width, the effects of the finite response time of the medium should be taken into account [81, 82]. Under this situation, the dispersive Kerr nonlinearity is given by

$$\mathbf{P}_K^{NL} = \varepsilon_0 \mathbf{S}_K \mathbf{E} \tag{3.18}$$

with $\mathbf{S}_K = \chi_{NL}^{(3)}\left(\mathbf{r}, t, |\mathbf{E}|^2\right)$ to satisfy the equation

$$\frac{\partial \mathbf{S}_K}{\partial t} + \frac{1}{\tau_K}\mathbf{S}_K = \frac{1}{\tau_K}\varepsilon_K |\mathbf{E}|^2 \tag{3.19}$$

where τ_K is the medium response time and ε_K is the Kerr model permittivity.

In this chapter, only the instantaneous Kerr nonlinearity is implemented in the FDTD method. In time domain, the instantaneous Kerr polarization current is given by

$$\mathbf{J}_K^{NL} = \alpha\varepsilon_0\chi_{NL}^{(3)}\frac{\partial}{\partial t}\left(\mathbf{E}\right)^3 \tag{3.20}$$

Appling the finite difference discretization, it yields

$$\mathbf{J}_K^{NL}\big|^{n+1/2} = -\mathbf{J}_K^{NL}\big|^{n-1/2} + 2\alpha\varepsilon_0\chi_{NL}^{(3)}\frac{\left(\mathbf{E}\big|^{n+1/2}\right)^3 - \left(\mathbf{E}\big|^{n-1/2}\right)^3}{\Delta t} \tag{3.21}$$

By taking the average of the values from the adjacent steps, the n-th step update equation is obtained as

$$\mathbf{J}_K^{NL}\big|^{n} = \frac{\mathbf{J}_K^{NL}\big|^{n+1/2} + \mathbf{J}_K^{NL}\big|^{n-1/2}}{2} = \alpha\varepsilon_0\chi_{NL}^{(3)}\frac{\left(\mathbf{E}\big|^{n+1/2}\right)^3 - \left(\mathbf{E}\big|^{n-1/2}\right)^3}{\Delta t} \tag{3.22}$$

3.4.2 The Raman Effect

The polarization caused by the Raman effect is descried under the Born-Oppenheimer approximation by [77, 79]

$$\mathbf{P}_R^{NL}(t) = (1-\alpha)\varepsilon_0 \mathbf{E}(t)\chi_{NL}^{(3)} g_R(t) * \mathbf{E}^2(t) \tag{3.23}$$

where the Raman nonlinear kernel function $g_R(t)$ is given by

$$g_R(t) = \frac{\tau_1^2 + \tau_2^2}{\tau_1 \tau_2^2} \exp\left(-\frac{t}{\tau_2}\right) \sin\left(\frac{t}{\tau_1}\right) u(t) \tag{3.24}$$

Thus, the Raman effect, which is a retarded response of the nuclei of atoms, is approximated by the response function of damped oscillation having a characteristic frequency $\frac{1}{\tau_1}$ and the damping time constant τ_2. In frequency domain, the Raman kernel function is expressed by

$$\tilde{g}_R = \frac{\omega_R^2}{\omega_R^2 + 2j\omega\delta_R - \omega^2} \tag{3.25}$$

where

$$\omega_R^2 = \frac{\tau_1^2 + \tau_2^2}{\tau_1 \tau_2^2}; \delta_R = \frac{1}{\tau_2} \tag{3.26}$$

To simplify the Raman nonlinearity express, a new definition is introduced as

$$\mathbf{S}_R = (1-\alpha)\chi_{NL}^{(3)} g_R(t) * \mathbf{E}^2 \tag{3.27}$$

By converting the above equation into frequency domain, the convolution is convert in to a product given by

$$\tilde{\mathbf{S}}_R = (1-\alpha)\chi_{NL}^{(3)} \tilde{g}_R \tilde{\mathbf{E}}^2 \tag{3.28}$$

By substituting equation (3.25) into the above equation, one obtains

$$\tilde{\mathbf{S}}_R = \frac{A\omega_R^2}{\omega_R^2 + 2j\omega\delta_R - \omega^2} \tilde{\mathbf{E}}^2 \tag{3.29}$$

with $A=(1-\alpha)\chi_{NL}^{(3)}$.

By taking the inverse Fourier transform on equation(3.29), a time domain differential equation is obtained as

$$\frac{\partial^2 \mathbf{S}_R}{\partial t^2}+2\delta_R\frac{\partial \mathbf{S}_R}{\partial t}+\omega_R^2\mathbf{S}_R=A\omega_R^2\mathbf{E}^2 \tag{3.30}$$

Applying the finite difference discretization centered at time step n+1/2 on the above equation, one obtains

$$\mathbf{S}_R\,|^{n+1/2}=-\left[\frac{1-\Delta t\delta_R}{1+\Delta t\delta_R}\right]\mathbf{S}_R\,|^{n-3/2}+\left[\frac{2-\omega_R^2\Delta t^2}{1+\Delta t\delta_R}\right]\mathbf{S}_R\,|^{n-1/2}+\left[\frac{A\omega_R^2(\Delta t)^2}{1+\Delta t\delta_R}\right]\left(\mathbf{E}\,|^{n-1/2}\right)^2 \tag{3.31}$$

In time domain, the Raman polarization current is given by

$$\mathbf{J}_R^{NL}=\varepsilon_0\frac{\partial}{\partial t}\mathbf{S}_R\mathbf{E} \tag{3.32}$$

By discretizing the above equation, yields

$$\mathbf{J}_R^{NL}\,|^{n+1/2}=-\mathbf{J}_R^{NL}\,|^{n-1/2}+\frac{2\varepsilon_0}{\Delta t}\left(\mathbf{E}\,|^{n+1/2}\,\mathbf{S}_R\,|^{n+1/2}-\mathbf{E}\,|^{n-1/2}\,\mathbf{S}_R\,|^{n-1/2}\right) \tag{3.33}$$

The n-th step update equation is obtained by taking the average of the values from the adjacent steps, as

$$\mathbf{J}_R^{NL}\,|^{n}=\frac{\mathbf{J}_R^{NL}\,|^{n+1/2}+\mathbf{J}_R^{NL}\,|^{n-1/2}}{2}=\frac{\varepsilon_0}{\Delta t}\left(\mathbf{E}\,|^{n+1/2}\,\mathbf{S}_R\,|^{n+1/2}-\mathbf{E}\,|^{n-1/2}\,\mathbf{S}_R\,|^{n-1/2}\right) \tag{3.34}$$

3.5 Electric Field Updating Scheme

By substitute the displacement vector expression (3.3) into equation (3.1), the frequency domain magnetic field curl equation is obtained as

$$\nabla \times \tilde{\mathbf{H}} = \sigma \tilde{\mathbf{E}} + j\omega\left(\varepsilon_0 \varepsilon_\infty \tilde{\mathbf{E}} + \tilde{\mathbf{P}}^L + \tilde{\mathbf{P}}_{2nd}^{NL} + \tilde{\mathbf{P}}_{3rd}^{NL}\right) \tag{3.35}$$

where $\tilde{\mathbf{P}}_{3rd}^{NL} = \tilde{\mathbf{P}}_K^{NL} + \tilde{\mathbf{P}}_R^{NL}$.

Substituting the polarizations with the corresponding polarization currents, the above equation can be rewritten as

$$\nabla \times \tilde{\mathbf{H}} = \sigma \tilde{\mathbf{E}} + j\omega\varepsilon_0 \varepsilon_\infty \tilde{\mathbf{E}} + \sum_{k=1}^{P} \tilde{\mathbf{J}}_k^L + \tilde{\mathbf{J}}_{2nd}^{NL} + \tilde{\mathbf{J}}_{3rd}^{NL} \tag{3.36}$$

where $\tilde{\mathbf{J}}_{3rd}^{NL} = \tilde{\mathbf{J}}_K^{NL} + \tilde{\mathbf{J}}_R^{NL}$

Taking the inverse Fourier transform on the above equation, the time domain curl equation is obtained as

$$\left(\nabla \times \mathbf{H}\right) = \sigma \mathbf{E} + \varepsilon_0 \varepsilon_\infty \frac{\partial}{\partial t} \mathbf{E} + \sum_{k=1}^{P} \mathbf{J}_k^L + \mathbf{J}_{2nd}^{NL} + \mathbf{J}_K^{NL} + \mathbf{J}_R^{NL} \tag{3.37}$$

Discretizing the electric and magnetic fields and substituting (3.22), (3.13), (3.22) and (3.34) into the above equation, yields the finite difference equation

$$\begin{aligned}
\left(\nabla \times \mathbf{H}\right)^n &= \varepsilon_0 \varepsilon_\infty \frac{\mathbf{E}^{n+1/2} - \mathbf{E}^{n-1/2}}{\Delta t} + \sigma \frac{\mathbf{E}^{n+1/2} + \mathbf{E}^{n-1/2}}{2} \\
&+ \sum \frac{1}{2}\left(1 + k_p\right) \mathbf{J}_{RDM}^{n-1/2} + \sum \frac{\beta_p}{2\Delta t}\left(\mathbf{E}^{n+1/2} - \mathbf{E}^{n-1/2}\right) \\
&+ \frac{\varepsilon_0 \chi^{(2)}}{\Delta t}\left[\left(\mathbf{E}^{n+1/2}\right)^2 - \left(\mathbf{E}^{n-1/2}\right)^2\right] \\
&+ \frac{\alpha \varepsilon_0 \chi_0^{(3)}}{\Delta t}\left[\left(\mathbf{E}^{n+1/2}\right)^3 - \left(\mathbf{E}^{n-1/2}\right)^3\right] \\
&+ \frac{\varepsilon_0}{\Delta t}\left(\mathbf{E}^{n+1/2}\mathbf{S}_R^{n+1/2} - \mathbf{E}^{n-1/2}\mathbf{S}_R^{n-1/2}\right)
\end{aligned} \tag{3.38}$$

Rearranging the above equation, one gets

$$
\begin{aligned}
&\left(\nabla\times\mathbf{H}\right)^{n} = \\
&+\left(\frac{\varepsilon_0\varepsilon_\infty}{\Delta t}+\frac{\sigma}{2}+\sum\frac{\beta_p}{2\Delta t}+\frac{\varepsilon_0\chi^{(2)}}{\Delta t}\mathbf{E}^{n+1/2}+\frac{\alpha\varepsilon_0\chi_0^{(3)}}{\Delta t}\left(\mathbf{E}^{n+1/2}\right)^2+\frac{\varepsilon_0}{\Delta t}\mathbf{S}_R^{n+1/2}\right)\mathbf{E}^{n+1/2} \\
&-\left(\frac{\varepsilon_0\varepsilon_\infty}{\Delta t}-\frac{\sigma}{2}+\sum\frac{\beta_p}{2\Delta t}+\frac{\varepsilon_0\chi^{(2)}}{\Delta t}\mathbf{E}^{n-1/2}+\frac{\alpha\varepsilon_0\chi_0^{(3)}}{\Delta t}\left(\mathbf{E}^{n-1/2}\right)^2+\frac{\varepsilon_0}{\Delta t}\mathbf{S}_R^{n-1/2}\right)\mathbf{E}^{n-1/2} \\
&+\sum\frac{1}{2}\left(1+k_p\right)\mathbf{J}_{RDM}^{n-1/2}
\end{aligned}
\tag{3.39}
$$

By solving the above equation, $\mathbf{E}^{n+1}$ is obtained as

$$
\mathbf{E}^{n+1/2}=C_a\mathbf{E}^{n-1/2}+C_b\left(\nabla\times\mathbf{H}^{n}-\mathrm{Re}\left(\sum\frac{1}{2}\left(1+k_p\right)\mathbf{J}_{RDM}^{n-1/2}\right)\right) \tag{3.40}
$$

Where

$$
\begin{aligned}
C_a &= \frac{\left(2\varepsilon_0\varepsilon_\infty-\sigma\Delta t+\mathrm{Re}\left(\sum\beta_p\right)+2\varepsilon_0\chi^{(2)}\mathbf{E}^{n-1/2}+2\alpha\varepsilon_0\chi_0^{(3)}\left(\mathbf{E}^{n-1/2}\right)^2+2\varepsilon_0\mathbf{S}_R^{n-1/2}\right)}{\left(2\varepsilon_0\varepsilon_\infty+\sigma\Delta t+\mathrm{Re}\left(\sum\beta_p\right)+2\varepsilon_0\chi^{(2)}\mathbf{E}^{n+1/2}+2\alpha\varepsilon_0\chi_0^{(3)}\left(\mathbf{E}^{n+1/2}\right)^2+2\varepsilon_0\mathbf{S}_R^{n+1/2}\right)} \\
C_b &= \frac{2\Delta t}{\left(2\varepsilon_0\varepsilon_\infty+\sigma\Delta t+\mathrm{Re}\left(\sum\beta_p\right)+2\varepsilon_0\chi^{(2)}\mathbf{E}^{n+1/2}+2\alpha\varepsilon_0\chi_0^{(3)}\left(\mathbf{E}^{n+1/2}\right)^2+2\varepsilon_0\mathbf{S}_R^{n+1/2}\right)}
\end{aligned}
\tag{3.41}
$$

Since $\mathbf{E}^{n+1/2}$ appears on both sides of the equation, Newton iteration is employed to update E field.

3.6 Magnetic Field Updating Scheme

The time domain electric field curl equation can be obtained by taking inverse Fourier transform on equation (3.2), as

$$
\nabla\times\mathbf{E}=-\mu_0\frac{\partial}{\partial t}\mathbf{H} \tag{3.42}
$$

The finite difference equation for updating the magnetic field at n+1 time step can be easily obtained by discretizing the above equation:

$$\mathbf{H}^{n+1} = D_a \mathbf{H}^n - D_b \left(\nabla \times \mathbf{E}^{n+1/2} \right) \tag{3.43}$$

with

$$D_a = 1, D_b = \frac{\Delta t}{\mu_0} \tag{3.44}$$

3.7 Summary of the FDTD Updating Scheme

In the FDTD simulation, the electric field, magnetic fields and all the related variables at all special locations are updated step by step. At each time step, the updating scheme follows the sequence of

1. Update E

$$\mathbf{E}^{n+1/2} = C_a \mathbf{E}^{n-1/2} + C_b \left(\nabla \times \mathbf{H}^n - \mathrm{Re}\left(\sum \frac{1}{2} \left(1 + k_p \right) \mathbf{J}_{RDM}^{n-1/2} \right) \right)$$

Where

$$C_a = \frac{\left(2\varepsilon_0 \varepsilon_\infty - \sigma \Delta t + \mathrm{Re}\left(\sum \beta_p \right) + 2\varepsilon_0 \chi^{(2)} \mathbf{E}^{n-1/2} + 2\alpha \varepsilon_0 \chi_0^{(3)} \left(\mathbf{E}^{n-1/2} \right)^2 + 2\varepsilon_0 \mathbf{S}_R^{n-1/2} \right)}{\left(2\varepsilon_0 \varepsilon_\infty + \sigma \Delta t + \mathrm{Re}\left(\sum \beta_p \right) + 2\varepsilon_0 \chi^{(2)} \mathbf{E}^{n+1/2} + 2\alpha \varepsilon_0 \chi_0^{(3)} \left(\mathbf{E}^{n+1/2} \right)^2 + 2\varepsilon_0 \mathbf{S}_R^{n+1/2} \right)}$$

$$C_b = \frac{2\Delta t}{\left(2\varepsilon_0 \varepsilon_\infty + \sigma \Delta t + \mathrm{Re}\left(\sum \beta_p \right) + 2\varepsilon_0 \chi^{(2)} \mathbf{E}^{n+1/2} + 2\alpha \varepsilon_0 \chi_0^{(3)} \left(\mathbf{E}^{n+1/2} \right)^2 + 2\varepsilon_0 \mathbf{S}_R^{n+1/2} \right)}$$

Since $\mathbf{E}^{n+1/2}$ appears on both sides of the equation, Newton iteration is employed to update E field.

2. Update Linear polarization current

$$\mathbf{J}_{RDM}^{n+1/2} = k_p \mathbf{J}_{RDM}^{n-1/2} + \beta_p \left(\frac{\mathbf{E}^{n+1/2} - \mathbf{E}^{n-1/2}}{\Delta t} \right)$$

3. Update Raman polarization current

$$\mathbf{S}_R^{n+1/2} = -\left[\frac{1-\Delta t \delta_R}{1+\Delta t \delta_R} \right] \mathbf{S}_R^{n-3/2} + \left[\frac{2-\omega_R^2 \Delta t^2}{1+\Delta t \delta_R} \right] \mathbf{S}_R^{n-1/2} + \left[\frac{A \omega_R^2 (\Delta t)^2}{1+\Delta t \delta_R} \right] \left(\mathbf{E}^{n-1/2} \right)^2$$

$$\mathbf{J}_R^{n+1/2} = -\mathbf{J}_R^{n-1/2} + \frac{2\varepsilon_0}{\Delta t} \left(\mathbf{E}^{n+1/2} \mathbf{S}_R^{n+1/2} - \mathbf{E}^{n-1/2} \mathbf{S}_R^{n-1/2} \right)$$

4. Update H

$$\mathbf{H}^{n+1} = D_a \mathbf{H}^n - D_b \left(\nabla \times \mathbf{E}^{n+1/2} \right)$$

3.8 Simulation of 1D-temporal Soliton

As we know than when a lightwave pulse propagating in a linear dispersive media, the pulse will be broadened due to the chromatic dispersion of the media[83]. Figure 3.1 shows the waveform of a pulse with carrier frequency $f_c = 1.37 \times 10^{14} Hz$ and a hyperbolic-secant function envelope with characteristic time constant $T = 14.6 fs$. The pulse width $T_0 = 8T$ is about 7 cycles of the carrier in the pulse.

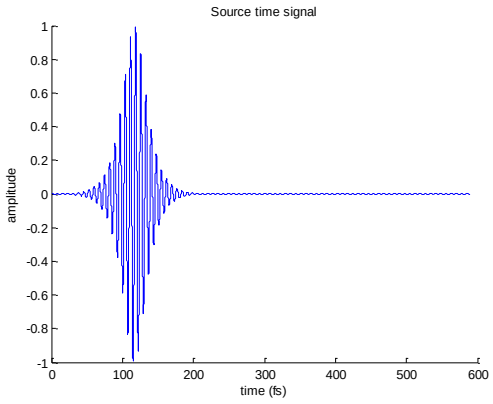

Figure 3.1 The time domain waveform of a pulse with hyperbolic-secant function envelop

The pulse is launched and propagating in a linear dispersive media with RDM parameters $\varepsilon_\infty = 2.52$, $p = -10^{11} - 4\times10^{14} i$ and $r = 5.46\times10^{14} i$. Figure 3.2 depicts the FDTD simulation results of the special waveforms of this pulse after it has propagated $55\mu m$ (blue line) and $126\mu m$ (red line), respectively. It shows clearly that the pulse is broadened in the media.

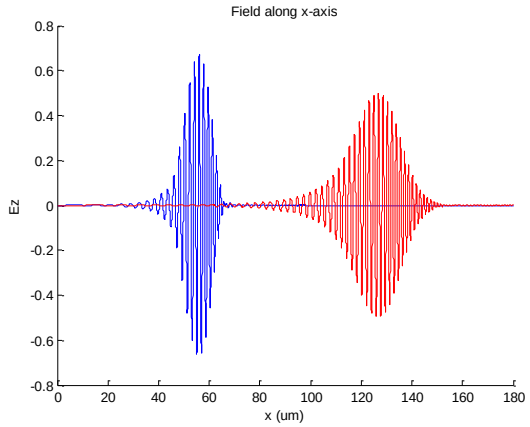

Figure 3.2 FDTD results of a pulse propagating in a linear dispersive media: the blue line is the spatial waveform after it has propagated $55\mu m$, the red line is the spacial waveform after it has propagated $126\mu m$

The same pulse is launched in a nonlinear media with the same parameters for the RDM polarization and nonlinear parameters $\alpha = 0.7$, $\chi_{NL}^{(3)} = 7\times10^{-2} m/V$, $\tau_1 = 12.2\, fs$ and $\tau_2 = 32\, fs$. Figure 3.3 gives the FDTD results of the soliton propagating in this nonlinear media. It shows that the soliton is not broadened when it propagates from the position of $55\mu m$ to $126\mu m$. From the frequency domain spectrum depicted in Figure 3.4, it can be

observed that the frequency spectrum is shifted to the lower side (red shift) when the soliton propagating in this nonlinear media.

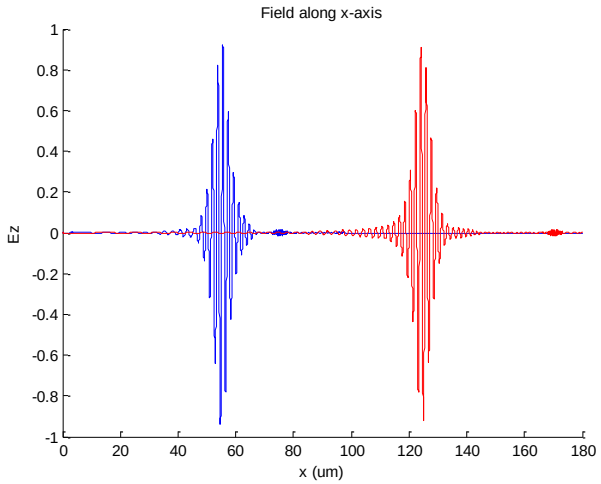

Figure 3.3 FDTD results of a pulse propagating in a nonlinear dispersive media: the blue line is the spacial waveform after it has propagated $55\mu m$, the red line is the spacial waveform after it has propagated $126\mu m$

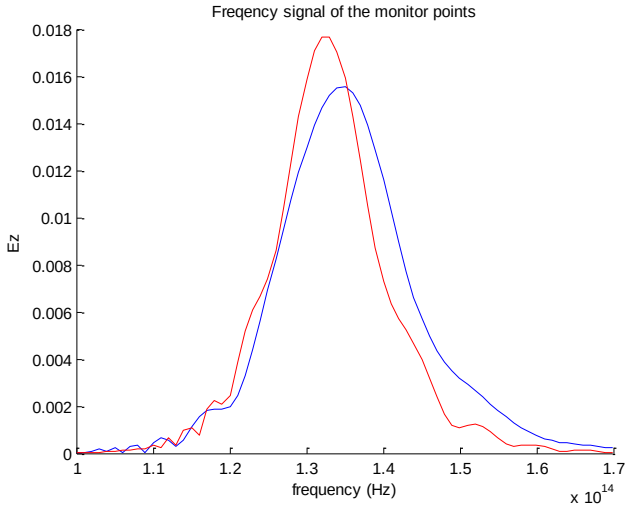

Figure 3.4 Frequency spectrum of the main propagating soliton at spacial position x=$55\mu m$ (blue line) and x=$126\mu m$ (red line).

3.9 Summary

In this chapter, the second-order nonlinearity and the third-order nonlinearity including Raman effect and Kerr effect are studied and implemented in the FDTD method. The RDM proposed in last chapter is integrated in the nonlinear FDTD scheme to handle the linear dispersion aspect. The implemented FDTD method is verified by simulating a 1D-temporal soliton. It forms a useful tool for simulating of optical devices consisting of nonlinear materials such as poled glasses with the second-order nonlinearity and silicon materials with nonlinear effects resulting from the third-order susceptibility.

Chapter 4 FDTD Method for Gain Materials

4.1 Introduction

Semiconductor optical sources and amplifiers such as semiconductor lasers, light emitting diodes (LED), silicon optical amplifiers (SOA), etc. are key components in lightwave communication system. These devices consist of a variety of different semiconductor materials such as indium phosphide (InP), gallium Indium arsenide phosphide (GaInAsP), gallium arsenide (GaAs), indium gallium arsenide (InGaAs), aluminium Gallium Arsenide (AlGaAs), etc. In this chapter, we focus on modeling the semiconductor lasers with gain materials. Several models have been proposed for modeling of different types of semiconductor lasers in different levels of complexity and accuracy. The physics-based models[84-86] are used to describe physical mechanisms of the semiconductor laser in terms of optical resonance, gain profile, refractive index derivation, carrier transport, heat dissipation, etc. However, the full physics-based models are very complicated and power consuming in numerical simulations. The behavior models such as zero[87-89] and one[90-92] dimensional rate equation models are widely adopted for modeling of Fabry-Perot (FP) and distributed feedback (DFB) lasers in system simulation due to the simplicity and efficiency. However, in the behavior modes, the optical filed is usually over simplified based on the characteristics of the cavity geometry of a specific type of laser. It cannot be employed to model lasers with arbitrary cavity geometries. In 1996, Hagness proposed a Lorentz shape gain model for the FDTD method to simulate devices with gain materials[93]. In 1998, Nagra and York adopted

Hagness's gain model with the FDTD method and added the rate equation model for the carriers to simulate semiconductor lasers with arbitrary cavity geometries[94]. Later, this method was improved with a more accurate multi-pole Lorentz gain model[95]. In the chapter, we propose a more efficient gain model for modeling of the gain materials with the FDTD method, as well as a new method to discretize the carrier rate equation.

4.2 Optical Model for Gain Materials

In this section, the RDM with multiple poles are proposed for modeling of the gain materials in the FDTD method. The Maxwell's curl equations are given by

$$\begin{aligned} \nabla \times \mathbf{H} &= \varepsilon \frac{\partial \mathbf{E}}{\partial t} + \mathbf{J}_t \\ \nabla \times \mathbf{E} &= -\mu_0 \frac{\partial \mathbf{H}}{\partial t} \end{aligned} \tag{4.1}$$

where $\mathbf{E}$ and $\mathbf{H}$ are electric and magnetic field vector, respectively, in time domain; $\mathbf{J}_t$ is the current density; μ_0 is the permeability of the vacuum. The material gain in the Maxwell's curl equations is introduced though the concept of the frequency-dependent conductivity given by $\mathbf{H}$

$$\sigma(\omega) = \frac{\tilde{\mathbf{J}}_t(\omega)}{\tilde{\mathbf{E}}(\omega)} = \left(\frac{1}{1 + I / I_s} \right) \sum_{k=1}^{P} R_k \tag{4.2}$$

where $\tilde{\mathbf{E}}$ and $\tilde{\mathbf{J}}_t$ are frequency domain electric field and current density vector, respectively. R_k is one of the RDM terms given by

$$R_k = \begin{cases} \dfrac{r_k}{j\omega - p_k}; if\ p_k\ is\ real \\ \dfrac{r_k}{j\omega - p_k} + \dfrac{r_k^*}{j\omega - p_k^*}; if\ p_k\ is\ \text{complex} \end{cases} \tag{4.3}$$

The parameters r_k and p_k are functions of carrier density N, which can be estimated by fitting the gain curves under different currents. Each of the RDM terms is linked to the corresponding current density by the expression

$$\tilde{\mathbf{J}}_k = \frac{R_k}{1+I/I_s}\tilde{\mathbf{E}} \tag{4.4}$$

where I is the optical intensity, which is given by $I=(1/2)cn\varepsilon_0 E^2$, I_s is the saturation optical intensity. By substituting the RDM expression into the above equation, the current density is obtained as

$$\tilde{\mathbf{J}}_k = s\tilde{\mathbf{E}}\begin{cases}\dfrac{r_k}{j\omega-p_k}; if\ \ p_k\ \ is\ real\\ \dfrac{r_k}{j\omega-p_k}+\dfrac{r_k^*}{j\omega-p_k^*}; if\ \ p_k\ \ is\ \text{complex}\end{cases} \tag{4.5}$$

with $s=\dfrac{1}{1+I/I_s}$. The total current density is the summation of all the current density, given as

$$\tilde{\mathbf{J}}_t = \sum_{k=1}^{P}\tilde{\mathbf{J}}_k \tag{4.6}$$

By taking the inverse Fourier transform on the equation of current density, the time domain current density corresponding to each of the RDM terms can be obtained. If p_k is real, r_k is also real, then the time-domain current density is real and given by

$$\frac{\partial \mathbf{J}_k}{\partial t} - p_k\mathbf{J}_k = r_k s\mathbf{E} \tag{4.7}$$

If p_k is complex, r_k is also complex. The time-domain current density has two parts $\mathbf{J}_k$ and $\mathbf{J}'_k$, corresponding to the two complex poles in equation (4.5). The two polarization currents are all complex and given by

$$\frac{\partial \mathbf{J}_k}{\partial t} - p_k \mathbf{J}_k = r_k s\mathbf{E} \tag{4.8}$$

$$\frac{\partial \mathbf{J}'_k}{\partial t} - p_k^* \mathbf{J}'_k = r_p^* s\mathbf{E} \tag{4.9}$$

Because $\mathbf{E}(t)$ is real, if the initial values for the two polarization current are the same, the two parts are mutual complex conjugate, i.e. $\mathbf{J}'_k = \mathbf{J}_k^*$. Only one complex equation, either equation (4.8) or (4.9), needs to be computed in the FDTD calculation. In the following derivation, equation (4.8) is employed. Therefore, when p_k is complex, the real part of the time domain current density is $\mathrm{Re}\left[\mathcal{F}^{-1}\left(\tilde{\mathbf{J}}_k\right)\right] = 2\,\mathrm{Re}\left(\mathbf{J}_k\right)$. The time domain Ampere's curl equation is given by

$$\varepsilon \frac{\partial}{\partial t}\mathbf{E} + \sum_{k=1}^{P} m\,\mathrm{Re}\left(\mathbf{J}_k\right) = \nabla \times \mathbf{H} \tag{4.10}$$

where $m = 1$ if p_k is real; $m = 2$ if p_k is complex. The time domain current density equation and Ampere's curl equation are combined together and discretized in the explicit FDTD scheme, yielding

$$\mathbf{E}\,|^{n+1/2} = C_a \mathbf{E}\,|^{n-1/2} + C_b \left[\nabla \times \mathbf{H}\,|^n - \mathrm{Re}\left(\sum_{k=1}^{L} \frac{m}{2}\left(1 + k_p\right)\mathbf{J}_k\,|^{n-1/2}\right)\right] \tag{4.11}$$

$$\mathbf{J}_k\,|^{n+1/2} = k_k \mathbf{J}_k\,|^{n-1/2} + \beta_k \left(\frac{\mathbf{E}\,|^{n+1/2} + \mathbf{E}\,|^{n-1/2}}{2}\right) \tag{4.12}$$

where

$$k_k = \frac{2 + p_k \Delta t}{2 - p_k \Delta t}; \beta_k = \frac{2 r_k s \Delta t}{2 - p_k \Delta t}$$

$$C_a = \frac{2\varepsilon + \mathrm{Re}\sum_{k=1}^{L}\left(m\beta_k\right)}{2\varepsilon + \mathrm{Re}\sum_{k=1}^{L}\left(m\beta_k\right)}; C_b = \frac{2\Delta t}{2\varepsilon + \mathrm{Re}\sum_{k=1}^{L}\left(m\beta_k\right)} \tag{4.13}$$

$$m = \begin{cases} 1; & \textit{if } p_k \textit{ is real} \\ 2; & \textit{if } p_k \textit{ is complex} \end{cases}$$

The carrier rate equation for a two energy level atomic system is expressed by

$$\frac{dN}{dt} = \frac{2}{\hbar\omega_0} E J_t - \frac{N}{\tau_c} + D\nabla^2 N + W_p$$

$$W_p = \frac{I}{qV} \tag{4.14}$$

$$\frac{N}{\tau_c} = AN + BN^2 + CN^3$$

where A, B, and C are the coefficients related with surface recombination, spontaneous emission, and Auger recombination, respectively.

The electric field with frequency ω is given by

$$\mathbf{E} = \mathbf{E}_0 e^{-\alpha\cdot\mathbf{r}} e^{j(\omega t - \beta\cdot\mathbf{r})} \tag{4.15}$$

For a low gain material, the optical gain is expressed by

$$gain(\omega) = -\alpha(\omega) \cong -\frac{\mathrm{Re}\left[\sigma(\omega)\right]}{2c\varepsilon_0 n_{neff}} \tag{4.16}$$

It shows clearly that if the real part of the conductivity is negative, we get a gain material. Otherwise, we get a lossy material. The conductivity is given by

$$\sigma(\omega)=\left(\frac{1}{1+I/I_s}\right)\sum_{k=1}^{P}R_k \approx \sum_{k=1}^{P}R_k ;(I<<I_s) \tag{4.17}$$

Thus, the real part of the conductivity can be calculated from the summation of the real parts of RDM terms by

$$\mathrm{Re}\left[\sigma(\omega)\right]=\sum_{k=1}^{P}\mathrm{Re}(R_k) \tag{4.18}$$

Similarly, the imaginary part of the conductivity is given by

$$\mathrm{Im}\left[\sigma(\omega)\right]=\sum_{k=1}^{P}\mathrm{Im}(R_k) \tag{4.19}$$

It reflects a change in the material refractive index caused by a change in carrier density. The real part of each RDM term is given by

$$\mathrm{Re}(R_k)=\begin{cases}\mathrm{Re}\left(\dfrac{r_k}{j\omega-p_k}\right);\textit{if } p_k \textit{ is real}\\ \mathrm{Re}\left(\dfrac{r_k}{j\omega-p_k}+\dfrac{r_k^*}{j\omega-p_k^*}\right);\textit{if } p_k \textit{ is} \text{ complex}\end{cases} \tag{4.20}$$

or

$$\mathrm{Re}(R_k)=\begin{cases}\dfrac{-r_k p_k}{\omega^2+p_k^2};\textit{if } p_k \textit{ is real}\\ \dfrac{\left[\left(-r_k p_k^*-r_k^* p_k\right)\left(p_k p_k^*-\omega^2\right)-\left(r_k+r_k^*\right)\left(p_k+p_k^*\right)\right]\omega^2}{\left(p_k p_k^*-\omega^2\right)^2+\left(\left(p_k+p_k^*\right)\omega\right)^2};\textit{if } p_k \textit{ is} \text{ complex}\end{cases}$$

(4.21)

And the imaginary part of the RDM term is given by

$$\mathrm{Im}(R_k)=\begin{cases}\dfrac{-r_k\omega}{\omega^2+p_k^2}; if\ \ p_k\ \ is\ real\\ \dfrac{\left[\left(r_k+r_k^*\right)\left(p_k p_k^*-\omega^2\right)+\left(-r_k p_k^*-r_k^* p_k\right)\left(p_k+p_k^*\right)\right]\omega}{\left(p_k p_k^*-\omega^2\right)^2+\left(\left(p_k+p_k^*\right)\omega\right)^2}; if\ \ p_k\ \ is\ \text{complex}\end{cases}$$

(4.22)

The theoretical gain profiles of a bulk material for different carrier densities are plotted in Figure 4.1. A two poles RDM model is employed to fit the theoretical gain profiles. It shows that the fit results agree very well with the theoretical results in the specified energy range. If it is required to fit the gain profiles in a wide energy range, more RDM poles can be added to obtain accurate results.

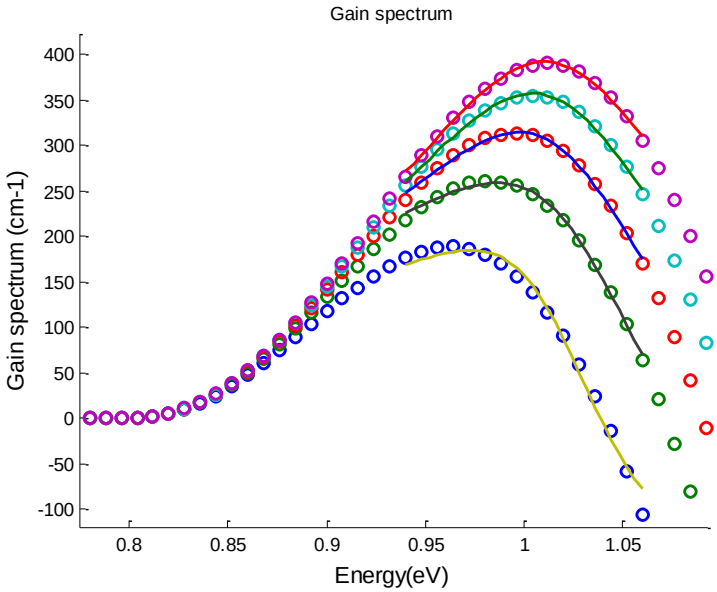

Figure 4.1 Gain profiles for different carrier densities: the dots are data calculated from theoretical gain model, the solid lines are fitted results through 2 RDM poles by using the RDM model.

The mirror loss of this laser diode is given by

$$\alpha_{mirror} = \frac{1}{2L}\ln\left(\frac{1}{R_1 R_2}\right) \tag{4.23}$$

where R1, R2 are the reflectivity of the mirrors on two sides of the longitudinal direction, and are given by

$$R = \frac{Z_2 - Z_1}{Z_2 + Z_1} = \frac{\sqrt{\varepsilon_{r1}} - \sqrt{\varepsilon_{r2}}}{\sqrt{\varepsilon_{r1}} + \sqrt{\varepsilon_{r2}}} = \frac{n_1 - n_2}{n_1 + n_2} \tag{4.24}$$

where n1, n2 are the material indices on two sides of a mirror.

The cavity modes of a Fabry-Perot laser is expressed by

$$\lambda_m = \frac{2nL}{m} \tag{4.25}$$

where m is the mode index.

The mode spacing of two adjacent modes is approximated by

$$\Delta\lambda = \frac{\lambda_p{}^2}{2nL} \tag{4.26}$$

where λ_p is the wavelength at the gain peak.

The finite difference equations of the optical equations are summarized as follows.

$$\begin{aligned}
\mathbf{E}\big|^{n+1/2} &= C_a \mathbf{E}\big|^{n-1/2} + C_b\left[\nabla\times\mathbf{H}\big|^{n} - \mathrm{Re}\left(\sum_{k=1}^{L}\frac{m}{2}\left(1+k_p\right)\mathbf{J}_k\big|^{n-1/2}\right)\right] \\
\mathbf{J}_k\big|^{n+1/2} &= k_k \mathbf{J}_k\big|^{n-1/2} + \beta_k\left(\frac{\mathbf{E}\big|^{n+1/2} + \mathbf{E}\big|^{n-1/2}}{2}\right) \\
\mathbf{H}^{n+1} &= \mathbf{H}^{n} - \frac{\Delta t}{\mu_0}\left(\nabla\times\mathbf{E}^{n+1/2}\right)
\end{aligned} \tag{4.27}$$

where

$$
\begin{aligned}
&k_k = \frac{2 + p_k \Delta t}{2 - p_k \Delta t}; \beta_k = \frac{2 r_k s \Delta t}{2 - p_k \Delta t} \\
&C_a = \frac{2\varepsilon + \mathrm{Re}\sum_{k=1}^{L}\left(m\beta_k\right)}{2\varepsilon + \mathrm{Re}\sum_{k=1}^{L}\left(m\beta_k\right)}; C_b = \frac{2\Delta t}{2\varepsilon + \mathrm{Re}\sum_{k=1}^{L}\left(m\beta_k\right)} \\
&m = \begin{cases} 1; & \textit{if } p_k \textit{ is real} \\ 2; & \textit{if } p_k \textit{ is} \text{ complex} \end{cases} \\
&s(i) = \frac{1}{1 + I(i)/I}, I(i) = \frac{1}{2} c \varepsilon_0 \sqrt{\varepsilon_r} \left[E_x^{peak}(i) \right]^2
\end{aligned}
\tag{4.28}
$$

4.3 Rate Equation Model for Carriers

If we do not consider the carrier diffusion process, the carrier equation is obtained as

$$
\frac{dN}{dt} = \frac{2}{\hbar \omega_0} E J_t - \frac{N}{\tau_c} + W_p \tag{4.29}
$$

It is discretized as follows for spatial one dimensional structure

$$
\begin{aligned}
&\frac{N|_i^{n+1} - N|_i^n}{\Delta t} = \frac{2}{\hbar \omega_0} E_x|_i^{n+1/2} \; J_t|_i^{n+1/2} - \frac{N|_i^{n+1} + N|_i^n}{2\tau_c} + W_p \\
&\left(\frac{1}{\Delta t} + \frac{1}{2\tau_c}\right) N|_i^{n+1} = \left(\frac{1}{\Delta t} - \frac{1}{2\tau_c}\right) N|_i^n + \frac{2}{\hbar \omega_0} E_x|_i^{n+1/2} \; J_t|_i^{n+1/2} + W_p \\
&N|_i^{n+1} = \frac{2\tau_c - \Delta t}{2\tau_c + \Delta t} N|_i^n + \frac{2\tau_c \Delta t}{2\tau_c + \Delta t} \left(\frac{2}{\hbar \omega_0} E_x|_i^{n+1/2} \; J_t|_i^{n+1/2} + W_p \right)
\end{aligned}
\tag{4.30}
$$

In order to avoid the spatial hole burning, the carrier diffusion process needs to be taken in to account. The carrier rate equation is then expressed by

$$
\frac{dN}{dt} = \frac{2}{\hbar \omega_0} E J_t - \frac{N}{\tau_c} + D \nabla^2 N + W_p \tag{4.31}
$$

The first discretization scheme is present in the literature [95] as follows.

The differential equation for a one dimensional structure is obtained by discretizing the carrier rate equation as

$$\frac{N|_i^{n+1} - N|_i^n}{\Delta t} = \frac{2}{\hbar\omega_0} E_x|_i^{n+1/2} \; J_t|_i^{n+1/2} - \frac{N|_i^{n+1} + N|_i^n}{2\tau_c} + D\nabla^2 \frac{N|_i^{n+1} + N|_i^n}{2} + W_p \qquad (4.32)$$

It leads to a Helmholtz-type equation as

$$\begin{gathered}
\frac{N|_i^{n+1} - N|_i^n}{\Delta t} = \frac{2}{\hbar\omega_0} E_x|_i^{n+1/2} \; J_t|_i^{n+1/2} - \frac{N|_i^{n+1} + N|_i^n}{2\tau_c} + D\nabla^2 \frac{N|_i^{n+1} + N|_i^n}{2} + W_p \\
\left(\frac{1}{\Delta t} + \frac{1}{2\tau_c} - \frac{D}{2}\nabla^2\right) N|_i^{n+1} = \left(\frac{1}{\Delta t} - \frac{1}{2\tau_c} + \frac{D}{2}\nabla^2\right) N|_i^n + \frac{2}{\hbar\omega_0} E_x|_i^{n+1/2} \; J_t|_i^{n+1/2} + W_p \\
\left(\nabla^2 - \frac{1}{D}\left(\frac{2}{\Delta t} + \frac{1}{\tau_c}\right)\right) N|_i^{n+1} = -\left(\nabla^2 + \frac{1}{D}\left(\frac{2}{\Delta t} - \frac{1}{\tau_c}\right)\right) N|_i^n + \frac{2}{\hbar\omega_0} E_x|_i^{n+1/2} \; J_t|_i^{n+1/2} + W_p
\end{gathered}$$

(4.33)

The finite difference rate equation for one dimensional case is finally obtained

$$\left(\frac{\partial^2}{\partial x^2} - \frac{1}{D}\left(\frac{2}{\Delta t} + \frac{1}{\tau_c}\right)\right) N|_i^{n+1} = -\left(\frac{\partial^2}{\partial x^2} + \frac{1}{D}\left(\frac{2}{\Delta t} - \frac{1}{\tau_c}\right)\right) N|_i^n + \frac{2}{\hbar\omega_0} E_x|_i^{n+1/2} \; J_t|_i^{n+1/2} \qquad (4.34)$$

However, it is not straightforward and obvious to find its solution. It has to be solved by using the fast Helmholtz algorithm that is described in literature [24 in Photon design's paper].

In this chapter, we propose a new way to discretize the diffusion equation as described below. For one dimensional case, the carrier rate equation is discretized as

$$\frac{N|_i^{n+1}-N|_i^n}{\Delta t}=\frac{2}{\hbar\omega_0}E_x|_i^{n+1/2}\ J_t|_i^{n+1/2}-\frac{N|_i^{n+1}+N|_i^n}{2\tau_c}+D\frac{N|_{i+1}^n-2N|_i^n+N|_{i-1}^n}{\Delta x^2}+W_p$$

$$\left(\frac{1}{\Delta t}+\frac{1}{2\tau_c}\right)N|_i^{n+1}=\left(\frac{1}{\Delta t}-\frac{1}{2\tau_c}\right)N|_i^n+\frac{2}{\hbar\omega_0}E_x|_i^{n+1/2}\ J_t|_i^{n+1/2}+W_p+D\frac{N|_{i+1}^n-2N|_i^n+N|_{i-1}^n}{\Delta x^2}$$

$$N|_i^{n+1}=\frac{2\tau_c-\Delta t}{2\tau_c+\Delta t}N|_i^n+\frac{2\tau_c\Delta t}{2\tau_c+\Delta t}\left(\frac{2}{\hbar\omega_0}E_x|_i^{n+1/2}\ J_t|_i^{n+1/2}+W_p+\frac{D}{\Delta x^2}\left(N|_{i+1}^n-2N|_i^n+N|_{i-1}^n\right)\right)$$

(4.35)

Thus, the solution of the carrier density at time step n+3/2 is obtained as

$$N|_i^{n+1}=\frac{2\tau_c-\Delta t}{2\tau_c+\Delta t}N|_i^n$$
$$+\frac{2\tau_c\Delta t}{2\tau_c+\Delta t}\left(\frac{2}{\hbar\omega_0}E_x|_i^{n+1/2}\ J_t|_i^{n+1/2}+W_p+\frac{D}{\Delta x^2}\left(\frac{N|_{i+1}^{n+1}+N|_{i+1}^n}{2}-2\frac{N|_i^{n+1}+N|_i^n}{2}+\frac{N|_{i-1}^{n+1}+N|_{i-1}^n}{2}\right)\right)$$

(4.36)

It is noticed that the carrier density at the newest time step $N|^{n+1}$ appears on both side of the equation. Therefore, Newton iterations can be employed to refine the accuracy of the solution. As we know that the carrier density varies very slowly in the cavity compared with the photon density, in most cases, the solution will converge in one or two Newton iterations. This method is computational efficient.

The boundary conditions are

$$\begin{aligned}&N(t=0,x)=0\\&N(t,x=0)=N_b\\&N(t,x=end)=N_b\end{aligned}\qquad(4.37)$$

where N_b is the carrier density at two boundaries. We use a half of the average carrier density in the cavity as the value of N_b. Since carrier density varies much slower than the electric field , we only need to update N at every 100 steps (or more) of updating E-field.

4.4 FDTD Updating Scheme for Gain Material

The FDTD scheme for simulation a device with gain material includes updating the coupled equations of the optical model and electrical model. At each time step, the sequence of updating all the variables at each position along the propagating direction is as follows.

1. Update E

$$E_x\big|_i^{n+1/2} = C_a E_x\big|_i^{n-1/2} + C_b\left[\left(\frac{H_y\big|_{j+1/2}^n - H_y\big|_{j-1/2}^n}{\Delta z}\right) - \mathrm{Re}\left(\sum_{k=1}^{L}\frac{m}{2}\left(1+k_p\right)J_{kx}\big|^{n-1/2}\right)\right]$$

2. Update current density

$$J_x\big|_i^{n+1/2} = k_k J_x\big|_i^{n-1/2} + \frac{\beta_k}{2}\left[E_x\big|_i^{n+1/2} + E_x\big|_i^{n-1/2}\right]$$

3. Update magnetic field

$$H_y\big|_{j+1/2}^{n+1} = H_y\big|_{j+1/2}^{n} + \frac{\Delta t}{\mu_0 \Delta z}\left[E_x\big|_{i+1}^{n+1/2} - E_x\big|_i^{n+1/2}\right]$$

4. Update carrier density

$$N\big|_i^{n+1} = \frac{2\tau_c - \Delta t}{2\tau_c + \Delta t} N\big|_i^n + \frac{2\tau_c \Delta t}{2\tau_c + \Delta t}\left(\frac{2}{\hbar\omega_0} E_x\big|_i^{n+1/2} J_t\big|_i^{n+1/2} + W_p + \frac{D}{\Delta x^2}\left(\frac{N\big|_{i+1}^{n+1} + N\big|_{i+1}^n}{2} - 2\frac{N\big|_i^{n+1} + N\big|_i^n}{2} + \frac{N\big|_{i-1}^{n+1} + N\big|_{i-1}^n}{2}\right)\right)$$

4.5 Verification

To verify the proposed FDTD method for gain materials, a one dimensional Fabry-Perot laser diode is simulated. The parameters of a Fabry-Perot laser diode is given by

$$\begin{aligned} L &= 12.4\mu m \\ \lambda_k &= 890nm \\ n &= 3.59(GaAs) \\ I_s &= 65.2kW / cm^2 \end{aligned} \tag{4.38}$$

The index profile along the longitudinal direction is shown in Figure 4.2

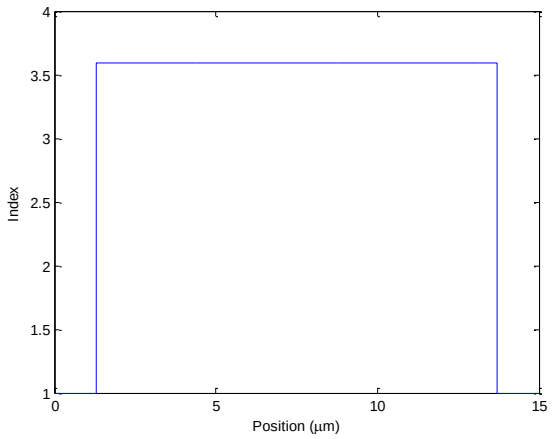

Figure 4.2 Index profile along the longitudinal direction

Figure 4.3 shows the random noise of the electric field in the laser cavity before lasing.

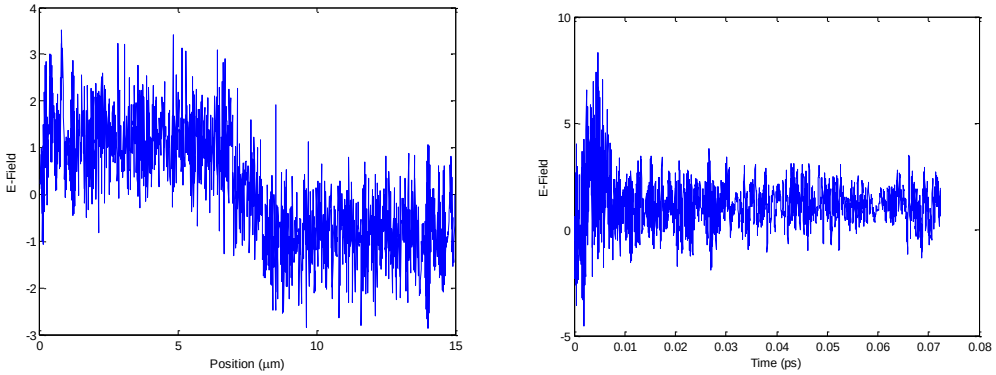

Figure 4.3 Spontaneous emission at the beginning: the first figure is the random noise at different position of the laser, the second figure is the random noise monitored at outside of the left mirror versus time.

The E-field variation during the lasing process is depicted in Figure 4.4.

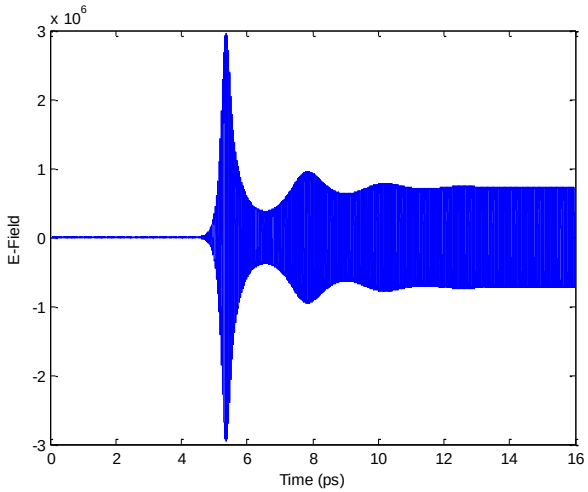

Figure 4.4 E-field evolution in the Fabry-Perot laser

The carrier density and output power from one facet are shown in Figure 4.5.

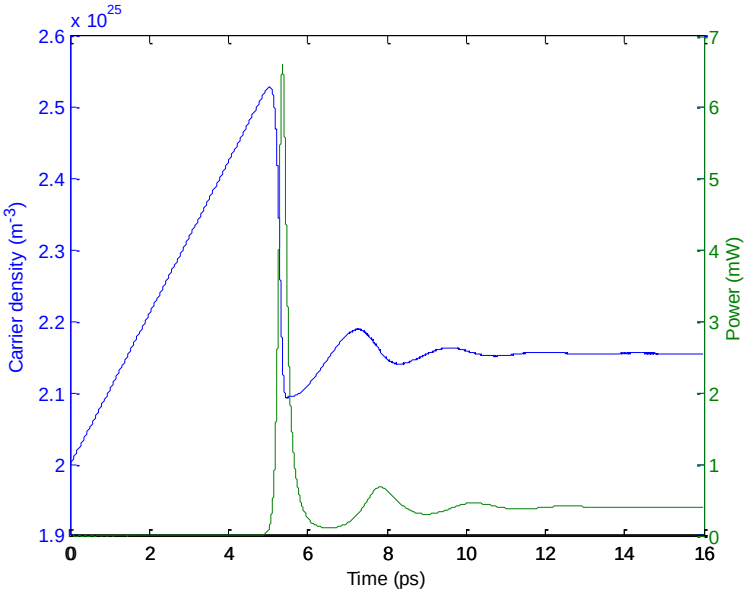

Figure 4.5 Carrier density and output power evolution

The carrier distribution in the laser cavity after lasing is depicted in Figure 4.6.

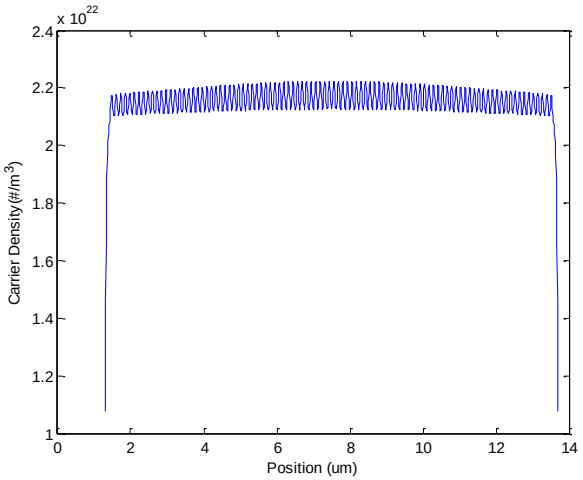

Figure 4.6 Carrier density distribution in the laser cavity after lasing

The E-field in the laser cavity after lasing at 16 picoseconds is shown in Figure 4.7.

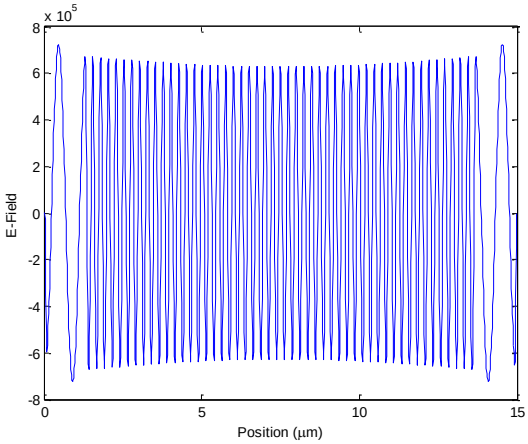

Figure 4.7 Electric field distribution in the laser cavity after lasing

The spectrum of the E-field is plotted in Figure 4.8. It shows that only one mode gets enough gain and starts lasing.

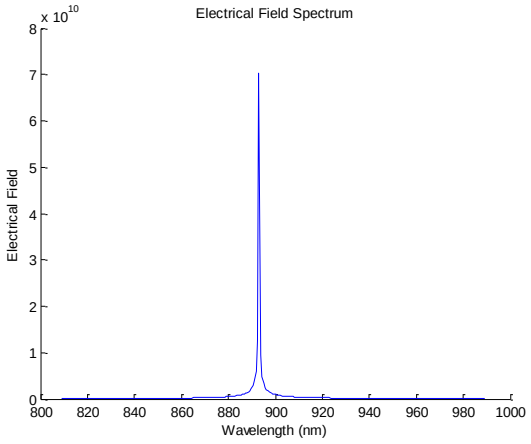

Figure 4.8 Electric field spectrum of the laser diode after lasing

If the carrier diffusion is not considered in the carrier density rate equation, the localized spatial hole burning effect appears. Figure 4.9 shows clearly that the carriers in the middle of the cavity are depleted due to the standing wave nature of the optical models. It will cause a decrease in the modal gain. Therefore the output power of the laser diode will be

affected. Figure 4.10 depicts the evolution of carrier density and output power of this laser.

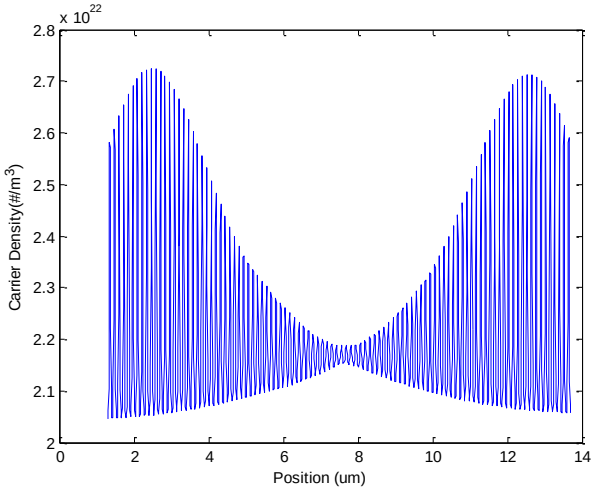

Figure 4.9 Carrier density distrubution in the laser cavity if the carrier diffusion is neglected

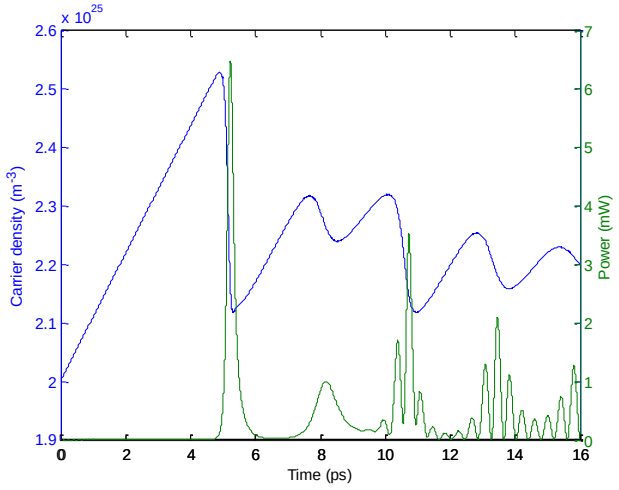

Figure 4.10 Carrier density and output power evolution if the carrier diffusion is neglected

4.6 Application

As an application of the proposed model for modeling of semiconductor lasers with arbitrary cavity geometry, it is employed to design a single mode laser based on the modification of the Fabry-Perot cavity. The cavity length of the Fabry-Perot cavity is $300\mu m$ and the refractive index is 3.59. The gain profile and the mirror loss are given in Figure 4.11. The black vertical lines indicate the scale of mode spacing compared with the scale of the gain spectrum.

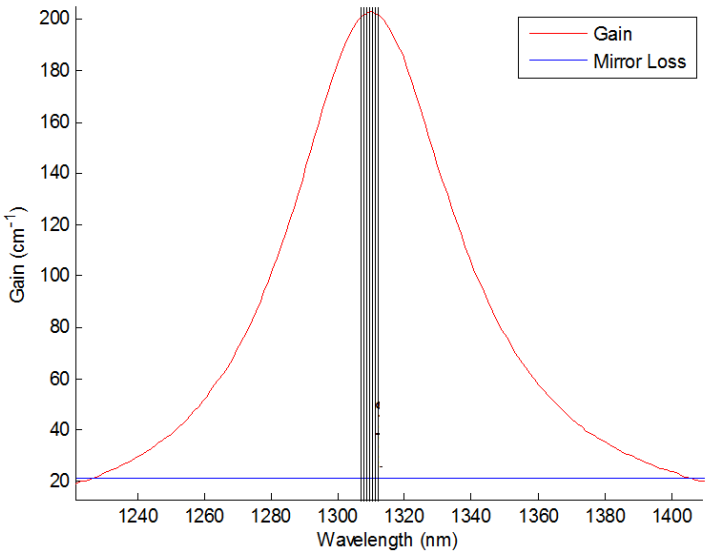

Figure 4.11 Gain and loss profile of a laser diode

Firstly, a Fabry-Perot laser with no modification on the cavity geometry is simulated. The output electric field spectrum is obtained and presented in Figure 4.12. The side-mode suppression ratio (SMSR) of this multi-mode laser is 3dB.

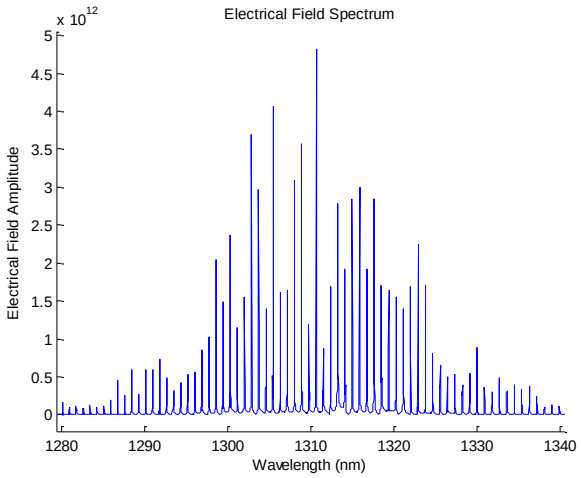

Figure 4.12 Optical spectrum of a Fabry-Perot laser diode

In order to increase the SMSR to design a single mode laser based on the Fabry-Perot cavity, two ditches are etched on the FP laser diode structure as shown in Figure 4.13. The two-ditch structure functions as a band-pass filter. The widths of the two ditches are designed to be $1\mu m$ and the spacing between them is $10\mu m$. To use this filter in the 1D laser simulation, the 3D structure is approximated to a 1D structure presented in Figure 4.14.

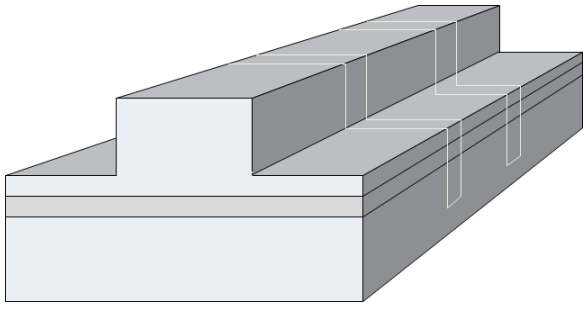

Figure 4.13 3D structure of a Fabry-Perot laser etched with two ditches

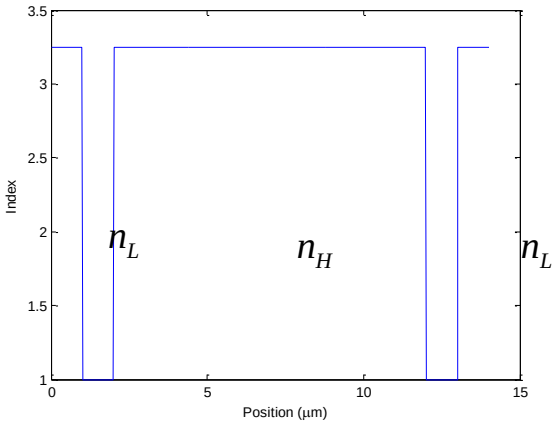

Figure 4.14 1D structure of a two-ditch band-pass filter

The power transmission and reflection spectra of the 1D band-pass filter are calculated by the FDTD method and shown in Figure 4.15.

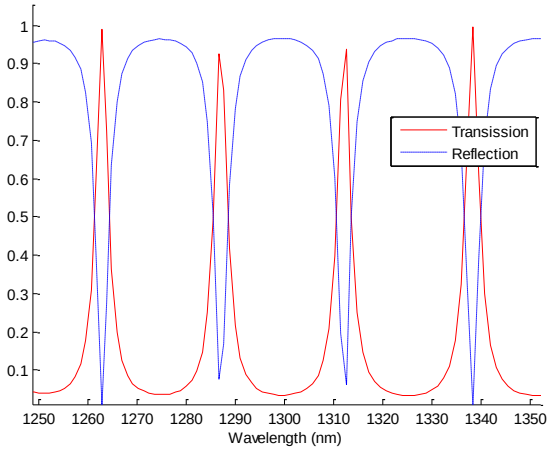

Figure 4.15 Power transmission and reflection spectra of a two-ditch band-pass filter.

The two ditches are etched on the $300\mu m$ FP cavity at the location with a distance of $75\mu m$ to the left facet. The longitudinal refractive index profile of the designed laser diode is shown in Figure 4.16.

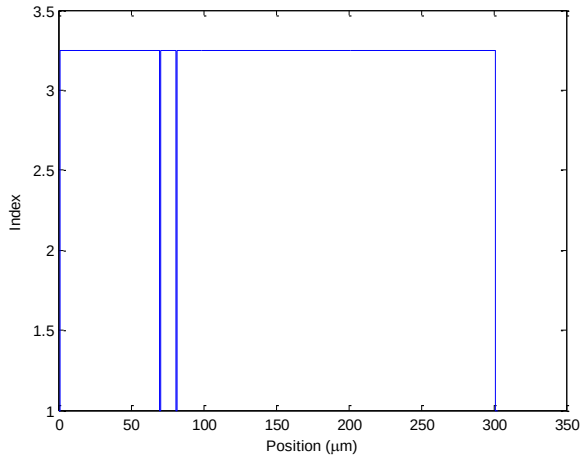

Figure 4.16 Longitudinal refractive index profile of a designed single mode laser structure

With the simulation of the designed laser diode, the spectrum of the output electric field is obtained and shown in Figure 4.17 with a SMSR of 19.8dB. It shows that by the modification of the FP cavity with two specified ditches, the SMSR is significantly improved compared with that of the original FP laser diode.

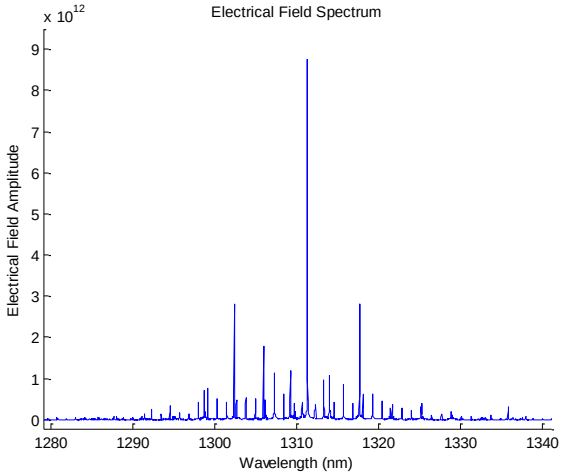

Figure 4.17 Optical spectrum of a designed laser diode

4.7 Summary

In this chapter, the FDTD method and the rate equation model are employed to simulate the semiconductor lasers with arbitrary cavity geometries. The RDM is proposed for modeling the gain materials with high efficiency and feasibility. A new method based on Newton iteration is proposed to discretize the carrier rate equation. It forms an efficient and accurate tool for simulation of semiconductor laser. To verify this method, a one dimensional Fabry-Perot laser diode is simulated and analyzed. As an application of this method, a single mode laser based on the FP cavity and a two-ditch filter is designed and optimized. It proves that this method is very useful and valuable for design of semiconductor lasers with varieties of cavity geometries.

Chapter 5 FDTD Method for Modal Analysis of Waveguides

5.1 Introduction

Mode calculation is a key task for simulation and analysis of optical waveguides and photonic integrated circuits. Several powerful numerical methods such as the finite difference (FD)[96-100] and the finite element (FE)[101, 102] methods have been developed and widely adopted for mode calculations of practical optical waveguides. In the conventional mode calculation method, the open optical waveguides are discretized over the transverse section and the boundary-value problem is reduced to a matrix eigen-value problem defined on finite computation domain facilitated by artificial numerical boundary conditions. As such, the accuracy, computational efficiency as well as memory requirements for the conventional mode solvers depend critically on size of the computation widow and number of meshes. Thanks to the powerful matrix algorithm, the solutions of the eigen-value problem associated with mode computation are normally highly efficient with an approximately linear scaling factor with total number of meshes. One of the shortcomings of the boundary-value eigen solution is that the memory requirement scales drastically with the size of the matrix and hence become a bottleneck especially for dealing with optical waveguide problem that need large number of mesh point to achieve sufficient accuracy.

An alternative approach to mode calculation is to formulate the problem as an initial-value problem. By launching an initial field at the input of the waveguide, one may track its propagation along the waveguide axis by a field propagation algorithm such as the

beam propagation method (BPM)[103-105] in frequency domain or the finite-difference time-domain (FDTD)[106, 107] method in time-domain. Once the propagation reaches its steady state, a signal processing method such as the Fourier transform (FT) method[103, 108] may be used to extract the modal parameters.

In this chapter, the optical mode solver is based on wave equation formulation in time-domain. The compact 2D-FDTD method [107] combined with matrix pencil method (MPM)[109] is adopted for calculation of the scalar, semi-vector and full-vector modes. Uniaxial perfectly matched layer (UPML)[110-112] absorbing boundary conditions (ABCs) are employed for the FDTD scheme in order to reduce the computation region. By launching an initial optical field into the waveguide, the light is propagating along the direction (z) through the FDTD method for a certain time (t). When the steady-state is reached, a series of instantaneous response field values at the end of the propagation are adopted by MPM algorithm for mode parameter extractions. Since the MPM algorithm is much more efficient and accurate for the mode parameter extraction compared with the traditional FT method, only limited propagation distance is required in FDTD simulation. Since the FDTD method is an inherently data-parallel algorithm, we implement it in Graphics Processing Units (GPUs) by using NVidia's Compute Unified Device Architecture (CUDA)[113]. With the help of the high computing power brought by GPUs[114, 115], simulation time of the FDTD method is further reduced to less than 3% of that used for the implementation on a standard 3.0GHz CPU.

This chapter is organized as follows. The wave equation-based compact 2D-FDTD method and the matrix pencil method for optical waveguide modal calculation are

described in section 2 and 3 followed by its validation in section 4. The convergence test is presented in section 5. The performance of the enhanced method implemented on GPUs using CUDA is discussed in section 6. Comparisons are made among the standard FDTD, the accelerated FDTD and the conventional eigen mode solvers.

5.2 Wave Equation-based Compact 2D-FDTD Method with UPML ABCs

For waveguide structures with uniform refractive index, derivatives of the mode field with respect to longitudinal direction can be replaced with $\mp j\beta$ and consequently reduce one dimension complexity in space which can significantly save computing time and reduce memory consumption. This method is called compact 2D-FDTD method which was introduced by Xiao et al. [107] and has been widely used in microwaves. To avoid the complex-variables in Maxwell's equation-based compact 2D-FDTD method, a wave equation-based compact 2D-FDTD method is introduced in [116].

In this section, the full-vector, semi-vector, and scalar schemes of wave equation-based compact 2D-FDTD method with UPML absorbing boundary conditions are derived in details. Compared with Benenger's PML[117], UPML is more preferable for parallel computing due to the reason that it avoids the non-physical field splitting by composing a uniaxial anisotropic medium.

5.2.1 Fullvectorial Scheme

In frequency domain, the full vector wave equation for transverse electric field in linear, isotropic medium optical waveguide is given by [118]

$$\nabla_t^2 \mathrm{E}_t + \left(n^2 - n_{eff}^2\right) k^2 \mathrm{E}_t = -\nabla_t \left(\frac{1}{n^2} \nabla_t n^2 \cdot \mathrm{E}_t\right) \tag{5.1}$$

The electric field with two perpendicular polarizations E_x, E_y obeys the following equations

$$\begin{aligned} A_{xx}E_x + A_{xy}E_y &= k^2 n_{eff}^2 E_x \\ A_{yx}E_x + A_{yy}E_y &= k^2 n_{eff}^2 E_y \end{aligned} \tag{5.2}$$

where

$$\begin{aligned} A_{xx}E_x &= \frac{\partial}{\partial x}\left[\frac{1}{n^2}\frac{\partial}{\partial x}\left(n^2 E_x\right)\right] + \frac{\partial^2 E_x}{\partial y^2} + n^2 k^2 E_x \\ A_{yy}E_y &= \frac{\partial}{\partial y}\left[\frac{1}{n^2}\frac{\partial}{\partial y}\left(n^2 E_y\right)\right] + \frac{\partial^2 E_y}{\partial x^2} + n^2 k^2 E_y \\ A_{xy}E_y &= \frac{\partial}{\partial x}\left[\frac{1}{n^2}\frac{\partial}{\partial y}\left(n^2 E_y\right)\right] - \frac{\partial^2 E_y}{\partial x \partial y} \\ A_{yx}E_x &= \frac{\partial}{\partial y}\left[\frac{1}{n^2}\frac{\partial}{\partial x}\left(n^2 E_x\right)\right] - \frac{\partial^2 E_x}{\partial y \partial x} \end{aligned} \tag{5.3}$$

Based on above equations, the full vector wave equation for the transverse electric field in time domain can be obtained as

$$\begin{aligned} \frac{n^2}{c^2}\frac{\partial^2}{\partial t^2}E_x &= \frac{\partial}{\partial x}\left[\frac{1}{n^2}\frac{\partial}{\partial x}\left(n^2 E_x\right)\right] + \frac{\partial^2 E_x}{\partial y^2} + \frac{\partial}{\partial x}\left[\frac{1}{n^2}\frac{\partial}{\partial y}\left(n^2 E_y\right)\right] - \frac{\partial^2 E_y}{\partial x \partial y} - \beta^2 E_x \\ \frac{n^2}{c^2}\frac{\partial^2}{\partial t^2}E_y &= \frac{\partial}{\partial y}\left[\frac{1}{n^2}\frac{\partial}{\partial y}\left(n^2 E_y\right)\right] + \frac{\partial^2 E_y}{\partial x^2} + \frac{\partial}{\partial y}\left[\frac{1}{n^2}\frac{\partial}{\partial x}\left(n^2 E_x\right)\right] - \frac{\partial^2 E_x}{\partial y \partial x} - \beta^2 E_y \end{aligned} \tag{5.4}$$

Since the waveguide is assumed to be homogeneous along the propagation direction (z), derivatives with respect to z have been replaced with $-j\beta$ in above equations. This replacement reduces one dimension complexity in space, which can significantly save computing time and reduce memory consumption.

By using the stretched coordinates technique[119], UPML boundary conditions can be applied to full vector compact 2D-FDTD equations as follows

$$\frac{n^2}{c^2}\frac{\partial^2}{\partial t^2}E_x = \frac{1}{s_x}\frac{\partial}{\partial x}\left[\frac{1}{n^2}\frac{1}{s_x}\frac{\partial}{\partial x}\left(n^2E_x\right)\right]+\frac{1}{s_y}\frac{\partial}{\partial y}\left[\frac{1}{s_y}\frac{\partial}{\partial y}E_x\right]-\beta^2E_x$$
$$+\frac{1}{s_x}\frac{\partial}{\partial x}\left[\frac{1}{n^2}\frac{1}{s_y}\frac{\partial}{\partial y}\left(n^2E_y\right)\right]-\frac{1}{s_y}\frac{\partial}{\partial y}\left[\frac{1}{s_x}\frac{\partial}{\partial x}E_y\right]$$
$$\frac{n^2}{c^2}\frac{\partial^2}{\partial t^2}E_y = \frac{1}{s_y}\frac{\partial}{\partial y}\left[\frac{1}{n^2}\frac{1}{s_y}\frac{\partial}{\partial y}\left(n^2E_y\right)\right]+\frac{1}{s_x}\frac{\partial}{\partial x}\left[\frac{1}{s_x}\frac{\partial}{\partial x}E_y\right]-\beta^2E_y \tag{5.5}$$
$$+\frac{1}{s_y}\frac{\partial}{\partial y}\left[\frac{1}{n^2}\frac{1}{s_x}\frac{\partial}{\partial x}\left(n^2E_x\right)\right]-\frac{1}{s_x}\frac{\partial}{\partial x}\left[\frac{1}{s_y}\frac{\partial}{\partial y}E_x\right]$$

where $s_x = 1+\sigma_x / j\omega\varepsilon_0 n^2$, $s_y = 1+\sigma_y / j\omega\varepsilon_0 n^2$

Auxiliary variables are further introduced and defined in Eq.(5.6)-(5.8)

$$j\omega D_{x\_x} = \frac{1}{s_x}\frac{\partial}{\partial x}\left(n^2E_x\right);\ j\omega D_{x\_y} = \frac{1}{s_y}\frac{\partial}{\partial y}E_x$$
$$j\omega D_{y\_x} = \frac{1}{s_x}\frac{\partial}{\partial x}E_y;\ j\omega D_{y\_y} = \frac{1}{s_y}\frac{\partial}{\partial y}\left(n^2E_y\right) \tag{5.6}$$

$$j\omega D_{x\_xx} = \frac{1}{s_x}\frac{\partial}{\partial x}\left(\frac{1}{n^2}\,j\omega D_{x\_x}\right);\ j\omega D_{x\_yy} = \frac{1}{s_y}\frac{\partial}{\partial y}\left(j\omega D_{x\_y}\right)$$
$$j\omega D_{y\_yx} = \frac{1}{s_x}\frac{\partial}{\partial x}\left(\frac{1}{n^2}\,j\omega D_{y\_y}\right);\ j\omega D_{y\_xy} = \frac{1}{s_y}\frac{\partial}{\partial y}\left(j\omega D_{y\_x}\right) \tag{5.7}$$

$$j\omega D_{y\_yy} = \frac{1}{s_y}\frac{\partial}{\partial y}\left(\frac{1}{n^2}\,j\omega D_{y\_y}\right);\ j\omega D_{y\_xx} = \frac{1}{s_x}\frac{\partial}{\partial x}\left(j\omega D_{y\_x}\right)$$
$$j\omega D_{x\_xy} = \frac{1}{s_y}\frac{\partial}{\partial y}\left(\frac{1}{n^2}\,j\omega D_{x\_x}\right);\ j\omega D_{x\_yx} = \frac{1}{s_x}\frac{\partial}{\partial x}\left(j\omega D_{x\_y}\right) \tag{5.8}$$

By substituting above auxiliary variables into Eq.(5.5), yields

$$\frac{n^2}{c^2}\frac{\partial^2}{\partial t^2}E_x = j\omega D_{x\_xx} + j\omega D_{x\_yy} - \beta^2E_x + j\omega D_{y\_yx} - j\omega D_{y\_xy}$$
$$\frac{n^2}{c^2}\frac{\partial^2}{\partial t^2}E_y = j\omega D_{y\_yy} + j\omega D_{y\_xx} - \beta^2E_y + j\omega D_{x\_xy} - j\omega D_{x\_yx} \tag{5.9}$$

By replacing $j\omega$ with $\partial/\partial t$ in the resulting equations, the time domain full vector wave equations with UPML absorbing boundary can be derived as

$$
\begin{aligned}
&\frac{n^2}{c^2}\frac{\partial^2}{\partial t^2}E_x = \frac{\partial}{\partial t}D_{x\_xx} + \frac{\partial}{\partial t}D_{x\_yy} - \beta^2 E_x + \frac{\partial}{\partial t}D_{y\_yx} - \frac{\partial}{\partial t}D_{y\_xy} \\
&\frac{n^2}{c^2}\frac{\partial^2}{\partial t^2}E_y = \frac{\partial}{\partial t}D_{y\_yy} + \frac{\partial}{\partial t}D_{y\_xx} - \beta^2 E_y + \frac{\partial}{\partial t}D_{x\_xy} - \frac{\partial}{\partial t}D_{x\_yx} \\
&\frac{\partial}{\partial t}D_{x\_x} + \frac{\sigma_x}{\varepsilon_0 n^2}D_{x\_x} = \frac{\partial}{\partial x}\left(n^2 E_x\right); \frac{\partial}{\partial t}D_{x\_y} + \frac{\sigma_y}{\varepsilon_0 n^2}D_{x\_y} = \frac{\partial}{\partial y}E_x \\
&\frac{\partial}{\partial t}D_{y\_x} + \frac{\sigma_x}{\varepsilon_0 n^2}D_{y\_x} = \frac{\partial}{\partial x}E_y; \frac{\partial}{\partial t}D_{y\_y} + \frac{\sigma_y}{\varepsilon_0 n^2}D_{y\_y} = \frac{\partial}{\partial y}\left(n^2 E_y\right) \\
&\frac{\partial}{\partial t}D_{x\_xx} + \frac{\sigma_x}{\varepsilon_0 n^2}D_{x\_xx} = \frac{\partial}{\partial x}\left(\frac{1}{n^2}\frac{\partial}{\partial t}D_{x\_x}\right); \frac{\partial}{\partial t}D_{x\_yy} + \frac{\sigma_y}{\varepsilon_0 n^2}D_{x\_yy} = \frac{\partial}{\partial y}\left(\frac{\partial}{\partial t}D_{x\_y}\right) \\
&\frac{\partial}{\partial t}D_{y\_yx} + \frac{\sigma_x}{\varepsilon_0 n^2}D_{y\_yx} = \frac{\partial}{\partial x}\left(\frac{1}{n^2}\frac{\partial}{\partial t}D_{y\_y}\right); \frac{\partial}{\partial t}D_{y\_xy} + \frac{\sigma_y}{\varepsilon_0 n^2}D_{y\_xy} = \frac{\partial}{\partial y}\left(\frac{\partial}{\partial t}D_{y\_x}\right) \\
&\frac{\partial}{\partial t}D_{y\_yy} + \frac{\sigma_y}{\varepsilon_0 n^2}D_{y\_yy} = \frac{\partial}{\partial x}\left(\frac{1}{n^2}\frac{\partial}{\partial t}D_{y\_y}\right); \frac{\partial}{\partial t}D_{y\_xx} + \frac{\sigma_x}{\varepsilon_0 n^2}D_{y\_xx} = \frac{\partial}{\partial x}\left(\frac{\partial}{\partial t}D_{y\_x}\right) \\
&\frac{\partial}{\partial t}D_{x\_xy} + \frac{\sigma_y}{\varepsilon_0 n^2}D_{x\_xy} = \frac{\partial}{\partial y}\left(\frac{1}{n^2}\frac{\partial}{\partial t}D_{x\_x}\right); \frac{\partial}{\partial t}D_{x\_yx} + \frac{\sigma_x}{\varepsilon_0 n^2}D_{x\_yx} = \frac{\partial}{\partial x}\left(\frac{\partial}{\partial t}D_{x\_y}\right)
\end{aligned}
\tag{5.10}
$$

Above equations can be discretized on Yee lattice, wherein the loss terms are averaged in time according to the semi-implicit scheme shown below

$$
\frac{\sigma_x}{\varepsilon_0 n^2}D_x = \frac{\sigma_x}{\varepsilon_0 n^2}\frac{D_x^{\,n+1} + D_x^{\,n}}{2}, \frac{\sigma_y}{\varepsilon_0 n^2}D_y = \frac{\sigma_y}{\varepsilon_0 n^2}\frac{D_y^{\,n+1} + D_y^{\,n}}{2} \tag{5.11}
$$

The FDTD scheme can then be derived as (space discretization isn't shown explicitly)

$$
\begin{aligned}
E_x^{\,n+1} &= -E_x^{\,n-1} + 2E_x^{\,n} + \frac{c^2\Delta t}{n^2}\left(D_{x\_xx}^{n} - D_{x\_xx}^{n-1}\right) + \frac{c^2\Delta t}{n^2}\left(D_{x\_yy}^{n} - D_{x\_yy}^{n-1}\right) - \frac{\beta^2 c^2 \Delta t^2}{n^2}E_x^{\,n} \\
&\quad + \frac{c^2\Delta t}{n^2}\left(D_{y\_yx}^{n} - D_{y\_yx}^{n-1}\right) - \frac{c^2\Delta t}{n^2}\left(D_{y\_xy}^{n} - D_{y\_xy}^{n-1}\right) \\
E_y^{\,n+1} &= -E_y^{\,n-1} + 2E_y^{\,n} + \frac{c^2\Delta t}{n^2}\left(D_{y\_yy}^{n} - D_{y\_yy}^{n-1}\right) + \frac{c^2\Delta t}{n^2}\left(D_{y\_xx}^{n} - D_{y\_xx}^{n-1}\right) - \frac{\beta^2 c^2 \Delta t^2}{n^2}E_y^{\,n} \\
&\quad + \frac{c^2\Delta t}{n^2}\left(D_{x\_xy}^{n} - D_{x\_xy}^{n-1}\right) - \frac{c^2\Delta t}{n^2}\left(D_{x\_yx}^{n} - D_{x\_yx}^{n-1}\right)
\end{aligned}
\tag{5.12}
$$

where

$$
\begin{aligned}
D_{x\_x}^{n+1} &= \frac{2\varepsilon_0 n^2 - \Delta t\sigma_x}{2\varepsilon_0 n^2 + \Delta t\sigma_x} D_{x\_x}^{n} + \frac{2\varepsilon_0 n^2 \Delta t}{2\varepsilon_0 n^2 + \Delta t\sigma_x}\left(\frac{\partial}{\partial x} n^2 E_x\right) \\
D_{x\_y}^{n+1} &= \frac{2\varepsilon_0 n^2 - \Delta t\sigma_y}{2\varepsilon_0 n^2 + \Delta t\sigma_y} D_{x\_y}^{n} + \frac{2\varepsilon_0 n^2 \Delta t}{2\varepsilon_0 n^2 + \Delta t\sigma_y}\left(\frac{\partial}{\partial y} E_x\right) \\
D_{y\_x}^{n+1} &= \frac{2\varepsilon_0 n^2 - \Delta t\sigma_x}{2\varepsilon_0 n^2 + \Delta t\sigma_x} D_{y\_x}^{n} + \frac{2\varepsilon_0 n^2 \Delta t}{2\varepsilon_0 n^2 + \Delta t\sigma_x}\left(\frac{\partial}{\partial x} E_y\right) \\
D_{y\_y}^{n+1} &= \frac{2\varepsilon_0 n^2 - \Delta t\sigma_y}{2\varepsilon_0 n^2 + \Delta t\sigma_y} D_{y\_y}^{n} + \frac{2\varepsilon_0 n^2 \Delta t}{2\varepsilon_0 n^2 + \Delta t\sigma_y}\left(\frac{\partial}{\partial y} n^2 E_y\right) \\
D_{x\_xx}^{n+1} &= \frac{2\varepsilon_0 n^2 - \Delta t\sigma_x}{2\varepsilon_0 n^2 + \Delta t\sigma_x} D_{x\_xx}^{n} + \frac{2\varepsilon_0 n^2}{2\varepsilon_0 n^2 + \Delta t\sigma_x}\left[\frac{\partial}{\partial x}\frac{1}{n^2} D_{x\_x}^{n} - \frac{\partial}{\partial x}\frac{1}{n^2} D_{x\_x}^{n-1}\right] \\
D_{x\_yy}^{n+1} &= \frac{2\varepsilon_0 n^2 - \Delta t\sigma_y}{2\varepsilon_0 n^2 + \Delta t\sigma_y} D_{x\_yy}^{n} + \frac{2\varepsilon_0 n^2}{2\varepsilon_0 n^2 + \Delta t\sigma_y}\left[\frac{\partial}{\partial y} D_{x\_y}^{n} - \frac{\partial}{\partial y} D_{x\_y}^{n-1}\right] \\
D_{y\_yx}^{n+1} &= \frac{2\varepsilon_0 n^2 - \Delta t\sigma_x}{2\varepsilon_0 n^2 + \Delta t\sigma_x} D_{y\_yx}^{n} + \frac{2\varepsilon_0 n^2}{2\varepsilon_0 n^2 + \Delta t\sigma_x}\left[\frac{\partial}{\partial x}\frac{1}{n^2} D_{y\_y}^{n} - \frac{\partial}{\partial x}\frac{1}{n^2} D_{y\_y}^{n-1}\right] \\
D_{y\_xy}^{n+1} &= \frac{2\varepsilon_0 n^2 - \Delta t\sigma_y}{2\varepsilon_0 n^2 + \Delta t\sigma_y} D_{y\_xy}^{n} + \frac{2\varepsilon_0 n^2}{2\varepsilon_0 n^2 + \Delta t\sigma_y}\left[\frac{\partial}{\partial y} D_{y\_x}^{n} - \frac{\partial}{\partial y} D_{y\_x}^{n-1}\right] \\
D_{y\_yy}^{n+1} &= \frac{2\varepsilon_0 n^2 - \Delta t\sigma_y}{2\varepsilon_0 n^2 + \Delta t\sigma_y} D_{y\_yy}^{n} + \frac{2\varepsilon_0 n^2}{2\varepsilon_0 n^2 + \Delta t\sigma_y}\left[\frac{\partial}{\partial y}\frac{1}{n^2} D_{y\_y}^{n} - \frac{\partial}{\partial y}\frac{1}{n^2} D_{y\_y}^{n-1}\right] \\
D_{y\_xx}^{n+1} &= \frac{2\varepsilon_0 n^2 - \Delta t\sigma_x}{2\varepsilon_0 n^2 + \Delta t\sigma_x} D_{y\_xx}^{n} + \frac{2\varepsilon_0 n^2}{2\varepsilon_0 n^2 + \Delta t\sigma_x}\left[\frac{\partial}{\partial x} D_{y\_x}^{n} - \frac{\partial}{\partial x} D_{y\_x}^{n-1}\right] \\
D_{x\_xy}^{n+1} &= \frac{2\varepsilon_0 n^2 - \Delta t\sigma_y}{2\varepsilon_0 n^2 + \Delta t\sigma_y} D_{x\_xy}^{n} + \frac{2\varepsilon_0 n^2}{2\varepsilon_0 n^2 + \Delta t\sigma_y}\left[\frac{\partial}{\partial y}\frac{1}{n^2} D_{x\_x}^{n} - \frac{\partial}{\partial y}\frac{1}{n^2} D_{x\_x}^{n-1}\right] \\
D_{x\_yx}^{n+1} &= \frac{2\varepsilon_0 n^2 - \Delta t\sigma_x}{2\varepsilon_0 n^2 + \Delta t\sigma_x} D_{x\_yx}^{n} + \frac{2\varepsilon_0 n^2}{2\varepsilon_0 n^2 + \Delta t\sigma_x}\left[\frac{\partial}{\partial x} D_{x\_y}^{n} - \frac{\partial}{\partial x} D_{x\_y}^{n-1}\right]
\end{aligned}
\tag{5.13}
$$

with $\sigma = 0$ in the non-PML region.

5.2.2 Semivectorial Scheme

The semivectorial scheme is a special case of full vectorial scheme when A_{xy} and A_{yx} in Eq.(5.3) are both equal to zero. Thus the semivectorial compact 2D FDTD with UPML absorbing boundary conditions for optical waveguide can be derived from the full vectorial scheme described in Eq.(5.12)-(5.13) by eliminating cross terms of the two perpendicular polarization electric fields, which yields

$$E_x^{n+1} = -E_x^{n-1} + 2E_x^n + \frac{c^2\Delta t}{n^2}\left(D_{x\_xx}^n - D_{x\_xx}^{n-1}\right) + \frac{c^2\Delta t}{n^2}\left(D_{x\_yy}^n - D_{x\_yy}^{n-1}\right) - \frac{\beta^2 c^2 \Delta t^2}{n^2} E_x^n$$
$$E_y^{n+1} = -E_y^{n-1} + 2E_y^n + \frac{c^2\Delta t}{n^2}\left(D_{y\_yy}^n - D_{y\_yy}^{n-1}\right) + \frac{c^2\Delta t}{n^2}\left(D_{y\_xx}^n - D_{y\_xx}^{n-1}\right) - \frac{\beta^2 c^2 \Delta t^2}{n^2} E_y^n \quad (5.14)$$

where

$$\begin{aligned}
D_{x_x}^{n+1} &= \frac{2\varepsilon_0 n^2 - \Delta t\sigma_x}{2\varepsilon_0 n^2 + \Delta t\sigma_x} D_{x_x}^n + \frac{2\varepsilon_0 n^2 \Delta t}{2\varepsilon_0 n^2 + \Delta t\sigma_x}\left(\frac{\partial}{\partial x} n^2 E_x\right) \\
D_{x_y}^{n+1} &= \frac{2\varepsilon_0 n^2 - \Delta t\sigma_y}{2\varepsilon_0 n^2 + \Delta t\sigma_y} D_{x_y}^n + \frac{2\varepsilon_0 n^2 \Delta t}{2\varepsilon_0 n^2 + \Delta t\sigma_y}\left(\frac{\partial}{\partial y} E_x\right) \\
D_{y_x}^{n+1} &= \frac{2\varepsilon_0 n^2 - \Delta t\sigma_x}{2\varepsilon_0 n^2 + \Delta t\sigma_x} D_{y_x}^n + \frac{2\varepsilon_0 n^2 \Delta t}{2\varepsilon_0 n^2 + \Delta t\sigma_x}\left(\frac{\partial}{\partial x} E_y\right) \\
D_{y_y}^{n+1} &= \frac{2\varepsilon_0 n^2 - \Delta t\sigma_y}{2\varepsilon_0 n^2 + \Delta t\sigma_y} D_{y_y}^n + \frac{2\varepsilon_0 n^2 \Delta t}{2\varepsilon_0 n^2 + \Delta t\sigma_y}\left(\frac{\partial}{\partial y} n^2 E_y\right) \\
D_{x_xx}^{n+1} &= \frac{2\varepsilon_0 n^2 - \Delta t\sigma_x}{2\varepsilon_0 n^2 + \Delta t\sigma_x} D_{x_xx}^n + \frac{2\varepsilon_0 n^2}{2\varepsilon_0 n^2 + \Delta t\sigma_x}\left[\frac{\partial}{\partial x}\frac{1}{n^2} D_{x_x}^n - \frac{\partial}{\partial x}\frac{1}{n^2} D_{x_x}^{n-1}\right] \\
D_{x_yy}^{n+1} &= \frac{2\varepsilon_0 n^2 - \Delta t\sigma_y}{2\varepsilon_0 n^2 + \Delta t\sigma_y} D_{x_yy}^n + \frac{2\varepsilon_0 n^2}{2\varepsilon_0 n^2 + \Delta t\sigma_y}\left[\frac{\partial}{\partial y} D_{x_y}^n - \frac{\partial}{\partial y} D_{x_y}^{n-1}\right] \\
D_{y_yy}^{n+1} &= \frac{2\varepsilon_0 n^2 - \Delta t\sigma_y}{2\varepsilon_0 n^2 + \Delta t\sigma_y} D_{y_yy}^n + \frac{2\varepsilon_0 n^2}{2\varepsilon_0 n^2 + \Delta t\sigma_y}\left[\frac{\partial}{\partial y}\frac{1}{n^2} D_{y_y}^n - \frac{\partial}{\partial y}\frac{1}{n^2} D_{y_y}^{n-1}\right] \\
D_{y_xx}^{n+1} &= \frac{2\varepsilon_0 n^2 - \Delta t\sigma_x}{2\varepsilon_0 n^2 + \Delta t\sigma_x} D_{y_xx}^n + \frac{2\varepsilon_0 n^2}{2\varepsilon_0 n^2 + \Delta t\sigma_x}\left[\frac{\partial}{\partial x} D_{y_x}^n - \frac{\partial}{\partial x} D_{y_x}^{n-1}\right]
\end{aligned} \quad (5.15)$$

and where $\sigma = 0$ in the non-PML region.

5.2.3 Scalar Scheme

Similarly, when the electrical field is assumed to be continuous in both x and y direction, the scalar compact 2D FDTD with UPML absorbing boundary conditions for optical waveguide can also be derived from the semivectorial scheme described in Eq.(5.14) by keeping only one of the two perpendicular polarization electric fields which yields

$$\Psi^{n+1} = -\Psi^{n-1} + 2\Psi^n + \frac{c^2\Delta t}{n^2}\left(D_{x\_xx}^n - D_{x\_xx}^{n-1}\right) + \frac{c^2\Delta t}{n^2}\left(D_{x\_yy}^n - D_{x\_yy}^{n-1}\right) - \frac{\beta^2 c^2 \Delta t^2}{n^2}\Psi^n \quad (5.16)$$

where

$$
\begin{aligned}
D_{x\_x}^{n+1} &= \frac{2\varepsilon_0 n^2 - \Delta t\sigma_x}{2\varepsilon_0 n^2 + \Delta t\sigma_x} D_{x\_x}^{n} + \frac{2\varepsilon_0 n^2 \Delta t}{2\varepsilon_0 n^2 + \Delta t\sigma_x}\left(\frac{\partial}{\partial x} E_x\right) \\
D_{x\_y}^{n+1} &= \frac{2\varepsilon_0 n^2 - \Delta t\sigma_y}{2\varepsilon_0 n^2 + \Delta t\sigma_y} D_{x\_y}^{n} + \frac{2\varepsilon_0 n^2 \Delta t}{2\varepsilon_0 n^2 + \Delta t\sigma_y}\left(\frac{\partial}{\partial y} E_x\right) \\
D_{x\_xx}^{n+1} &= \frac{2\varepsilon_0 n^2 - \Delta t\sigma_x}{2\varepsilon_0 n^2 + \Delta t\sigma_x} D_{x\_xx}^{n} + \frac{2\varepsilon_0 n^2}{2\varepsilon_0 n^2 + \Delta t\sigma_x}\left[\frac{\partial}{\partial x} D_{x\_x}^{n} - \frac{\partial}{\partial x} D_{x\_x}^{n-1}\right] \\
D_{x\_yy}^{n+1} &= \frac{2\varepsilon_0 n^2 - \Delta t\sigma_y}{2\varepsilon_0 n^2 + \Delta t\sigma_y} D_{x\_yy}^{n} + \frac{2\varepsilon_0 n^2}{2\varepsilon_0 n^2 + \Delta t\sigma_y}\left[\frac{\partial}{\partial y} D_{x\_y}^{n} - \frac{\partial}{\partial y} D_{x\_y}^{n-1}\right]
\end{aligned}
\tag{5.17}
$$

and where $\sigma = 0$ in the non-PML region.

5.3 Extraction of Mode Parameters by Matrix Pencil Method

When the wave equations are solved in frequency domain, the operation frequency is treated as an input parameter whereas the propagation constant β is an output in the mode calculation. In our algorithm, the wave equations are solved in time domain and hence β is selected as an input parameter so as to the mode frequencies ω_m , the mode losses ξ_m, and the optical fields (Φ_m) for different modes are extracted in the post processing after the FDTD simulation. Since the optical waveguide has a uniform index along the propagation direction, an arbitrary transverse field ($\Psi_t(x,y,t)$) in the waveguide can be represented by the summation of the eigenmodes $\Phi_m(x,y)$

$$
\Psi_t(x,y,t) = \sum_{m=0}^{\infty} A_m \exp(j\omega_m t)\exp(-\xi_m t)\Phi_m(x,y) \tag{5.18}
$$

In order to extract the mode parameter ω_m for different modes, the Fourier transform can be employed to obtain the frequency spectrum from the steady-state time domain optical field captured in a window with proper width. The mode parameters ω_m are the positions of resonant peaks in the frequency spectrum. Since the accuracy of the mode frequency

ω_m depends on the resolution of the frequency spectrum, a large time window in FDTD simulation is required to achieve a high accuracy, which is extremely computation intensive. It is also very difficult to obtain the mode loss ξ_m accurately by fitting Lorentz shapes centered at mode frequencies in the frequency spectrum. The matrix pencil method (MPM) is proposed to overcome the drawback of the Fourier transform method so that the mode frequency ω_m and mode losses ξ_m can be extracted accurately with reasonable computation resources.

In the MPM, the time-dependent signal is represented by a summation of a series of complex exponentials[109] as follow.

$$S(t) = \sum_{m=0}^{M} R_m \exp(s_m t) \tag{5.19}$$

R_m is a real number and s_m is a complex number. By mapping Eq. (5.18) to Eq.(5.19), the mode frequency ω_m and mode loss factor ξ_m can both be obtained by

$$\begin{aligned} \omega_m &= \mathrm{Im}(s_m) \\ \xi_m &= -\mathrm{Re}(s_m) \end{aligned} \tag{5.20}$$

The loss factor can be easily converted to attenuation coefficient α_m by the relation $\alpha_m = \xi_m / (d\omega_m / d\beta_m)$. It will be illustrated in the following sections that only limited number of field samples in time domain is required by MPM to obtain mode parameters accurately, which is more efficient compared with Fourier transform method.

5.4 Assessment and Validation

In order to validate the mode solver presented in this chapter, we calculated the real guided mode of a rectangular channel waveguide and the complex leaky mode of a ridge waveguide.

5.4.1 Guided Mode Analysis

The square channel waveguide structure is shown in Figure 5.1. The width (w_1) of the square core region is chosen as $2\mu m$ and the indices of the core region and the cladding region are 1.52 and 1.46, respectively. The number of PML layers is chosen to be 20 in our simulation.

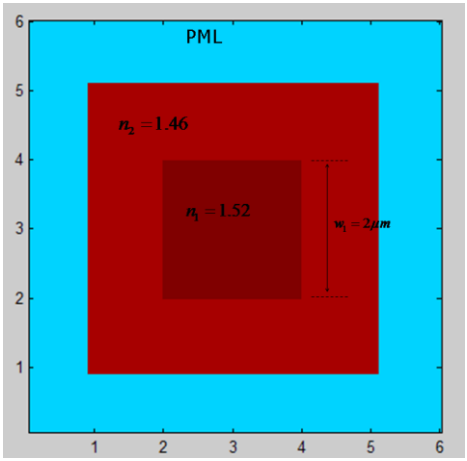

Figure 5.1 Schematic diagram of the square channel waveguide structure, $n_1 = 1.52$, $n_2 = 1.46$, $w_1 = 2\mu m$, PML Layers = 20.

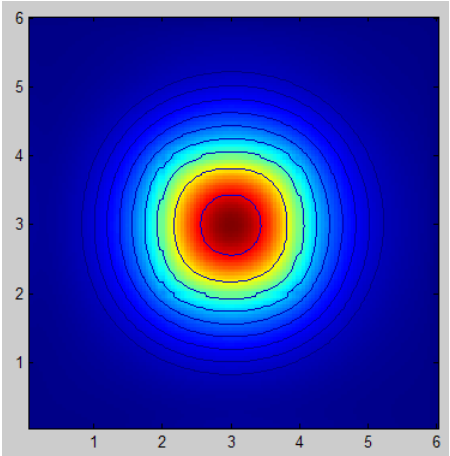

Figure 5.2 Fundamental mode profile of the square channel waveguide.

An initial optical field with the pre-set propagation constant β and the Gaussian distribution is launched at the position (x_0, y_0) inside the core region in FDTD simulation. The source is a Gaussian modulated sinusoidal waveform in time domain. The waveform in the frequency domain also follows a Gaussian distribution with a central frequency of ω_0, formulated by

$$E_{src}(x,y,t) = A\exp\left(-\frac{(x-x_0)^2+(y-y_0)^2}{R_m}\right)\exp\left(-\frac{(t-t_0)^2}{T_m}\right)\sin(\omega_0 t) \qquad (5.21)$$

When the steady-state is reached after the optical field propagates in the waveguide for a certain period of time, proper numbers of temporal samples of the optical field are taken at one position inside the core region in MPM analysis from which the resonant frequency for each mode can be extracted. The accuracy of extracted values by the full-vectorial solver is validated through comparisons with benchmark results obtained by Goell's model[120] in Figure 5.3. Note that for the given FDTD time steps and the MPM

sampling numbers, the relatively larger error is observed near the cut-off. This is due to the reason that the effective width of each mode is increasing with the decrease of the normalized frequency V (horizontal label in Figure 5.3). By using a larger computation window (in space), this error can be reduced.

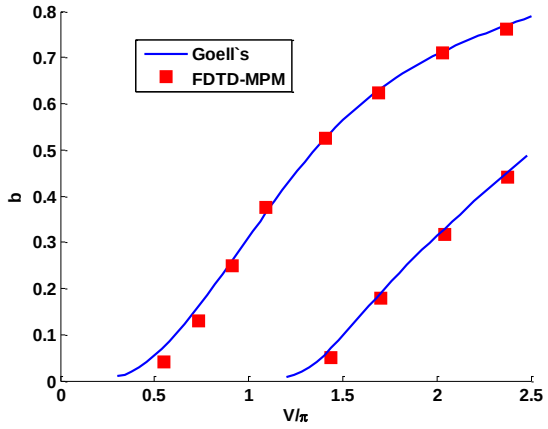

Figure 5.3 Guided modal analysis by Goell's model and solver in this chapter.

Once the mode frequency ω_m is extracted, the field distribution of each mode (Φ_m) can be readily obtained from the instantaneous field (Ψ_t) by the formula

$$\Phi_m(x,y) = \Delta t \sum_{n=0}^{N_t-1} \Psi_t(x,y,t)\exp(j\omega_m n\Delta t)\exp(-\xi_m n\Delta t) \qquad (5.22)$$

Figure 5.2 shows the calculated field pattern of the fundamental mode for the square channel waveguide depicted in Figure 5.1.

5.4.2 Leaky Mode Analysis

In this section, the proposed method is applied to a deep-etched GaAs-AlGaAs optical waveguide structure[121] shown in Figure 5.4. The indices are 3.4519, 3.4434, 3.3955, 3.3675 for 5%, 6.5%, 15% and 20% AlGaAs material, respectively, and 3.4804

for GaAs cap and substrate. Note that the refractive index of the 5% AlGaAs core region is higher than those of the upper and lower cladding layers. The fundamental mode can be well confined in the rib. However high order modes are much lossier and can strongly leak through the lower 15% AlGaAs cladding layer and radiate into the substrate[121].

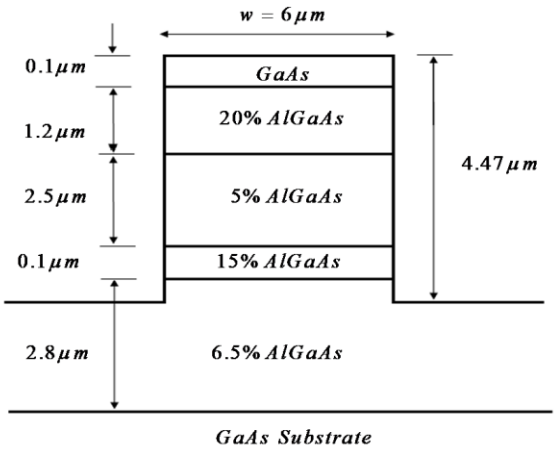

Figure 5.4 Schematic diagram of a deep-etched GaAs-alGaAs optical waveguide structure.

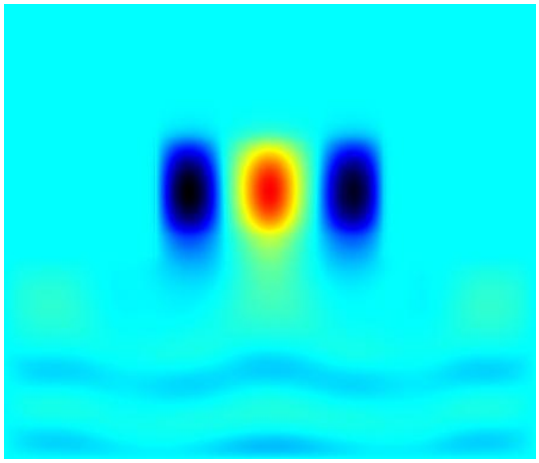

Figure 5.5 TE20 mode profile of the ridge waveguide.

The TE20 mode frequency ω_m and attenuation coefficient α_m obtained by the proposed method with full-vectorial scheme are compared with those obtained from FD mode solver [99] in Table 5.1. It also shows that results are well agreed with each other. The accuracy of the extracted results can be controlled by several factors such as the FDTD time steps and the number of sampling points for the MPM. For critical applications, the accuracy can be further enhanced with the cost of extra computation efforts. The TE20 mode profile of the ridge waveguide under investigation is calculated and shown in Figure 5.5. It is observed that the field is radiative towards the substrate.

Table 5.1 Leaky modal analysis by FD mode solver and solver in this chapter

Parameters	FD Mode Solver	FDTD+MPM
Wavelength	1.06400um	1.06358um
Propagation Constant	20.30006/um	20.30006/um
Effective Index	3.43763	3.43636
Attenuation	0.00057 dB/um	0.00061 dB/um

5.5 Error Analysis and Convergence Test

The accuracy of the extracted parameters for the optical waveguide modal analysis depends on several factors, namely, the accuracy of the propagating field simulated by the FDTD and that of the MPM post processing. The former is related to the transverse mesh size whereas the latter is related to the FDTD running time (i.e., related to the sampling window in time) and MPM sample numbers. Assume that the FDTD mesh size is chosen in accordance with the numerical dispersion condition which is $\delta \le \lambda/12$. We may focus exclusively on the impact of the accuracy associated with the post data processor. Under this assumption, the convergence of the mode solver as

functions of the FDTD running time and the MPM sample size is simulated and analyzed for the square channel waveguide structure described previously in section 5.4.

5.5.1 Convergence with FDTD Time Steps

The extracted wavelength of the fundamental mode is calculated with 480x480 mesh points and 7.810043rad/um propagation constant. The percentage error is defined with respect to the benchmark results obtained from the FD mode solver and shown in Figure 5.6 as a function of FDTD time steps for a fixed number (1000) of MPM samples. It is observed that the error of the extracted parameter converges rapidly toward zero with the increase of FDTD time steps.

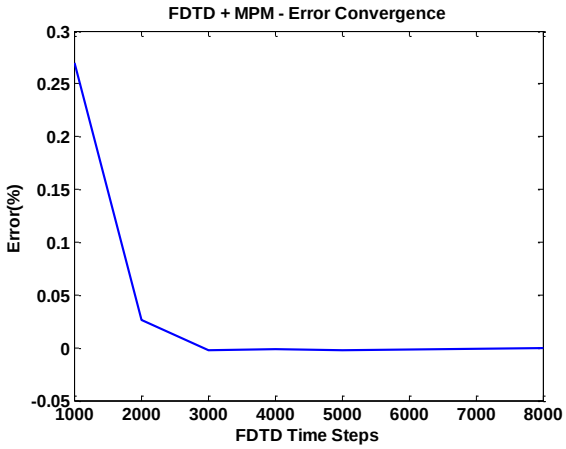

Figure 5.6 Percentage error of extracted wavelength of fundamental mode versus different FDTD time steps.

5.5.2 Convergence with MPM Sample Number

To study the convergence of this method with MPM sample numbers, the FDTD time steps is chosen to be 8000. The mode calculation is then carried out for the square channel waveguide with different numbers of MPM samples. The percentage error of

extracted wavelength of the fundamental mode is shown in Figure 5.7. It is noted that the extracted parameter converges well with the increase of MPM sample numbers.

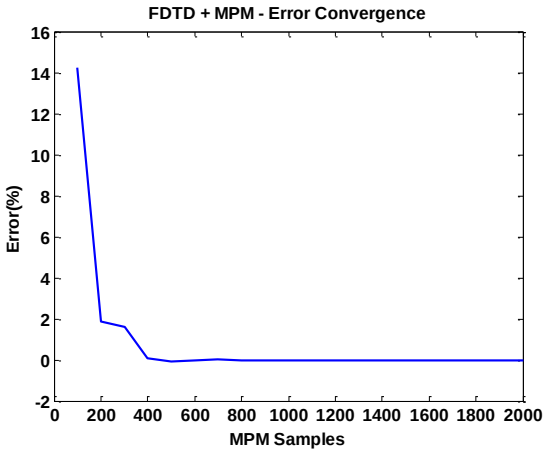

Figure 5.7 Percentage error of extracted wavelength of fundamental mode versus MPM sample numbers.

5.6 Performance of the Mode Solver on GPUs

In the mode solver based on FDTD, the most computational intensive work is for the FDTD simulation. Since the index of the waveguide is uniform along the propagation direction (z), the compact FDTD method is employed so that significant computation time can be saved. However, in the modal analysis of an optical waveguide with relatively large dimensions, a large number of meshes are required to ensure adequate accuracy. This leads to drastic increase in computation time and render this approach not applicable as a practical tool for mode calculation on CPUs of today's desktop computers. In order to improve the computation efficiency, this method is implemented on NVidia GTX 295 GPUs with parallel calculation algorithms. Comparisons of the memory and

time consumptions are made in implementing this method on GPUs, CPU as well as the FD mode solver.

5.6.1 Memory Consumption

When the FDTD mode solver is implemented on CPU and GPU, the memory requirements are virtually the same. The memory consumptions for the scalar mode calculation by the standard and the accelerated FDTD and the conventional FD mode solvers are estimated and shown in Figure 5.8. It is clearly shown that the memory consumption for the FDTD methods scale much slowly than that of the FD eigen solver. A saving of 94.6% memory can be realized for a problem of total mesh points of 480x480. In addition, we also examined the memory requirements of the scalar, semi-vector and full-vector mode calculations by the accelerated FDTD solvers showing in Figure 5.9. It is noted that there are moderate increases of memory consumption for the full and semi-vector modes (e.g., 20% and 35% increase, respectively) in comparison with the scalar mode. We conclude that the FDTD method is far more scalable than the FD scheme in terms of memory requirement and hence is capable of solving waveguide problems with large number of mesh points.

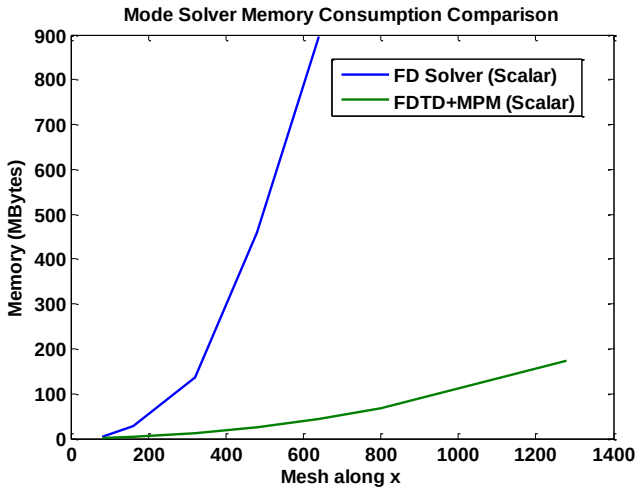

Figure 5.8 Memory consumptions of the scalar mode calculation by the accelerated FDTD and the conventional FD mode solvers.

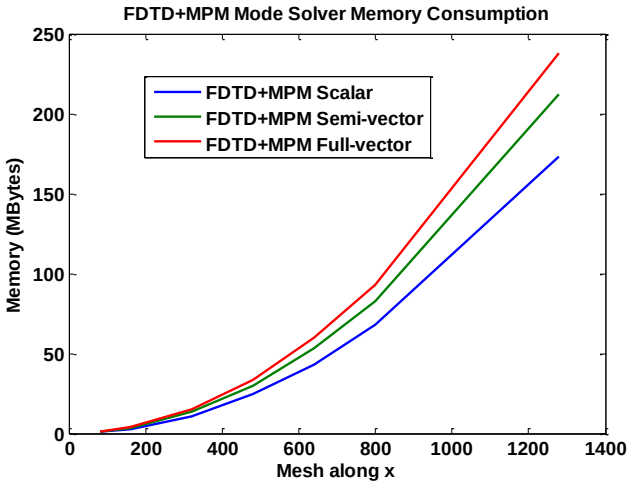

Figure 5.9 Memory consumptions of the scalar, semi-vector and full-vector mode calculations by the accelerated FDTD solvers.

5.6.2 Time Consumption

The computational efficiency is measured by the computation time required to achieve a desirable accuracy. In Figure 5.10, the computation time for scalar mode by the

standard FDTD, accelerated FDTD and conventional FD solvers are plotted. Significant improvement in computation efficiency (e.g., reduction of computation time as much as 97% is realized for the scalar mode for a problem of total mesh points of 640x640) is achieved by the accelerated FDTD mode solver in comparison with the standard FDTD mode solver running on CPU of a standard desktop computer. It also shows that the computational efficiency of the accelerated FDTD method is in the same order of magnitude of the standard FD eigen mode solver. In Figure 5.11, the computation time for the scalar, semi-vector and full-vector modes by the accelerated FDTD mode solvers are plotted. It is noted that there are moderate increases of time consumption for the full and semi-vector modes in comparison with the scalar mode.

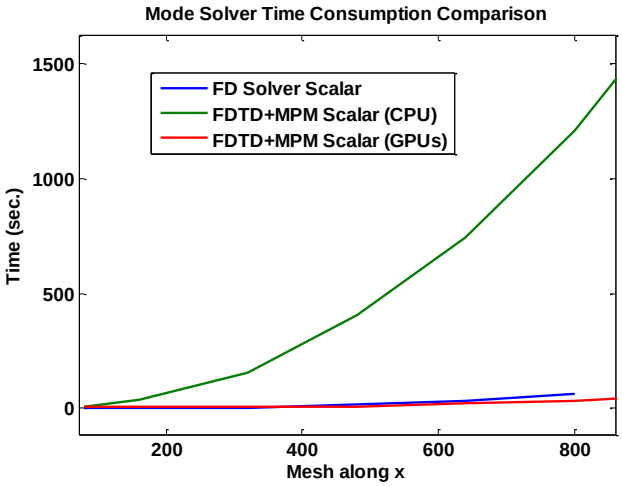

Figure 5.10 Time consumption of the scalar mode calculation by the standard FDTD, accelerated FDTD and the conventional FD mode solvers.

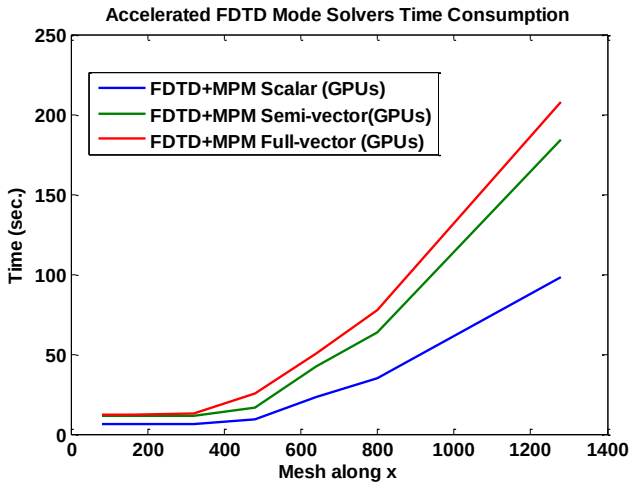

Figure 5.11 Time consumption of the scalar, semi-vector and full-vector mode calculations by accelerated FDTD mode solvers on GPUs.

5.7 Summary

It is proposed and demonstrated that the numerical mode solver based on the compact FDTD method in combination of the matrix pencil method (MPM) can be accelerated significantly by commercially available, low-cost and easy-to-implement high-performance computing techniques such as the CUDA algorithm on GPUs. In the meanwhile, the relative low memory requirements and simple numerical scheme inherent in the time explicit FDTD method is preserved. This idea is implemented and validated for calculations of scalar, semi-vector and full-vector modes and hence has general applicability to a wide range of optical waveguide problems. The advantages of this new approach become even more pronounced when the total number of meshes is large, in which the standard FDTD method is prohibitively time-consuming and the conventional FD solver is severely limited by its memory consumption.

Chapter 6 Circuit Model with Complex Mode Expansion Method

6.1 Introduction

In the design of optical devices and circuits, it is important to do the simulation by the aid of modern computation techniques before the fabrication to dramatically reduce the total cost. Several numerical methods, such as the Finite-Difference Time-Domain (FDTD) method[11-13], the Finite-Difference Frequency-Domain (FDFD) method[14-16], the Beam Propagating Method (BPM) [3-5], the Mode Matching Method (MMM) [6, 7], and the Couple Mode Theory (CMT) [8-10], have been widely adopted in academic research fields and commercial software packages. The FDTD method and FDFD method are rigorous numerical methods for simulating of electromagnetic field in time-domain and frequency-domain, respectively. They are powerful and accurate. However, they are both extremely memory and time consuming when applied to simulate large scale structures. A single modern personal computer can hardly afford such a task which requires many memory and computing resources. Although the FDTD method can be implemented to execute on multiple computers in parallel, there is too much burden on computing resources used for exchanging data between the corresponding computers involved in the computation. The BPM based on a reduced form of Maxwell's equations requires less computing resources. However, it is only suitable for paraxial propagation problems because of its slowly varying envelope approximation. The MMM is based on the mode expansion of the transverse fields and matching of boundary condition at refractive index discontinuities. It is quite computationally efficient. However, it cannot

be applied to devices with discontinuities out of perpendicular. The CMT's basic assumption that the weak perturbation does not affect the mode profiles in the waveguide limits its application only for weakly guided structures.

In analysis of the conventional microwave devices and circuits, a circuit theory based on scattering matrix formulation defined by the guided modes of waveguides connecting each part of the target structure[23, 24]. This theory can be borrowed for analyze the optical devices and circuits which can be partitioned into separated parts connected with relatively long waveguides in which only guided modes are considered. All the radiation effects in the connecting waveguides are neglected. For the compact optical devices and high density integrated optical circuits, the neglected radiation effects may cause significant deviation.

In this chapter, a circuit model based on the complex mode expansion of the interconnecting structures is proposed for analysis of optical devices and integrated optical circuits with compact geometries. The interconnecting structures are not limited to waveguides with guided modes. Any structure with uniform refractive index along the interconnecting direction could be defined as an interconnecting structure, such as waveguides with guided and/or leaky modes, and even free space. The lengths of the interconnecting structures can be extremely short, even zero. In this method both the guided and radiation waves are considered. It is rigorous and versatile. It can easily be implemented to run in a parallel computing environment with negligible burden on computing resources.

This chapter is organized as follows. The partition methodology is demonstrated by way of example in section 1. The complex mode expansion method is described in section 2. The complex scattering matrix is introduced and the parameter extraction method for the complex scattering matrix is described in section 3. The cascade of the scattering matrix in each block is demonstrated in section 4. The proposed method is verified in section 5 and an application is given in section 6.

6.2 Partition Methodology and Building Blocks

In the complex mode expansion circuit theory, a large-scale structure is partitioned into a collection of interconnected building blocks with rectangular domains. The interface of two adjacent building blocks is defined as a port. The field at a port is expanded by the complex modes of a waveguide with the refractive index profile at this port. The building blocks are divided into two types according to the simulation method employed to solve the individual building block: the functional optical element and the optical connector. The functional optical element contains a complex optical structure need to be solved by a rigorous numerical method such as the FDTD method. The optical connector is an interconnecting structure with two ports connecting two adjacent functional optical elements. It is a structure with uniform refractive index along the interconnecting direction. It could be a waveguide with guided and/or leaky modes, or even free space. The optical connector is solved by the analytical manipulation of the complex modes used to expand the fields at the two ports.

Usually the ways to partition a large scale structure into building blocks are not unique. However, several rules should be hold in the partitioning process as many as possible to minimize the total computational costs and maximize the final result accuracy. The first rule is maximizing the size of the optical connectors and minimizing the size of the optical functional elements. The computational cost for solving an optical connector is negligible compared with that for solving an optical functional element. Thus, the purpose of this rule is to minimize the total computational costs. The second rule is maximizing the number of optical functional elements with the same or symmetric geometries. N blocks with the same or symmetric geometries can be solved at once instead of N times. Therefore, the computational costs can be extremely reduced. The third rule is that the interface or port of the building blocks should better be located at a place with stronger guided structure. When this rule is applied, less complex modes need to be involved in the computation or high accuracy could be achieved. The priority of the three rules is varying in partition different structures. The overall target is to minimize the total computational costs and maximize the final result accuracy.

An example is given to demonstrate how to partition a structure in an optimized way. The structure of an optical band-pass filter is depicted in Figure 6.1 (a). The band-pass filter consists of two identical air slots on a waveguide. The width of the waveguide is 2um. The core and cladding refractive index of the waveguide are n1=3.260 and n0=3.218, respectively. The thickness of the two slots is b. The distance between the two slots is a. The structure is partitioned in to three blocked as shown in Figure 6.1(a). Block #1 and #3 are functional optical elements and block #2 is an optical connector. According to the first

rule, the size of the block#1 and #3 should be minimized and that of the block #2 should be maximized. According to the second rule, block #1 and #3 should be partitioned to be identical. According to the third rule, the interfaces of block#1 and 3 should not be located in the two slots because a lot of complex modes are required to expand the field in the slot accurately. Another way to partition the same structure is depicted in Figure 6.1(b). In this partition, block #1 and block #4 is identical. Block #2 and block #5 is identical. Block #1 and block #4 mirror block#2 and block#5, respectively. Therefore, blocks #1, 2, 4, 5 only need to be solved at once. Both the first and this partition scheme require one numerical simulation to solve the functional optical elements and one analytical operation to solve an optical connector. Compared with the first partition scheme, the size of the functional optical elements in the second partition scheme is smaller. But one interface of each functional optical element is located in the air slots. Therefore, there is a tradeoff between the first rule and third rule. It is hard to say which partition scheme is better before doing overall analysis.

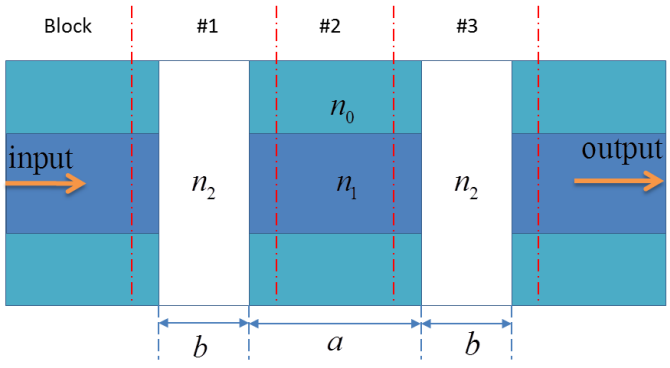

(a)

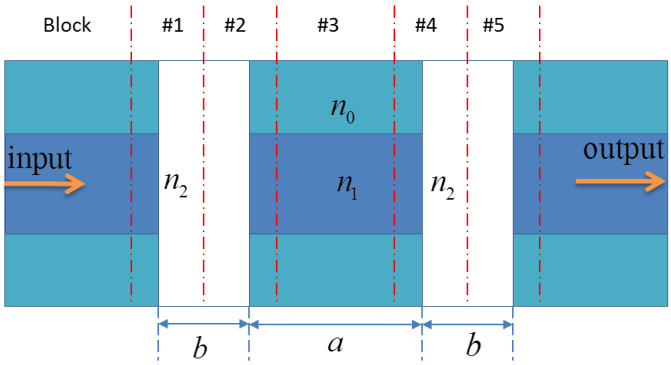

(b)

Figure 6.1 (a) Partition of a structure of an optical band-pass filter

(b) another way to partition the structure

6.3 Complex Mode Expansion Method

The conventional waveguide mode theory has been successfully employed to analyze well guided waveguide problems. However, it can hardly be applied in reality for solving a waveguide problem with non-negligible radiations. Because the radiation mode in the conventional waveguide mode theory is continuous, integration operations, which are computational power consuming, are requires to hand the continuous modes. Recently, a complex mode theory for waveguide is developed. In this theory, the waveguide is boxed by the perfectly matched layer (PML) and terminated by the perfect reflection boundary condition (PRB) at the outermost layer. Due to the PRB, the radiation modes are discretized to complex modes whose propagation constants have both real and imaginary parts. If the original waveguide has guided modes, the guided modes could be almost unaffected if the box size and the PML parameters are properly chosen.

The complex modes can be obtained by a mode solver by using FDTD method, finite difference method, smooth transition method, etc. Once the complex modes are obtained, the electromagnetic fields can be expanded by the complex modes as follows.

$$\begin{aligned}\mathbf{E} &= \sum_{m=1}^{M}\left(a_m + b_m\right)\mathbf{e}_m \\ \mathbf{H} &= \sum_{m=1}^{M}\left(a_m - b_m\right)\mathbf{h}_m\end{aligned} \tag{6.1}$$

where $\mathbf{E}$ and $\mathbf{H}$ are the transverse electric and magnetic fields, $\mathbf{e}_m$ and $\mathbf{h}_m$ are the m-th modal fields obtained by the complex mode solver, a_m and b_m are the amplitude of the m-th mode propagating to two opposite directions, respectively. The modal fields of the complex modes are normalized in terms of power by the expression

$$\frac{1}{4}\iint \mathrm{Re}\left(\mathbf{e}_m \times \mathbf{h}_m^* + \mathbf{e}_m^* \times \mathbf{h}_m\right)\hat{z}da = 1 \tag{6.2}$$

where $\hat{z}$ is the unit vector of the mode propagation direction. In the complex mode theory, the mode orthogonality is valid, which means

$$\frac{\iint \left(\mathbf{e}_n \times \boldsymbol{h}_m + \boldsymbol{e}_m \times \mathbf{h}_n\right)\hat{z}da}{2\iint \left(\boldsymbol{e}_n \times \boldsymbol{h}_n\right)\hat{z}da} = \begin{cases}1, m = n \\ 0, m \neq n\end{cases} \tag{6.3}$$

In contrast with the conventional mode theory, the mode power orthogonality is not valid anymore, which means,

$$\frac{\iint \left(\mathbf{e}_n \times \boldsymbol{h}_m^* + \boldsymbol{e}_m^* \times \mathbf{h}_n\right)\hat{z}da}{2\iint \left(\boldsymbol{e}_n \times \boldsymbol{h}_n^*\right)\hat{z}da} = \begin{cases}1, m = n \\ \neq 0, m \neq n\end{cases} \tag{6.4}$$

As an example of the complex mode theory, a 0.8um waveguide is solved by a complex mode solver. The waveguide is boxed by the PBR and PML in the center of a 8.8 um

region. The thickness of the PML is 3um. The refractive index of the waveguide and the first 50 complex modes (ordered by the imaginary part of the effective index) are depicted in Figure 6.2 (a). The real and imaginary parts of the complex effective index of the first 50 complex modes are given in Figure 6.2 (b).

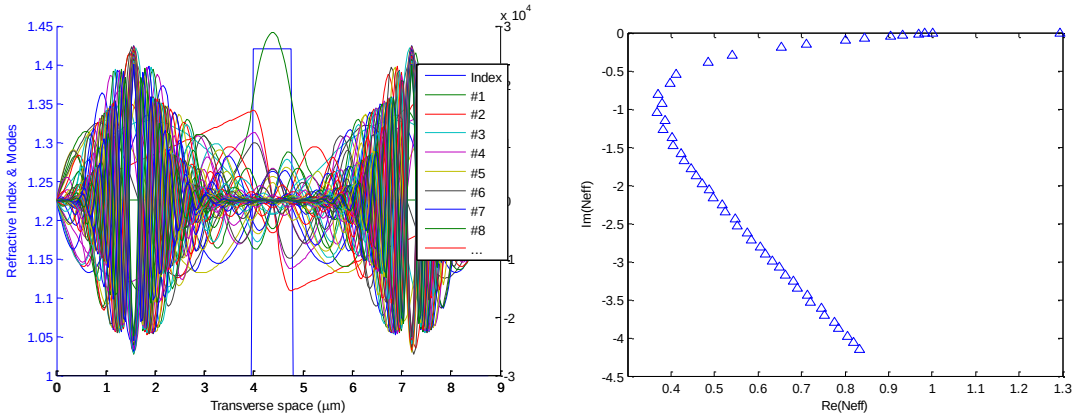

(a) (b)

Figure 6.2 (a)The refractive index and 50 complex mode profiles of a 0.8um waveguide solved by a complex mode solver (b)The real and imaginary parts of the complex effective index of the first 50 complex modes.

The results calculated from the mode orthogonality equation (6.3) and the power orthogonality equation (6.4) are depicted in Figure 6.3(a) and (b), respectively. It shows clearly that the mode orthogonality is hold very well while the power orthogonality is not.

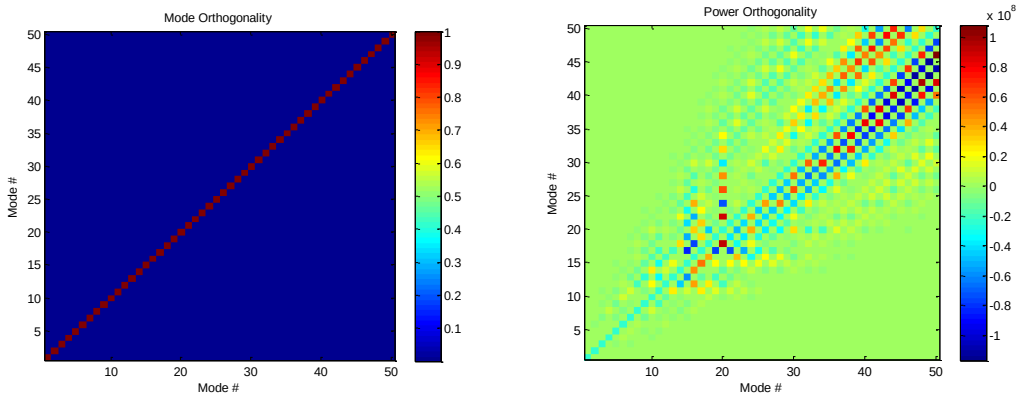

(a) (b)

Figure 6.3 (a) Results calculated by the mode orthogonality equation (b) Results calculated by the power orthogonality equation

To exam the propagation properties of the complex mode, several modes including the guided and discretized radiation modes are launched individually in the waveguide structure shown in Figure 6.4. The location of the bottom yellow line in Figure 6.4 is defined as port #1 and the top yellow line is defined as port #2. The modal fields are launched at port #1. The field will propagate 12um along the waveguide to reach port #2. The evolution of electric field (TE) is simulated by the FDTD method with 1.55um continuous wave.

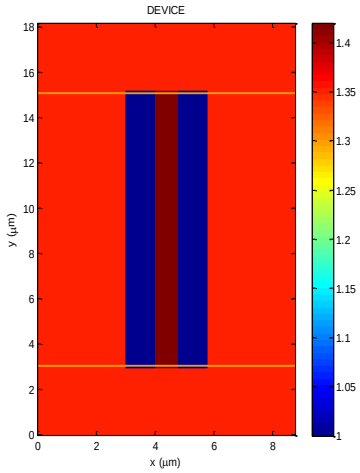

Figure 6.4 A 0.8um waveguide with index=1.42 surrounded by air boxed in a PBR region with 3um thick PML.

The static state electric fields of launching the mode #1, #4 and #6 are shown in Figure 6.5 (a), (b) and (c), respectively.

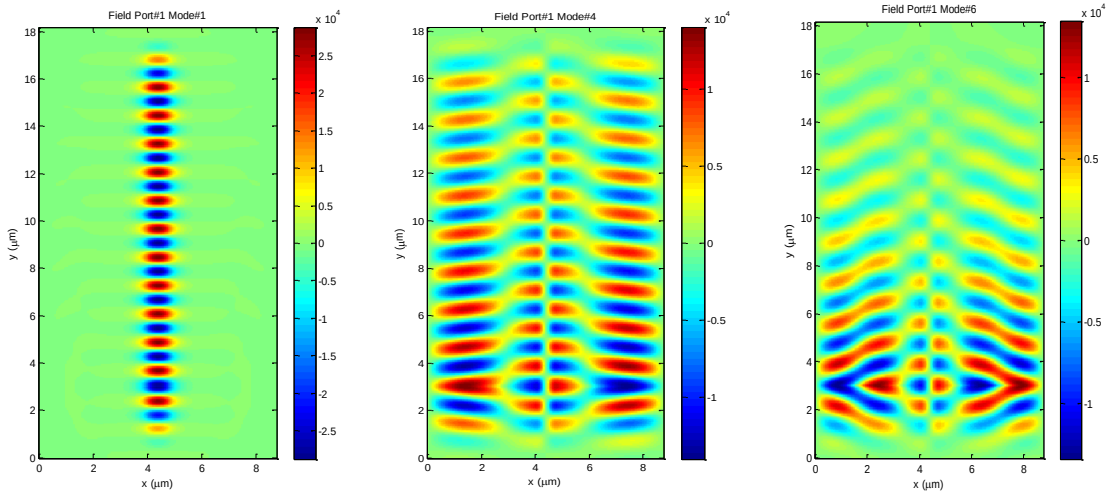

(a) (b) (c)

Figure 6.5 The static state electric field of launching a complex mode at port #1: (a) mode #1 (b) mode #4 (c) mode #6

Figure 6.5 (a) shows that the first mode is well confined in the waveguide and propagates with almost no loss. This mode is a guided mode. Figure 6.5 (b) shows that the 4th order mode propagates with observable loss and a large ratio of energy exists at the cladding and PML region. The higher order mode is more lossy as shown in Figure 6.5 (c). The normalized amplitude and phase of the electric fields recorded at port #2 by launching the corresponding complex modes at port #1 are given in Figure 6.6. The amplitude and phase of the corresponding complex mode is depicted in the same figure of the electric field as a reference. It shows that both the guided and discretized radiation modes keep their modal field profiles very well when propagating in the corresponding waveguide. The amplitude of the discretized radiation mode is decaying because of the loss from radiation.

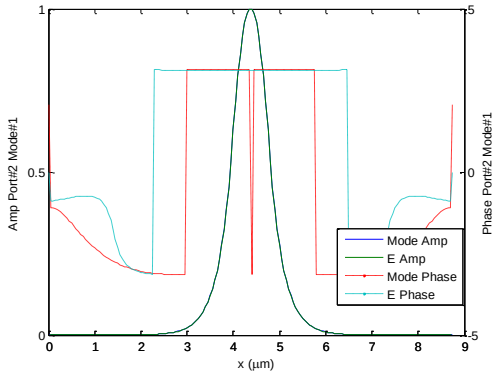

(a)

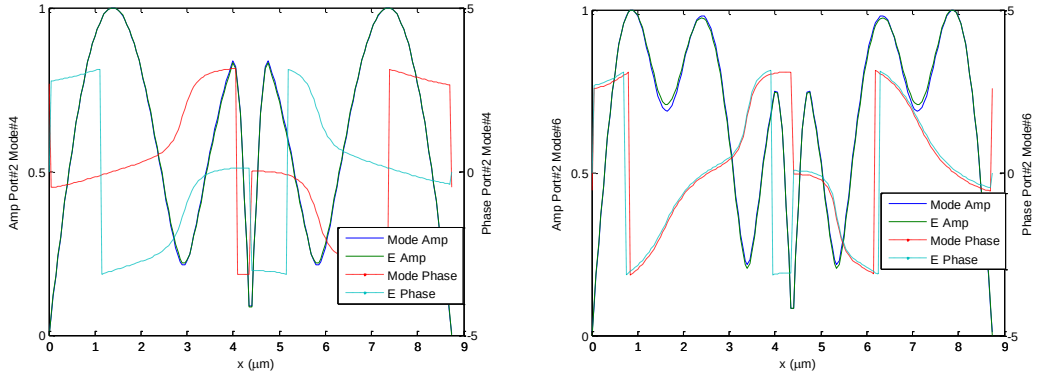

(b) (c)

Figure 6.6 The amplitude and phase of the electric field recorded at port 2 and the corresponding complex mode launched at port 1: (a) mode #1 (b) mode #4 (c) mode #6

6.4 Complex Scattering Matrix

In the proposed circuit theory, the complex scattering matrix is employed to describe the relationship of the electromagnetic fields at two ports of a building block, including the functional optical element and the optical connector, based on complex mode expansion of the electromagnetic fields at the two ports. The complex mode expansion method is introduced in previous section. The number of the complex modes for a port is chosen by the characteristic of the field at the port and the degree of accuracy required for the interconnection. Once the complex modes for every port are obtained by a complex mode solver, the complex scattering matrix linking the amplitudes of the complex modes of the two ports can be obtained by a parameter extraction process. The complex scattering matrix and the parameter extraction method will be introduced by way of example in this section.

Figure 6.7 gives an example of a building block with the i-th and j-th port. Assume that M_i and M_j modes are chosen for the i-th port and j-th port, respectively.

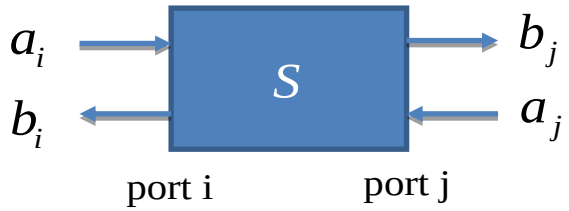

Figure 6.7 Amplitudes of in-going and out-going complex modes at two ports of a building block

a_i and b_i denote the amplitudes of in-going and out-going modes, respectively, for the i-th port. a_j and b_j are for the j-th port. The column matrix for each of them is given by

$$a_i = \begin{pmatrix} a_i^1 \\ \vdots \\ a_i^{M_i} \end{pmatrix} \tag{6.5}$$

$$b_i = \begin{pmatrix} b_i^1 \\ \vdots \\ b_i^{M_i} \end{pmatrix} \tag{6.6}$$

$$a_j = \begin{pmatrix} a_j^1 \\ \vdots \\ a_j^{M_j} \end{pmatrix} \tag{6.7}$$

$$b_j = \begin{pmatrix} b_j^1 \\ \vdots \\ b_j^{M_j} \end{pmatrix} \tag{6.8}$$

The scattering matrix linking the amplitudes of the modes at i-th and j-th ports is expressed by

$$\begin{pmatrix} b_j \\ b_i \end{pmatrix} = \begin{pmatrix} S_{11} & S_{12} \\ S_{21} & S_{22} \end{pmatrix} \begin{pmatrix} a_i \\ a_j \end{pmatrix} \tag{6.9}$$

where the sub-matrices S_{11}, S_{12}, S_{21} and S_{22} are given as

$$S_{11} = \begin{pmatrix} S_{11}^{ji} & \cdots & S_{1M_i}^{ji} \\ \vdots & \ddots & \vdots \\ S_{M_j 1}^{jj} & \cdots & S_{M_j M_i}^{ji} \end{pmatrix} \tag{6.10}$$

$$S_{12} = \begin{pmatrix} S_{11}^{jj} & \cdots & S_{1M_j}^{jj} \\ \vdots & \ddots & \vdots \\ S_{M_j 1}^{jj} & \cdots & S_{M_j M_j}^{jj} \end{pmatrix} \tag{6.11}$$

$$S_{21} = \begin{pmatrix} S_{11}^{ii} & \cdots & S_{1M_i}^{ii} \\ \vdots & \ddots & \vdots \\ S_{M_i 1}^{ii} & \cdots & S_{M_i M_i}^{ii} \end{pmatrix} \tag{6.12}$$

$$S_{22} = \begin{pmatrix} S_{11}^{ij} & \cdots & S_{1M_j}^{ij} \\ \vdots & \ddots & \vdots \\ S_{M_i 1}^{ij} & \cdots & S_{M_i M_j}^{ij} \end{pmatrix} \tag{6.13}$$

For a functional optical element building block which has total of P ports, the overall scattering matrix is given by

$$\begin{pmatrix} b_p \\ b_{p-1} \\ \vdots \\ b_1 \end{pmatrix} = \begin{pmatrix} S_{11} & S_{12} & \cdots & S_{1p} \\ S_{21} & S_{22} & \cdots & S_{2p} \\ \vdots & \vdots & \ddots & \vdots \\ S_{p1} & \cdots & \cdots & S_{pp} \end{pmatrix} \begin{pmatrix} a_1 \\ a_2 \\ \vdots \\ a_p \end{pmatrix} \tag{6.14}$$

For an optical connector building block shown in Figure 6.8, the total ports are always 2 and the two ports are identical. The set of complex modes for the two ports are the same.

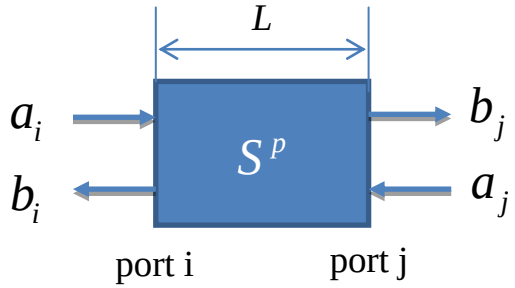

Figure 6.8 Amplitudes of in-going and out-going complex modes at two ports of an optical connector with length L

The reflections and even mode couplings in the optical connector are negligible. Therefore, the scattering matrix for the optical connector can be simplified from its two-port general form defined in (6.9) to the propagation form expressed as

$$\begin{pmatrix} b_j \\ b_i \end{pmatrix} = \begin{pmatrix} S^p{}_{11} & 0 \\ 0 & S^p{}_{22} \end{pmatrix} \begin{pmatrix} a_i \\ a_j \end{pmatrix} \tag{6.15}$$

where the sub-matrices are given by

$$S^p{}_{11} = S^p{}_{22} = \begin{pmatrix} \exp(-j\beta_1 L) & 0 & 0 \\ 0 & \ddots & 0 \\ 0 & 0 & \exp(-j\beta_{M_i} L) \end{pmatrix} \tag{6.16}$$

with the propagation length L of the optical connector and the propagation constant β_m for each mode.

The scattering matrix elements for each and every building blocks of the entire structure (device or circuit) need to be extracted efficiently and accurately. For an optical

connector, the scattering matrix elements can be obtained analytically by the mode propagation formula as shown in equation(6.16). It is fast and only costs very limited computational resources. In general, the scattering matrix elements for a functional optical element can be extracted numerically by the following procedures. Firstly, we launch the n-th mode from i-th port with unity power and calculate the transverse electromagnetic fields for the out-going waves at all port, i.e. $\mathbf{E}_n^{ij}$ and $\mathbf{H}_n^{ij}$ (j=1,…,p). The electromagnetic fields of a building block can be calculated by a numerical method such as FDTD, FDFD or BPM. We adopted the FDTD method for the simulations in this chapter. Once the transverse fields at the j-th port are obtained, the scattering matrix elements for the m-th mode at this port can be calculated by the following formula:

$$S_{nm}^{ij} = \frac{\iint \left(\mathbf{E}_n^{ij} \times \mathbf{h}_m^j + \mathbf{e}_m^j \times \mathbf{H}_n^{ij} \right) \hat{z} da}{2 \iint \left(\mathbf{e}_m^j \times \mathbf{h}_m^j \right) \hat{z} da} \tag{6.17}$$

By launching each mode at each port individually one by one and calculate the transverse fields at all ports, all the scattering matrix elements can be obtained.

6.5 Cascade of the Complex Scattering Matrices

Once the scattering matrix for every building blocks making up of a structure (device or circuit) is obtained, the total scattering matrix linking the ports of the entire structure can be calculated by cascading the scattering matrices of the corresponding adjacent building blocks. Figure 6.9 shows two adjacent building blocks with an interconnection port j and two other ports i and k.

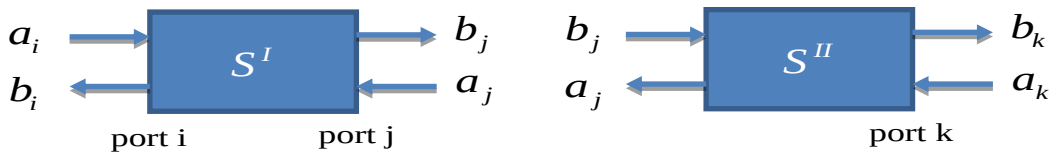

Figure 6.9 Two adjacent building blocks

The scattering matrix linking the i-th and j-th ports for the first building block is expressed as

$$\begin{pmatrix} b_j \\ b_i \end{pmatrix} = \begin{pmatrix} S^I{}_{11} & S^I{}_{12} \\ S^I{}_{21} & S^I{}_{22} \end{pmatrix} \begin{pmatrix} a_i \\ a_j \end{pmatrix} \tag{6.18}$$

And, the one linking the j-th and k-th ports for the second building block is given by

$$\begin{pmatrix} b_k \\ a_j \end{pmatrix} = \begin{pmatrix} S^{II}{}_{11} & S^{II}{}_{12} \\ S^{II}{}_{21} & S^{II}{}_{22} \end{pmatrix} \begin{pmatrix} b_j \\ a_k \end{pmatrix} \tag{6.19}$$

The total scattering matrix linking the i-th and k-th ports is calculated by cascading the above two matrices as

$$\begin{pmatrix} b_k \\ b_i \end{pmatrix} = \begin{pmatrix} S_{11} & S_{12} \\ S_{21} & S_{22} \end{pmatrix} \begin{pmatrix} a_i \\ a_k \end{pmatrix} \tag{6.20}$$

where the sub-matrices are given by

$$\begin{aligned} S_{11} &= S^{II}{}_{11}\left(I - S^I{}_{12}S^{II}{}_{21}\right)^{-1} S^I{}_{11} \\ S_{12} &= S^{II}{}_{11}\left(I - S^I{}_{12}S^{II}{}_{21}\right)^{-1} S^I{}_{12}S^{II}{}_{22} + S^{II}{}_{12} \\ S_{21} &= S^I{}_{22}\left(I - S^{II}{}_{21}S^I{}_{12}\right)^{-1} S^{II}{}_{21}S^I{}_{11} + S^I{}_{21} \\ S_{22} &= S^I{}_{22}\left(I - S^{II}{}_{21}S^I{}_{12}\right)^{-1} S^{II}{}_{22} \end{aligned} \tag{6.21}$$

6.6 Verification

To verify the proposed complex mode expansion circuit theory, several optical devices are partitioned with different schemes and analyzed by the proposed method. The results are compared with those obtained from the FDTD simulation of the corresponding entire structures.

As shown in Figure 6.10, the first optical device to analyze is band-pass filter consisting of two vertical ditches on a $2.0\mu m$ wide symmetric slab waveguide. The refractive indices of the core and cladding regions of the waveguide are $n_1 = 3.260$ and $n_0 = 3.218$, respectively. The refractive index of the two ditches is 1.0. The thickness of the two ditches is $b = 2.0\mu m$ and the distance of the closest edges of the two ditches is $a = 0.5\mu m$. The device is partitioned into 3 building blocks as shown in Figure 6.10. Block #1 and #3 are functional optical elements and block #2 is the optical connector. Block #1 and #3 are partitioned to be identical so that the scattering matrices of them can be extracted at the same time to save computational resources. All the interfaces of the three building blocks are located at outside of the two ditches, thus the corresponding ports have well guided index profiles. However, the distance of the two functional optical elements, i.e. block #1 and block #3, is not very large (a=0.5um). The radiation effects would affect the accuracy of the final result.

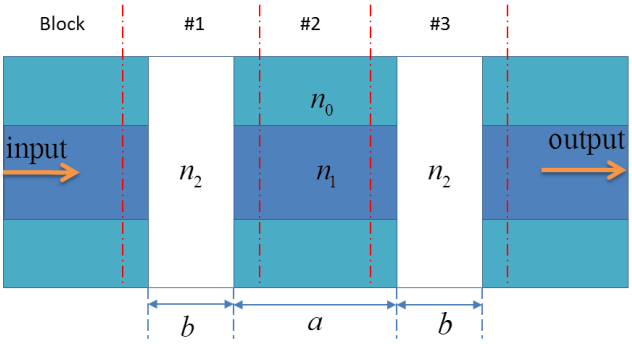

Figure 6.10 A band-pass filter consisting of two vertical ditches on a slab waveguide partitioned into 3 blocks: $n_0 = 3.218$, $n_1 = 3.260$, $n_2 = 1.0$, $a = 0.5\mu m$, $b = 2.0\mu m$

The scattering matrix of each building block is extracted by the method described in the previous section and the total scattering matrix for the entire device is calculated by cascading the scattering matrices of the three building blocks. The transmission and reflection coefficient of the first mode of the entire device is obtained from the total scattering matrix and shown in Figure 6.9 (a) and (b), respectively. The results obtained by the FDTD method are plotted using red dots as references. The results obtained by the circuit model with 1, 3 and 10 modes for the interconnection are depicted in Figure 6.11 using blue dotted line, purple dash line and black solid line, respectively. It shows that with the increasing number of modes for the interconnection, the results calculated by the circuit theory are more and more accurate compared with the references obtained from the FDTD method. In the modes used in the calculation, only the first mode is a guided mode. All the other modes are complex modes with radiations. This example provides clear evidence that when the radiation effects are taken into account by the complex mode expansion method, the accuracy of the result calculated by the circuit theory is

significantly improved compared with the conventional circuit theory which only employs the guided modes.

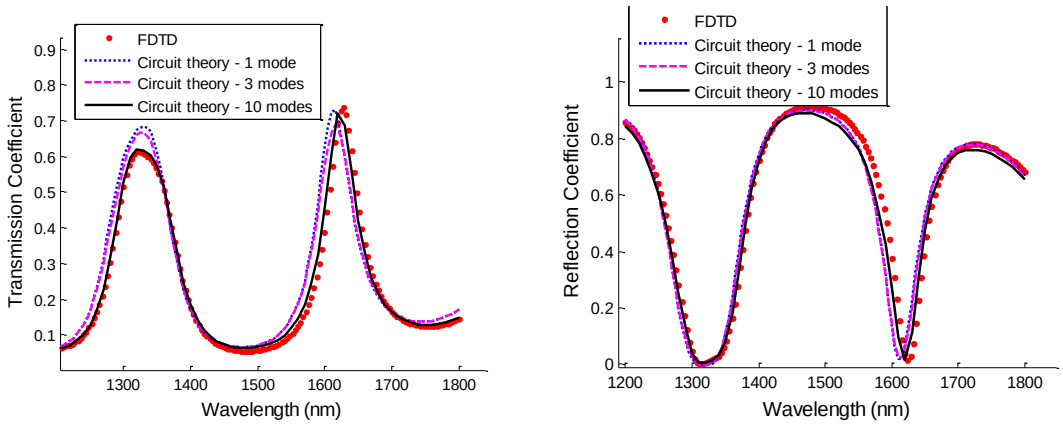

(a) (b)

Figure 6.11 Transmission (a) and reflection (b) coefficients of the first mode of the entire device: The red dots are the results calculated by the FDTD method, The blue dotted line, purple dash line and black solid line are the results calculated by the circuit theory with 1 mode, 3 modes and 10 modes, respectively, for the interconnection

To further demonstrate the usefulness of the radiation complex mode in the circuit theory, the same device is analyzed based on another partition scheme where the radiation effects are crucial to the accuracy of the final result. The device is partitioned into 5 building blocks as shown in Figure 12. Block #1, #2, #4 and #5 are functional optical elements. Block #3 is an optical connector. In this partition scheme, every functional optical element has an interface located in the ditches, which means the corresponding port has only radiation complex modes but no guide mode. The proposed circuit model based on complex mode expansion still works, while the conventional circuit model based on guided mode cannot be applied on this scheme at all.

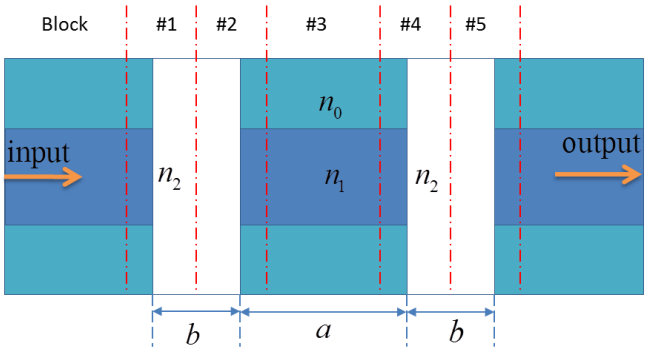

Figure 6.12 A band-pass filter consisting of two vertical ditches on a slab waveguide partitioned into 5 blocks: $n_0 = 3.218$, $n_1 = 3.260$, $n_2 = 1.0$, $a = 0.5\mu m$, $b = 2.0\mu m$

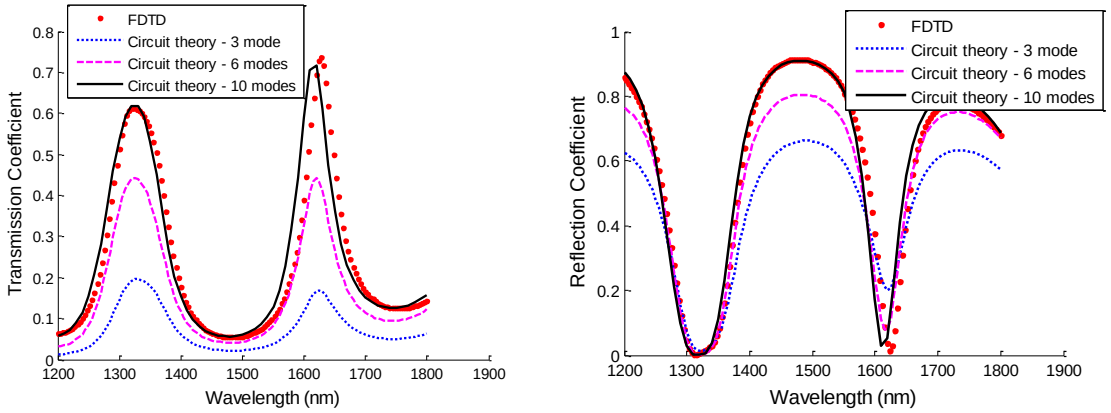

(a) (b)

Figure 6.13 Transmission (a) and reflection (b) coefficients of the first mode of the entire device: The red dots are the results calculated by the FDTD method, The blue dotted line, purple dash line and black solid line are the results calculated by the circuit theory with 3 mode, 6 modes and 10 modes, respectively, for the interconnection

The transmission and reflection coefficients of the first mode of the entire device are given in Figure 6.13 (a) and (b), respectively. The results calculated by the FDTD method are depicted by red dots as references. The results obtained by the circuit theory

with 3, 6 and 10 interconnection modes are plotted as blue dotted line, purple dash line and solid black line, respectively. It shows that with more and more complex modes for interconnections involved in the circuit model, the results converge quickly to the references.

To demonstrate the convergence more clearly, the relative error of the transmission coefficients versus the number of modes involved in the circuit model analysis is shown in Figure 6.14. The relative error of the circuit model obtained transmission coefficient to the reference data calculated by FDTD is defined by

$$e_{rel} = \frac{\sqrt{\sum_{i=1}^{N} \left| T^{ref}(\omega_i) - T(\omega_i) \right|^2}}{\sqrt{\sum_{i=1}^{N} \left| T^{ref}(\omega_i) \right|^2}} \qquad (6.22)$$

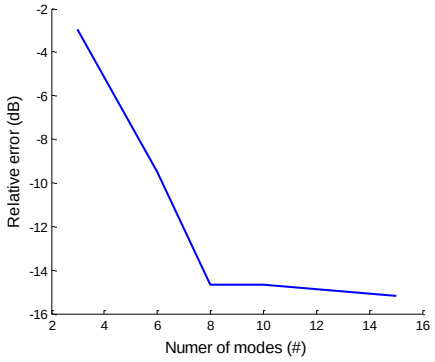

Figure 6.14 The relative error of the transmission coefficients versus the number of modes employed by the circuit model

6.7 Applications

Firstly, the proposed circuit theory based on the complex mode expansion is applied to analyze a one-dimensional coupled cavities photonic crystal filter proposed in Ref. [122]. The structure is shown in Figure 6.15. The filter is based on a silicon on

insulator (SOI) waveguide that consists of 360nm thick silicon on 1.5um thick silicon dioxide, air cladding and silicon substrate. The refractive indices of silicon and silicon dioxide are 3.48 and 1.46, respectively. The other structural parameters of the device are $N_{inner} = 9$, $N_{outer} = 4$, $h = 650nm$, $dH = 200nm$, $dL = 90nm$, and $D = 400nm$.

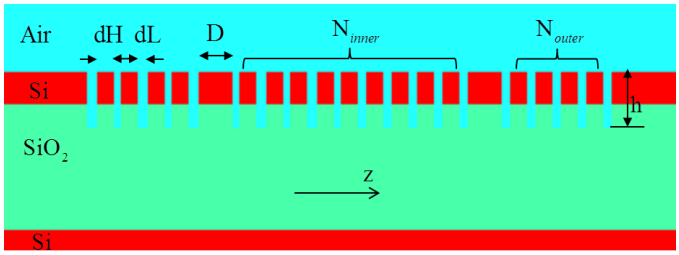

Figure 6.15 Structure of a one-dimensional couple cavities photonic crystal filter: $N_{inner} = 9$, $N_{outer} = 4$, $h = 650nm$, $dH = 200nm$, $dL = 90nm$, and $D = 400nm$

The entire device is partitioned into 22 building blocks as shown in Figure 6.16. The 6-th and 17-th blocks are optical connectors and all the other blocks are optical function elements. The scattering matrices for all building blocks are obtained by the parameter extraction method described before and are cascaded to generate the total scattering matrix for the entire device.

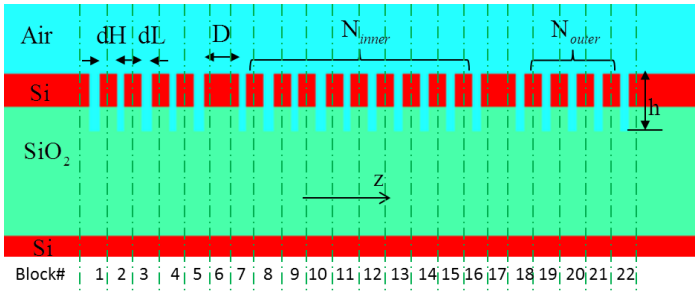

Figure 6.16 A one-dimensional couple cavities photonic crystal partitioned into 22 building blocks

The transmission and reflection coefficients of the narrow band-pass filter is obtained from the total scattering matrix and shown in Figure 6.17. It shows that with the increase of the number of modes for the interconnections in the circuit model analysis, the final results converge to the reference obtained by the FDTD method.

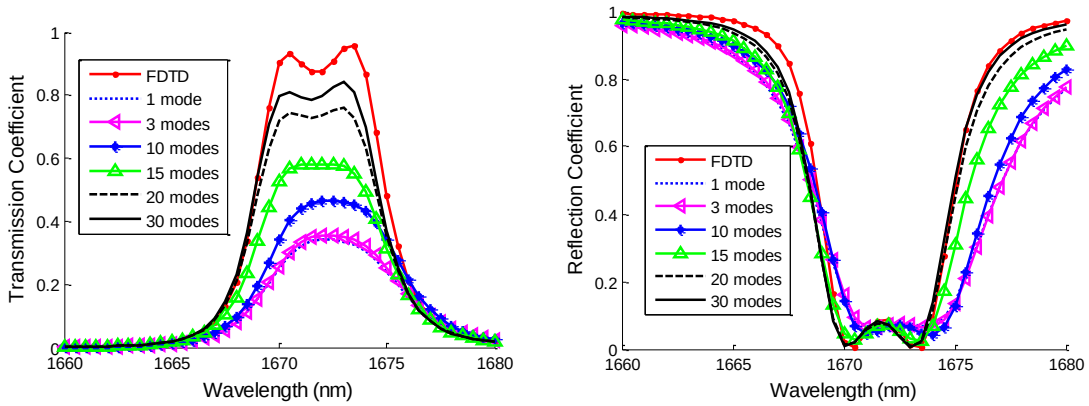

Figure 6.17 Transmission (a) and reflection (b) coefficients of the first mode of the 1D photonic crystal filter

The convergence of the relative error of the transmission coefficients versus the number of modes involved in the circuit model analysis is shown in Figure 6.18

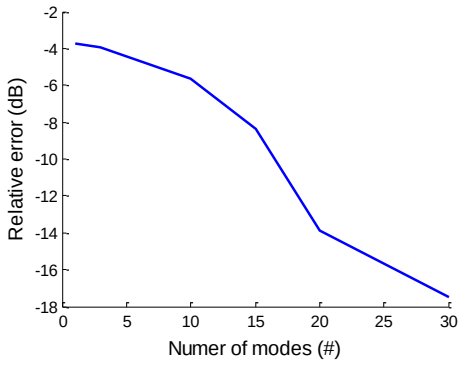

Figure 6.18 The relative error of the transmission coefficients versus the number of modes employed by the circuit model

Since the building blocks are very compact in the circuit analysis of this device, the radiation effects need to be taken into account carefully. Therefore, a large number of complex modes (at least 20) are required to obtain an accurate result (less than -10dB error).

As another application of the proposed circuit theory, an optical square disk resonator illustrated in Figure 6.19 is analyzed. The widths of the input and output bus waveguides are the same, i.e. $w = 0.2\mu m$. The refractive index of the core and cladding regions are 3.2 and 1.0, respectively. The square disk geometry parameters are $a = 1.6\mu m$ and $x = 0.4\mu m$. The separation of the disk and bus waveguide is $t = 0.1\mu m$. The entire structure is partitioned into four identical building blocks as shown in Figure 6.19. Only one building block need to be simulated by the FDTD method to extract the scattering matrix parameters for all the four building blocks. The overall scattering matrix is obtained from recombination of the scattering parameters of the four building blocks.

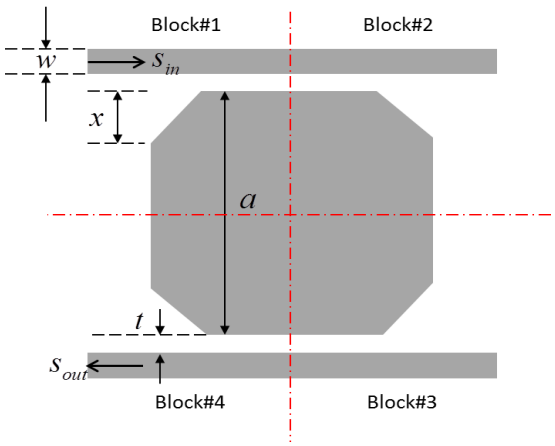

Figure 6.19 Schematic diagram for an optical square disk resonator.

The lightwave is shining through the top left port and monitored at the bottom left port of the device. The transmission spectrum of the fundamental mode at the input and output ports is calculated under different circumstances where different numbers of complex modes are considered for the interconnections of the four building blocks. One guided mode is considered for the four external ports. The transmission spectrums in the range from 1.50um to 1.60um are depicted in Figure 6.20. As a reference for the calculated data from the circuit theory analysis, the results obtained by simulating the entire resonator using the FDTD method are added in the same figure. As shown in Figure 6.20, by using more and more complex modes for interconnections, the circuit theory obtained results are closer and closer to those of the FDTD simulation. The peak of the fundamental mode transmission is located at 1.53um. The electric field amplitude distribution of the entire circuit when shining the 1.53um fundamental mode at the input port is obtained by the FDTD simulation and shown in Figure 6.21.

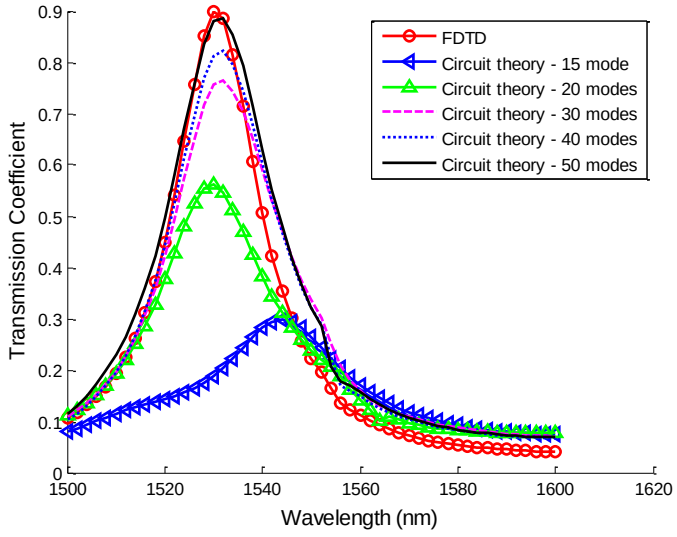

Figure 6.20 Transmission spectrum of the fundamental mode at the input and output ports of the structure shown in Figure 6.19: the red circles are data of a FDTD simulation; the blue and green triangles, purple dash line, blue dot-line and black solid line are calculated by the circuit theory using 15, 20, 30, 40 and 50 complex modes for interconnections, respectively.

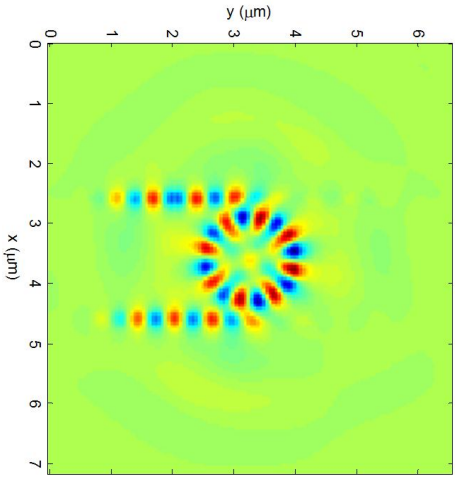

Figure 6.21 The electric field amplitude distribution of the entire structure when shining the 1.53um fundamental mode at the top left port.

6.8 Summary

In this chapter, the complex mode expansion method was introduced and a circuit theory based on the complex mode expansion was proposed. The new circuit theory was verified by a two-ditch band-pass filter. It showed that accuracy of the result is significantly improved due to the consideration of the radiation effects using the complex mode expansion of fields at the ports of interconnections. This theory even worked for the building blocks whose ports located at an open space where only complex radiation

modes exist. This theory was applied to analyze a one-dimensional photonic crystal narrow band-pass filter and a square disk resonator on SOI material systems. The proposed circuit theory is a powerful and versatile tool for analysis of large scale optical devices and circuits.

Chapter 7 Conclusions and Future Work

7.1 Summary of Contributions

In this thesis, the FDTD method and the circuit theory are intensively studied for design of large scale optical devices and circuits using computer-aided technologies. The efficiency of the FDTD method for simulation of a variety of materials is successfully improved by the new proposed models. First of all, a new method combining the hardware accelerated FDTD method and the matrix pencil method is proposed to do waveguide modal analysis efficiently. In addition, a circuit theory based on complex mode expansion method is proposed and implemented to analyze compact optical devices and high density integrated circuits with non-negligible radiation effects. The main work and contributions of this thesis are summarized as follows.

Firstly, a novel rational dispersion model, referred to as the Rational Dispersion Model (RDM) is proposed for modeling arbitrary linear dispersive materials. This model is proved to be more efficient in fitting the material permittivity functions compared with the conventional Debye, Drude and Lorentz models. A generally applicable method is introduced to estimate the parameters of this model with no initial guess requirement, which makes it feasible in practical applications. The new model is implemented in the FDTD method to improve the efficiency of simulating optical devices in a wide wavelength range. The improved FDTD method is employed to systematically study the cross-section spectra characteristics of different nano-particles surrounded by different materials, which produced a good reference for design of optical devices consisting of

metal nano-particles, such as optical sensors, optical filters, etc. For the nonlinear materials, the RDM is integrated into the nonlinear FDTD method to simulate optical devices with the second and third order nonlinear effects. In the simulation of semiconductor lasers with arbitrary cavity geometries, the FDTD method and the rate equation model are combined and employed. The efficiency of this method is significantly improved by utilizing the RDM to model the gain materials and to use the Newton iteration method to discretize the carrier rate equation.

Secondly, a two-dimensional (2D) compact FDTD mode solver for both guided and leaky waveguide analysis is developed. It is based on the wave equation formalism in combination with the Matrix Pencil Method (MPM). By taking advantage of the inherent parallel nature of the FDTD algorithm, the mode solver is implemented on graphics processing units (GPUs) using the compute unified device architecture (CUDA). While the memory requirement keeps the same, the speed of this mode solver could be dramatically increased by the high-performance computing technique. The advantages of this new approach become even more pronounced when the scale of the waveguide cross-section is large, because the standard FDTD method is prohibitively time-consuming and the conventional FD solver is severely limited by its memory consumption.

Finally, a circuit theory is proposed in analysis of compact optical devices and large scale high density integrated optical circuits. The new circuit theory employs the complex mode theory to expand the electromagnetic fields in the waveguides that interconnect different parts of the target structure. The radiation effects in the interconnections are carefully taken into account. It proves that this method is very

efficient and accurate in analysis of modern optical structures in which the radiation effects in the interconnections play an important role in the performance of the entire component.

7.2 Suggestions of Future Work

The following topics are suggested as the extension of the work done in this thesis.

1) Implementations of the RDM in other numerical methods to simulate the electromagnetic fields, such as the Transmission Line Method (TLM), the Discontinuous Galerkin Time-Domain (DGTD) method, the Pseudo-Spectral Time-Domain (PSTD) method, etc.
2) Modeling the gain profile and the refractive index derivation of gain materials simultaneously in simulation of optical sources, such as the semiconductor laser, light emitting diode, etc.
3) Implementation of the circuit model under parallel computing environments such as the many-core computers, the computer clusters, etc.

Bibliography

1. Xu, C. *CAD for Photonic Devices and Circuit*. in *Optical Fiber Communication & Optoelectronic Exposition & Conference*. 2006. Shanghai, China IEEE.
2. Gallagher, D. and P. Design, *Photonic cad matures.* IEEE LEOS NewsLetter, 2008.
3. Van Roey, J., J. Van der Donk, and P. Lagasse, *Beam-propagation method: analysis and assessment.* JOSA, 1981. **71**(7): p. 803-810.
4. Huang, W., et al., *The finite-difference vector beam propagation method: analysis and assessment.* Lightwave Technology, Journal of, 1992. **10**(3): p. 295-305.
5. Huang, W. and C. Xu, *Simulation of three-dimensional optical waveguides by a full-vector beam propagation method.* Quantum Electronics, IEEE Journal of, 1993. **29**(10): p. 2639-2649.
6. Jiang, K. and W.P. Huang, *Finite-difference-based mode-matching method for 3-D waveguide structures under semivectorial approximation.* Journal of Lightwave Technology, 2005. **23**(12): p. 4239.
7. Mu, J. and W.P. Huang, *Simulation of three-dimensional waveguide discontinuities by a full-vector mode-matching method based on finite-difference schemes.* Optics Express, 2008. **16**(22): p. 18152-18163.
8. Huang, W.P., *Coupled-mode theory for optical waveguides: an overview.* JOSA A, 1994. **11**(3): p. 963-983.
9. Huang, W.P. and J. Mu, *Complex coupled-mode theory for optical waveguides.* Optics Express, 2009. **17**(21): p. 19134-19152.
10. Haus, H.A. and W. Huang, *Coupled-mode theory.* Proceedings of the IEEE, 1991. **79**(10): p. 1505-1518.
11. Taflove, A. and S. Hagness, *Computational Electrodynamics: The Finite-Difference Time-Domain Method 3rd edn (Norwood, MA: Artech House)*. 2005, Wiley.
12. Luebbers, R.J. and F. Hunsberger, *FDTD for Nth-order dispersive media.* Antennas and Propagation, IEEE Transactions on, 1992. **40**(11): p. 1297-1301.
13. Sullivan, D.M., *Frequency-dependent FDTD methods using Z transforms.* Antennas and Propagation, IEEE Transactions on, 1992. **40**(10): p. 1223-1230.
14. Xu, F., et al., *Finite-difference frequency-domain algorithm for modeling guided-wave properties of substrate integrated waveguide.* Microwave Theory and Techniques, IEEE Transactions on, 2003. **51**(11): p. 2221-2227.
15. Rumpf, R., *SIMPLE IMPLEMENTATION OF ARBITRARILY SHAPED TOTAL-FIELD/SCATTERED-FIELD REGIONS IN FINITE-DIFFERENCE FREQUENCY-DOMAIN.*
16. Margengo, E., C.M. Rappaport, and E.L. Miller, *Optimum PML ABC conductivity profile in FDFD.* Magnetics, IEEE Transactions on, 1999. **35**(3): p. 1506-1509.
17. *FDTD solutions from Lumerical Solutions Inc*.
18. *Photonic Component Design Suite, BeamPROP, FullWave from Rsoft Inc.*

19. Hao, F. and P. Nordlander, *Efficient dielectric function for FDTD simulation of the optical properties of silver and gold nanoparticles.* Chemical Physics Letters, 2007. **446**(1-3): p. 115-118.
20. Joseph, R.M. and A. Taflove, *FDTD Maxwell's equations models for nonlinear electrodynamics and optics.* Antennas and Propagation, IEEE Transactions on, 1997. **45**(3): p. 364-374.
21. Guiffaut, C. and K. Mahdjoubi, *A parallel FDTD algorithm using the MPI library.* Antennas and Propagation Magazine, IEEE, 2001. **43**(2): p. 94-103.
22. Varadarajan, V. and R. Mittra, *Finite-difference time-domain (FDTD) analysis using distributed computing.* Microwave and Guided Wave Letters, IEEE, 1994. **4**(5): p. 144-145.
23. Gupta, K.C., R. Garg, and R. Chadha, *Computer aided design of microwave circuits.* NASA STI/Recon Technical Report A, 1981. **82**: p. 39449.
24. Gupta, K.C. and A. Singh, *Microwave integrated circuits.* New York, Halsted Press, 1974. 389 p, 1974. **1**.
25. Yamamoto, S. and T. Makimoto, *Circuit theory for a class of anisotropic and gyrotropic thin‐film optical waveguides and design of nonreciprocal devices for integrated optics.* Journal of Applied Physics, 1974. **45**(2): p. 882-888.
26. Nishihara, H., M. Haruna, and T. Suhara, *Optical integrated circuits*. 1989: McGraw-Hill Professional.
27. Snyder, A.W. and J.D. Love, *Optical waveguide theory*. Vol. 190. 1983: Springer.
28. Manolatou, C., et al., *High-density integrated optics.* Journal of Lightwave Technology, 1999. **17**(9): p. 1682.
29. Espinola, R., et al., *Fast and low-power thermooptic switch on thin silicon-on-insulator.* Photonics Technology Letters, IEEE, 2003. **15**(10): p. 1366-1368.
30. Liu, A., et al., *A high-speed silicon optical modulator based on a metal–oxide–semiconductor capacitor.* Nature, 2004. **427**(6975): p. 615-618.
31. Ahmad, R., et al., *Ultracompact corner-mirrors and T-branches in silicon-on-insulator.* Photonics Technology Letters, IEEE, 2002. **14**(1): p. 65-67.
32. Chang, S.H., S. Gray, and G. Schatz, *Surface plasmon generation and light transmission by isolated nanoholes and arrays of nanoholes in thin metal films.* Optics Express, 2005. **13**(8): p. 3150-3165.
33. Lee, T.W. and S. Gray, *Subwavelength light bending by metal slit structures.* Optics Express, 2005. **13**(24): p. 9652-9659.
34. Vial, A., et al., *Improved analytical fit of gold dispersion: Application to the modeling of extinction spectra with a finite-difference time-domain method.* Physical Review B, 2005. **71**(8): p. 085416.
35. Kelley, D.F. and R.J. Luebbers, *Piecewise linear recursive convolution for dispersive media using FDTD.* Antennas and Propagation, IEEE Transactions on, 1996. **44**(6): p. 792-797.
36. Laroche, T. and C. Girard, *Near-field optical properties of single plasmonic nanowires.* Applied physics letters, 2006. **89**: p. 233119.

37. McMahon, J.M., et al., *Tailoring the sensing capabilities of nanohole arrays in gold films with Rayleigh anomaly-surface plasmon polaritons.* Optics Express, 2007. **15**(26): p. 18119-18129.
38. Rakic, A.D., et al., *Optical properties of metallic films for vertical-cavity optoelectronic devices.* Applied Optics, 1998. **37**(22): p. 5271-5283.
39. Vial, A. and T. Laroche, *Comparison of gold and silver dispersion laws suitable for FDTD simulations.* Applied Physics B: Lasers and Optics, 2008. **93**(1): p. 139-143.
40. Han, M., R.W. Dutton, and S. Fan, *Model dispersive media in finite-difference time-domain method with complex-conjugate pole-residue pairs.* Microwave and Wireless Components Letters, IEEE, 2006. **16**(3): p. 119-121.
41. Udagedara, I., et al., *Unified perfectly matched layer for finite-difference time-domain modeling of dispersive optical materials.* Optics Express, 2009. **17**(23): p. 21179-21190.
42. Etchegoin, P., E. Le Ru, and M. Meyer, *An analytic model for the optical properties of gold.* The Journal of chemical physics, 2006. **125**: p. 164705.
43. Vial, A., *Implementation of the critical points model in the recursive convolution method for modelling dispersive media with the finite-difference time domain method.* Journal of Optics A: Pure and Applied Optics, 2007. **9**: p. 745.
44. Hamidi, M., et al., *Implementation of the critical points model in a SFM-FDTD code working in oblique incidence.* Journal of Physics D: Applied Physics, 2011. **44**: p. 245101.
45. Gustavsen, B. and A. Semlyen, *Rational approximation of frequency domain responses by vector fitting.* Power Delivery, IEEE Transactions on, 1999. **14**(3): p. 1052-1061.
46. Zeng, R.X. and J.H. Sinsky. *Modified rational function modeling technique for high speed circuits*. 2006: IEEE MTT-S Int. Microwave Symp. Dig.
47. Kirkpatrick, S., C.D. Gelatt, and M.P. Vecchi, *Optimization by simulated annealing.* science, 1983. **220**(4598): p. 671.
48. Johnson, P.B. and R. Christy, *Optical constants of the noble metals.* Physical Review B, 1972. **6**(12): p. 4370.
49. Roden, J.A. and S.D. Gedney, *Convolutional PML (CPML): An efficient FDTD implementation of the CFS-PML for arbitrary media.* Microwave and optical technology letters, 2000. **27**(5): p. 334-338.
50. Rother, T., K. Schmidt, and R.S.G.S. Neustrelitz, *The discretized Mie-formalism for electromagnetic scattering.* Progress In Electromagnetics Research, 1997. **17**: p. 91-183.
51. Fu, Y., K. Li, and F. Kong, *Analysis of the optical transmission through the metal plate with slit array.* Progress In Electromagnetics Research, 2008. **82**: p. 109-125.
52. Qi, L.M. and Z. Yang, *Modified plane wave method analysis of dielectric plasma photonic crystal.* Progress In Electromagnetics Research, 2009. **91**: p. 319-332.

53. Handapangoda, C., M. Premaratne, and P. Pathirana, *Plane wave scattering by a spherical di-electric particle in motion: a relativistic extension of the mie theory.* Progress In Electromagnetics Research, 2011. **112**: p. 349-379.
54. Duan, X., J. Wang, and C.M. Lieber, *Synthesis and optical properties of gallium arsenide nanowires.* Applied physics letters, 2000. **76**: p. 1116.
55. Bro nstrup, G., et al., *Optical Properties of Individual Silicon Nanowires for Photonic Devices.* ACS nano.
56. Yamamoto, N., S. Ohtani, and F.J. Garci a de Abajo, *Gap and Mie Plasmons in Individual Silver Nanospheres near a Silver Surface.* Nano letters, 2011.
57. McMahon, J.M., S.K. Gray, and G.C. Schatz, *Optical properties of nanowire dimers with a spatially nonlocal dielectric function.* Nano letters, 2010.
58. Smajic, J., et al., *Comparison of numerical methods for the analysis of plasmonic structures.* Journal of Computational and Theoretical Nanoscience, 2009. **6**(3): p. 763-774.
59. Talley, C.E., et al., *Surface-enhanced Raman scattering from individual Au nanoparticles and nanoparticle dimer substrates.* Nano letters, 2005. **5**(8): p. 1569-1574.
60. Bohren, C.F. and D.R. Huffman, *Absorption and scattering of light by small particles.* Research supported by the University of Arizona and Institute of Occupational and Environmental Health. New York, Wiley-Interscience, 1983, 541 p., 1983. **1**.
61. Hu, X.J. and D.B. Ge, *Study on conformal FDTD for electromagnetic scattering by targets with thin coating.* Progress In Electromagnetics Research, 2008. **79**: p. 305-319.
62. Swillam, M.A., et al., *Efficient approach for sensitivity analysis of lossy and leaky structures using FDTD.* Progress In Electromagnetics Research, 2009. **94**: p. 197-212.
63. Zhang, Y.Q. and D.B. Ge, *A unified FDTD approach for electromagnetic analysis of dispersive objects.* Progress In Electromagnetics Research, 2009. **96**: p. 155-172.
64. Huang, C.H., et al., *Image reconstruction of the buried metallic cylinder using FDTD method and SSGA.* Progress In Electromagnetics Research, 2008. **85**: p. 195-210.
65. Lee, K., et al., *Implementation of the fdtd method based on lorentz-drude dispersive model on gpu for plasmonics applications.* Progress In Electromagnetics Research, 2011. **116**: p. 441-456.
66. Futamata, M., Y. Maruyama, and M. Ishikawa, *Local electric field and scattering cross section of Ag nanoparticles under surface plasmon resonance by finite difference time domain method.* The Journal of Physical Chemistry B, 2003. **107**(31): p. 7607-7617.
67. Gedney, S.D., *An anisotropic perfectly matched layer-absorbing medium for the truncation of FDTD lattices.* Antennas and Propagation, IEEE Transactions on, 1996. **44**(12): p. 1630-1639.

68. Li, J., L.X. Guo, and H. Zeng, *FDTD investigation on bistatic scattering from a target above two-layered rough surfaces using UPML absorbing condition.* Progress In Electromagnetics Research, 2008. **88**: p. 197-211.
69. Ryoo, S., et al. *Optimization principles and application performance evaluation of a multithreaded GPU using CUDA*. 2008: ACM.
70. Tanaka, K., *Optical nonlinearity in photonic glasses.* Journal of Materials Science: Materials in Electronics, 2005. **16**(10): p. 633-643.
71. Osgood Jr, R., et al., *Engineering nonlinearities in nanoscale optical systems: physics and applications in dispersion-engineered silicon nanophotonic wires.* Advances in Optics and Photonics, 2009. **1**(1): p. 162-235.
72. Lin, Q., O.J. Painter, and G.P. Agrawal, *Nonlinear optical phenomena in silicon waveguides: modeling and applications.* Optics Express, 2007. **15**(25): p. 16604-16644.
73. Foster, M.A., et al., *Nonlinear optics in photonic nanowires.* Optics Express, 2008. **16**(2): p. 1300-1320.
74. Koos, C., et al., *Nonlinear silicon-on-insulator waveguides for all-optical signal processing.* Optics Express, 2007. **15**(10): p. 5976-5990.
75. Rukhlenko, I.D., M. Premaratne, and G.P. Agrawal, *Nonlinear silicon photonics: Analytical tools.* Selected Topics in Quantum Electronics, IEEE Journal of, 2010. **16**(1): p. 200-215.
76. Dissanayake, C.M., et al., *FDTD modeling of anisotropic nonlinear optical phenomena in silicon waveguides.* Optics Express, 2010. **18**(20): p. 21427-21448.
77. Fujii, M., et al., *High-order FDTD and auxiliary differential equation formulation of optical pulse propagation in 2-D Kerr and Raman nonlinear dispersive media.* Quantum Electronics, IEEE Journal of, 2004. **40**(2): p. 175-182.
78. Naqavi, A., et al., *Extension of Unified Formulation for the FDTD Simulation of Nonlinear Dispersive Media.* Photonics Technology Letters, IEEE, 2010. **22**(16): p. 1214-1216.
79. Li, D. and C.D. Sarris, *Time-Domain Modeling of Nonlinear Optical Structures With Extended Stability FDTD Schemes.* Journal of Lightwave Technology, 2011. **29**(7): p. 1003-1010.
80. Blow, K.J. and D. Wood, *Theoretical description of transient stimulated Raman scattering in optical fibers.* Quantum Electronics, IEEE Journal of, 1989. **25**(12): p. 2665-2673.
81. Hile, C.V. and W.L. Kath, *Numerical solutions of Maxwell's equations for nonlinear-optical pulse propagation.* JOSA B, 1996. **13**(6): p. 1135-1146.
82. Ziolkowski, R.W. and J.B. Judkins, *Nonlinear finite-difference time-domain modeling of linear and nonlinear corrugated waveguides.* JOSA B, 1994. **11**(9): p. 1565-1575.
83. Goorjian, P.M. and A. Taflove, *Direct time integration of Maxwell's equations in nonlinear dispersive media for propagation and scattering of femtosecond electromagnetic solitons.* Optics letters, 1992. **17**(3): p. 180-182.
84. Li, X., et al., *A physics-based three-dimensional model for distributed feedback laser diodes.* Quantum Electronics, IEEE Journal of, 1998. **34**(9): p. 1545-1553.

85. Champagne, A., et al., *Global and local effects in gain-coupled multiple-quantum-well DFB lasers.* Quantum Electronics, IEEE Journal of, 1999. **35**(10): p. 1390-1401.
86. Yamanaka, T., S. Seki, and K. Yokoyama, *Numerical analysis of static wavelength shift for DFB lasers with longitudinal mode spatial hole burning.* Photonics Technology Letters, IEEE, 1991. **3**(7): p. 610-612.
87. Marcuse, D., *Computer model of an injection laser amplifier.* Quantum Electronics, IEEE Journal of, 1983. **19**(1): p. 63-73.
88. Marcuse, D., *Computer simulation of laser photon fluctuations: Theory of single-cavity laser.* Quantum Electronics, IEEE Journal of, 1984. **20**(10): p. 1139-1148.
89. Henry, C., *Theory of the phase noise and power spectrum of a single mode injection laser.* Quantum Electronics, IEEE Journal of, 1983. **19**(9): p. 1391-1397.
90. Li, W., W.P. Huang, and X. Li, *Digital filter approach for simulation of a complex integrated laser diode based on the traveling-wave model.* Quantum Electronics, IEEE Journal of, 2004. **40**(5): p. 473-480.
91. Li, X. and W.P. Huang, *Simulation of DFB semiconductor lasers incorporating thermal effects.* Quantum Electronics, IEEE Journal of, 1995. **31**(10): p. 1848-1855.
92. Xi, Y., X. Li, and W.P. Huang, *Time-domain standing-wave approach based on cold cavity modes for simulation of DFB lasers.* Quantum Electronics, IEEE Journal of, 2008. **44**(10): p. 931-937.
93. Hagness, S.C., R.M. Joseph, and A. Taflove, *Subpicosecond electrodynamics of distributed Bragg reflector microlasers: Results from finite difference time domain simulations.* Radio Sci, 1996. **31**(4): p. 931-941.
94. Nagra, A.S. and R.A. York, *FDTD analysis of wave propagation in nonlinear absorbing and gain media.* Antennas and Propagation, IEEE Transactions on, 1998. **46**(3): p. 334-340.
95. Pernice, W.H.P., F.P. Payne, and D.F.G. Gallagher, *A finite-difference time-domain method for the simulation of gain materials with carrier diffusion in photonic crystals.* Journal of Lightwave Technology, 2007. **25**(9): p. 2306-2314.
96. Schweig, E. and W. Bridges, *Computer analysis of dielectric waveguides: A finite-difference method.* IEEE Transactions on Microwave Theory and Techniques, 1984. **32**(5): p. 531-541.
97. Stern, M., *Semivectorial polarised finite difference method for opticalwaveguides with arbitrary index profiles.* IEE Proceedings J Optoelectronics [see also IEE Proceedings-Optoelectronics], 1988. **135**(1): p. 56-63.
98. Huang, W.P., et al., *A scalar finite-difference time-domain approach to guided-wave optics*. 1991. p. 524-526.
99. Fallahkhair, A., K. Li, and T. Murphy, *Vector finite difference modesolver for anisotropic dielectric waveguides.* Journal of Lightwave Technology, 2008. **26**(11): p. 1423-1431.
100. Xu, C., et al., *Full-vectorial mode calculations by finite difference method.* IEE Proceedings-Optoelectronics, 1994. **141**(5): p. 281-286.

101. Rahman, B. and J. Davies, *Finite-element analysis of optical and microwave waveguide problems.* IEEE Transactions on Microwave Theory and Techniques, 1984. **32**(1): p. 20-28.
102. Lee, J., D. Sun, and Z. Cendes, *Full-wave analysis of dielectric waveguides using tangential vector finite elements.* IEEE Transactions on Microwave Theory and Techniques, 1991. **39**(8): p. 1262-1271.
103. Feit, M. and J. Fleck, JA, *Computation of mode properties in optical fiber waveguides by a propagating beam method.* Applied Optics, 1980. **19**(7): p. 1154-1164.
104. Xu, C., W. Huang, and S. Chaudhuri, *Efficient and accurate vector mode calculations by beam propagationmethod.* Lightwave Technology, Journal of, 1993. **11**(7): p. 1209-1215.
105. Tsuji, Y. and M. Koshiba, *Guided-mode and leaky-mode analysis by imaginary distance beam propagation method based on finite element scheme.* Journal of Lightwave Technology, 2000. **18**(4): p. 618.
106. Zhao, A., J. Juntunen, and A. Räisänen, *Analysis of hybrid modes in channel multilayer optical waveguides with the compact 2-D FDTD method.* Microwave and Optical Technology Letters, 1997. **15**(6): p. 398-403.
107. Xiao, S., R. Vahldieck, and H. Jin, *Full-wave analysis of guided wave structures using a novel 2-D FDTD.* IEEE Microwave and Guided Wave Letters, 1992. **2**(5): p. 165-167.
108. Zhou, G. and X. Li, *Wave equation-based semivectorial compact 2-D-FDTD method for optical waveguide modal analysis.* Journal of Lightwave Technology, 2004. **22**(2): p. 677.
109. Sarkar, T. and O. Pereira, *Using the matrix pencil method to estimate the parameters of a sum of complex exponentials.* IEEE Antennas and Propagation Magazine, 1995. **37**(1): p. 48-55.
110. Sacks, Z., et al., *A perfectly matched anisotropic absorber for use as an absorbingboundary condition.* IEEE Transactions on Antennas and Propagation, 1995. **43**(12): p. 1460-1463.
111. Gedney, S., *An anisotropic perfectly matched layer-absorbing medium for thetruncation of FDTD lattices.* IEEE Transactions on Antennas and Propagation, 1996. **44**(12): p. 1630-1639.
112. Taflove, A. and S. Hagness, *Computational electrodynamics: the finite-difference time-domain method*. 1995: Artech House Norwood, MA.
113. Ryoo, S., et al. *Optimization principles and application performance evaluation of a multithreaded GPU using CUDA*. 2008: ACM.
114. Krakiwsky, S., L. Turner, and M. Okoniewski. *Acceleration of finite-difference time-domain (FDTD) using graphics processor units (GPU)*. in *Microwave Symposium Digest, IEEE MTT-S International*. 2004.
115. Balevic, A., et al. *Accelerating simulations of light scattering based on finite-difference time-domain method with general purpose gpus*. 2008.
116. Okoniewski, M., *Vector wave equation 2-D-FDTD method for guided wave problems.* IEEE Microwave and Guided Wave Letters, 1993. **3**(9): p. 307-309.

117. Berenger, J., *A perfectly matched layer for the absorption of electromagnetic waves.* Journal of computational physics, 1994. **114**(2): p. 185-200.
118. Huang, W. and C. Xu, *Simulation of three-dimensional optical waveguides by a full-vectorbeam propagation method.* IEEE Journal of Quantum Electronics, 1993. **29**(10): p. 2639-2649.
119. Chew, W. and W. Weedon, *A 3-D perfectly matched medium from modified Maxwell's equations with stretched coordinates.* Microwave and Optical Technology Letters, 1994. **7**(13): p. 599-604.
120. Goell, J., *A circular-harmonic computer analysis of rectangular dielectric waveguides.* Bell System Technical Journal, 1969. **48**: p. 2133-2160.
121. Heaton, J., et al., *Optimization of deep-etched, single-mode GaAs/AlGaAs optical waveguides using controlled leakage into the substrate.* Journal of Lightwave Technology, 1999. **17**(2): p. 267.
122. Chen, Q. and D.W.E. Allsopp, *One-dimensional coupled cavities photonic crystal filters with tapered Bragg mirrors.* Optics Communications, 2008. **281**(23): p. 5771-5774.

Appendix A List of publications related to the thesis work

Journal papers:

L. Han, Y. Xi, W.-P. Huang, "Acceleration of FDTD mode solver by high-performance computing techniques", 2010, Optics Express 18(13): 13679-13692.

R. Wang, L. Han, J. Mu, W.-P. Huang, "Simulation of waveguide crossings and corners with complex mode matching method", 2012, Journal of Lightwave Technology, accepted.

L. Han, D. Zhou, K. Li, X. Li, W.-P. Huang, "A rational dispersion model for efficient simulation of dispersive media in the FDTD method", submitted for publication.

Q. Guo, X. Li, J. Mu, L. Han, W.-P. Huang, "Planar Waveguide Polarization Beam Splitter Based on the Form Birefringence", submitted for publication

W.-P. Huang, L. Han, J. Mu, "Modeling and simulation of large-scale planar lightwave circuits including radiation", in preparation.

L. Deng, L. Han, Y. Xi, X. Li, W.-P. Huang, "Design optimization of high performance quantum dot Fabry-Perot lasers", in preparation.

Conference papers:

L. Han, Y. Wen, W.-P. Huang, "Automatic Extraction of Chirp Parameter of DFB Laser", Integrated Photonics Research, Silicon and Nano Photonics, 2011, Toronto

R. Wang, L. Han, J. Mu, W.-P. Huang, "Simulation of Waveguide Corner and Cross by Complex Mode Matching Method", Integrated Photonics Research, Silicon and Nano Photonics, 2011, Toronto

L. Deng, L. Han, Y. Xi, X. Li, W.-P. Huang, “Design Optimization of High Performance Single-mode Fabry-Perot Lasers Based on Quantum Dot Materials”, Integrated Photonics Research, Silicon and Nano Photonics, 2011, Toronto